

Dissertation submitted to
the Combined Faculties of the Natural Sciences and Mathematics
of the Ruperto-Carola-University of Heidelberg, Germany
for the degree of Doctor of Natural Sciences

Put forward by

M.Sc. Milica Mičić
born in Kruševac, Republic of Serbia

Oral examination: **January 9th, 2013**

Molecular cloud formation
with self-consistent thermal and chemical
treatment of the gas

Referees:

Prof. Dr. Ralf Klessen

Institut für Theoretische Astrophysik, Universität Heidelberg

Priv. Doz. Dr. Henrik Beuther

Max-Planck-Institut für Astronomie, Heidelberg

Zusammenfassung

Physikalische und chemische Prozesse, welche die Entstehung und Entwicklung von Riesenmolekülwolken (giant molecular clouds, GMCs) bestimmen, sind für das Verständnis der Sternentstehung von großer Wichtigkeit. GMCs bestehen hauptsächlich aus molekularem Wasserstoff, es gibt aber mehr als 200 chemische Verbindungen diverser Kombinationen von Kohlenstoff-, Stickstoff- und Sauerstoffatomen. Diese Verbindungen bestimmen das Kühlverhalten sowie die thermische und dynamische Entwicklung der Gaswolke. Um die Beschränkungen der meisten bisherigen Modelle bedingt durch die Komplexität chemischer Reaktionsnetzwerke und deren Einbindung in numerische Simulationen zu umgehen, haben wir eine detaillierte Behandlung atomarer/molekularer Kühlung und Wasserstoffchemie in moderne hochauflösende hydrodynamische Simulationen integriert. Das Hauptaugenmerk unserer Untersuchungen liegt auf den Auswirkungen, welche die Wahl unterschiedlicher Kühlfunktionen und Turbulenztreiber auf die Entstehung und Entwicklung molekularen Gases hat. Auf diese Weise untersuchen wir den Einfluss der Art von Turbulenz auf die Bildung molekularen Wasserstoffes, indem wir sowohl quellenfreie (also divergenzfremde) und kompressible (also rotationsfreie) Turbulenztreiber betrachten. Die Ergebnisse verwenden wir zur Überprüfung einer einfachen Vorschrift zur Modellierung des Einflusses unaufgelöster Dichteschwankungen auf die H_2 Erzeugungsrate in großskaligen Simulation der ISM, welche von Gnedin et al. (2009) vorgeschlagen wurde. Ferner untersuchen wir die Eigenschaften dichter Haufen, welche sich in unserem Modell der Entstehung molekularer Wolken in konvergierenden Strömungen bilden. Dabei vergleichen wir die Ergebnisse einer einfachen, parametrisierten Kühlfunktion, die von Koyama & Inutsuka (2002) eingeführt wurde und in vielen Arbeiten zu konvergierenden Strömungen Verwendung findet, mit den Ergebnissen der detaillierten Berechnung von Nichtgleichgewichtschemie und thermischem Gleichgewicht des Gases. Zuletzt betrachten wir die C I und CO Emission molekularer Wolken im Vergleich zu deren Säulendichte und der Gesamtsäulendichte, um die Struktur der Wolke zu verfolgen.

Abstract

Understanding physical and chemical processes that guide the formation and evolution of giant molecular clouds (GMCs) has important implications for the formation of stars. GMCs dominantly consist of molecular hydrogen, but there are more than 200 chemical species of various combinations of carbon, nitrogen and oxygen atoms. Together, these species control the cooling ability with the thermal and dynamical evolution of the gas cloud. In order to overcome the restrictions encountered by most previous models of molecular cloud formation due to the complexity of chemical reaction networks and its inclusion in hydrodynamical codes, we have implemented detailed treatment of atomic/molecular cooling and hydrogen chemistry into state-of-art high resolution hydrodynamical simulations. The main focus of our study is on the influence that choosing between different cooling functions and turbulent driving has on the formation and evolution of molecular gas. In that manner, we study the influence of the nature of the turbulence on the formation of molecular hydrogen by examining both solenoidal (divergence-free) and compressive (curl-free) turbulent driving. The obtained results we use to test a simple prescription suggested by Gnedin et al. (2009) for modelling the influence of unresolved density fluctuations on the H_2 formation rate in large-scale simulations of the ISM. We also investigate the properties of the dense clumps formed within our model of the molecular cloud formation in converging flows and directly compare the results obtained using the simple, parametrized cooling function introduced by Koyama & Inutsuka (2002) and used by a number of converging flows studies with the results of the detailed calculation of the non-equilibrium chemistry and thermal balance of the gas. Finally, we study C I and CO emission from molecular clouds in comparison to their column densities and the total column density, as we look for the way to trace the structure of the cloud.

Contents

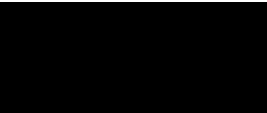
Abstract (Deutsch/English)	iii
List of figures	viii
List of tables	x
1 Introduction	1
1.1 Phenomenology of Molecular Clouds	2
1.2 The Lifetime of Giant Molecular Clouds	5
1.3 Molecular Cloud Formation	6
1.4 Chemistry of Molecular Clouds	8
1.4.1 Gas thermal balance	9
1.5 Modelling Molecular Cloud Formation	12
1.5.1 Grid-based codes	14
1.5.2 Equations to solve	15
1.5.3 Equation of state (EOS)	17
1.5.4 Adaptive mesh refinement (AMR)	18
2 Modelling H₂ Formation in the Turbulent ISM	21
2.1 – Prologue –	22
2.2 Numerical Method	23
2.2.1 Chemistry and cooling	23
2.2.2 Turbulent driving and hydrodynamics	25
2.2.3 Initial conditions	26
2.2.4 Numerical resolution	28
2.3 Results	29
2.3.1 Time dependence of H ₂ abundance	29
2.3.2 Density and temperature distributions	32
2.3.3 Dependence on the density clumping factor	34
2.4 Summary	42

3	Cloud Formation in Colliding Flows	45
3.1	– Prologue –	46
3.2	Numerical Model	46
3.2.1	The numerical code and setup	46
3.2.2	Cooling and heating	48
3.3	Results	50
3.3.1	Density and temperature distributions	50
3.3.2	Cloud structure and velocity	55
3.3.3	Clump properties	62
3.4	Summary	64
4	Modelling C I emission	67
4.1	– Prologue –	68
4.2	Numerical Method	69
4.2.1	Radiative transfer	70
4.2.2	The Sobolev approximation	71
4.2.3	C I emission	72
4.3	Results	73
4.3.1	C I column density and intensity distribution	73
4.3.2	C I and CO correlation	75
4.4	Summary	78
5	Conclusions and outlook	81
	Acknowledgements	85
	Bibliography	94

List of Figures

1.1	The "Black Cloud" Bernard 68 (B68) in the Ophiuchus constellation	3
1.2	Looking through the "Black Cloud" Bernard 68 (B68) in the Ophiuchus constellation	4
1.3	Illustration of the computational block in the cartesian grid	18
1.4	Illustration of the adaptive mesh refinement (AMR)	19
2.1	Resolution study on time evolution of the mass-weighted H ₂ abundance in units of the turbulent crossing time	28
2.2	Time evolution of the mass-weighted mean H ₂ fraction	30
2.3	Time evolution of the mass-weighted mean H ₂ fraction in units of the turbulent crossing time	31
2.4	Solenoidal and compressive volume-weighted density PDF	33
2.5	Mean H ₂ fraction, plotted as a function of the number density	35
2.6	Mean gas temperature plotted as a function of the number density	36
2.7	Evolution of the clumping factor	39
2.8	Expanded view of the clumping factor evolution	41
3.1	Mass-weighted density and temperature PDF	51
3.2	2D temperature-density PDF	53
3.3	Time evolution of the mass and volume fractions of the cold gas	56
3.4	Face-on view of the cloud column density	57
3.5	Edge-on view of the cloud column density	58
3.6	Radial velocity distribution in the cloud	60
3.7	Time evolution of the temperature	62
3.8	Statistical properties of the clumps	64
4.1	Relationship between integrated C I intensity and extinction A_V	74
4.2	C I column density and integrated C I intensity PDF	75
4.3	Images of C I column density and integrated C I intensity	76
4.4	Image of C I/CO integrated intensity ratio	77

- 4.5 Relationship between C I/CO integrated intensity ratio and extinction A_V 78
- 4.6 Relationship between column density ratios N_C (and N_{CO})/ N_{tot} and extinction A_V 79
-



List of Tables

2.1	Reactions used in non-equilibrium chemical model	24
2.2	Processes included in non-equilibrium chemical model	25
2.3	Time in Myr when the gas becomes molecular	32
3.1	Reactions in our non-equilibrium chemical model.	49

1 Introduction

Almost all natural light we observe in the sky at optical wavelengths originates from stars. It is either being reflected from our Sun by the Moon and the planets in our solar system, or coming from a star or collection of stars further away. Thanks to the very high brightness of the most massive stars we are able to reach out to the far ends of the universe and understand the physical processes that govern its evolution.

Throughout the millennia, stars have been central to many of our understandings of the universe and cosmic history. They have been the observational targets of traditional astronomy. They define the celestial landscape, the constellations. As very well summarised by McKee & Ostriker (2007): "Stars are the "atoms" of the universe, and the problem of how stars form is at the nexus of much of contemporary astrophysics. By transforming gas into stars, star formation determines the structure and evolution of galaxies. By tapping the nuclear energy in the gas left over from the Big Bang, it determines the luminosity of galaxies and, quite possibly, leads to the reionisation of the universe. Most of the elements – including those that make up the world around us – are formed in stars. Finally, the process of star formation is inextricably tied up with the formation and early evolution of planetary systems". Indeed, to reach the chemical composition observed today in our solar system, the material had to go through many cycles of stellar birth and death.

Because of the central role of star formation in the formation, evolution, and appearance of our galactic home, the Milky Way, understanding the origin of stars, at present and at early times, and the mechanisms

that govern the formation of the sites of their birth are of considerable scientific interest. It has a profound impact on how we see our position in the universe.

1.1 Phenomenology of Molecular Clouds

The birthplaces of stars and their planetary systems are the turbulent interstellar clouds. They mostly consist of molecular gas with a small fraction of dust mixed in. These dense clouds can be seen even with the naked eye on the night sky where they appear as dark, starless patches. The reason we see them as dark patches of obscuration is that at optical wavelengths, the light from stars further away is blocked by dust (see Fig. 1.1). However, at far-infrared, sub-millimetre, and radio wavelengths, the dust becomes increasingly transparent and we are able to look into the clouds (see Fig. 1.2). These observations reveal a large population of massive clouds in our galaxy known as giant molecular clouds (GMCs). GMCs have extremely complex morphological and kinematic structure. They are inhomogeneous systems where the way gas is distributed depends strongly on many physical processes. Usually, the patches of cold high-density gas are found at places surrounded by regions of low-density warmer material (Ferrière 2001). Various studies (Mac Low & Klessen 2004; Elmegreen & Scalo 2004; Scalo & Elmegreen 2004) argue that this could be a global galactic effect caused by a large gravitational motions in the galaxy (such as spiral density waves) or the supersonic turbulence generated by the energy and momentum input from stars themselves causes this complicated texture. The supersonic turbulence within the clouds leads to the compressions of the warm neutral medium (WNM). These compressions non-linearly trigger thermal instability (e.g. Audit & Hennebelle 2005; Vázquez-Semadeni et al. 2007; Hennebelle et al. 2008; Banerjee et al. 2009; Heitsch & Hartmann 2008) which produces the clumpy structure of the cloud. Dense, cold clumps of gas are embedded in a more diffuse, turbulent flow. When some of the resulting density fluctuations exceed the critical mass of gravitational stability, clumps begin to collapse, eventually forming new protostars.

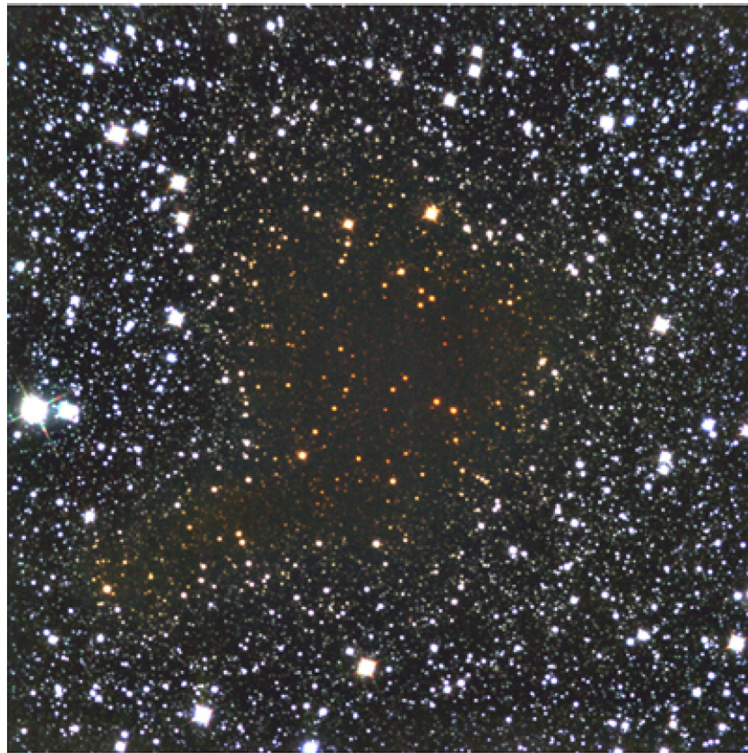
Molecular clouds consist mainly of molecules, with $\geq 98\%$ of their mass being in the form of H_2 and $\leq 1\%$ mass is contributed by numerous 'trace' molecules. Apart from the intercloud medium in the Milky Way and galaxies of lower density that are mostly atomic or in form of ionised hydrogen, the gas in the densest nearby galaxies, such as M64 (Rosolowsky & Blitz 2005), is molecular. Molecular hydrogen is formed in the regions where the gas is sufficiently dense and well-shielded against the dissociating effects of interstellar ultraviolet radiation. It is a homonuclear molecule, so its dipole moment vanishes and it radiates extremely weakly. This makes it extremely difficult



Figure 1.1: The "Black Cloud" Bernard 68 (B68) about 500 light years from Earth towards the Ophiuchus constellation. A concentration of dust and gas in an interstellar cloud absorbs the visible light of background stars, apparently creating a "hole in the sky". Courtesy of FORS team, 8.2 m VLY Antu, ESO.

to observe. The only possible way to detect H_2 is by measuring the absorption of light from bright stars or active galactic nuclei, such as the measurements done by the *Copernicus* and *Far Ultraviolet Spectroscopic Explorer (FUSE)* satellites (Spitzer & Jenkins 1975; Moos et al. 2000; Sahnou et al. 2000). However, because of the atmospheric opacity they can only be done from space. Due to these limitations, most of what is known about the largest clouds comes from observations of the $J = 1 \rightarrow 0$ transition of the carbon monoxide molecule, ^{12}CO , which is the most prominent to be found in the same locations as H_2 and the circumstances conspire to make it easy to observe. The second most common tool for study of the molecular ISM is radio and sub-millimetre emission from dust grains.

High resolution observations of all of the nearby galaxies indicate that the typical masses of GMCs are $\approx 10^4 - 10^7 M_\odot$ with average densities $\sim 100 \text{ H}_2 \text{ molecules cm}^{-3}$ (Solomon et al. 1987). Beside their masses and densities, molecular clouds across the Local Group all seem to have a common surface density of $\approx 170 M_\odot \text{ pc}^{-2}$ ($= 0.035 \text{ g cm}^{-2}$) (Blitz



Looking Through the Dark Cloud B68 (NIT + SOFI)

ESO PR Photo 29a/99 (2 July 1999)

© European Southern Observatory



Figure 1.2: A infrared false-colour image of Bernard 68. Infrared radiation penetrates the molecular cloud more readily than visible light, and many background stars can be seen. Bernard 68 is not a "hole in the sky". Courtesy of FORS team, 8.2 m VLY Antu, ESO.

et al. 2007) and they all display linewidths much greater than it would be expected from thermal motion, given their inferred temperatures of 10 – 20 K.

Magnetic fields also play an important role in the life of a molecular cloud. Given that the gas in molecular clouds is a weakly ionised plasma, it is tied to magnetic field lines. Various observations using Zeeman splitting (Crutcher 1999; Troland & Crutcher 2008) and Chandrasekhar-Fermi effect (Lai et al. 2001, 2002) indicate that the strengths of these magnetic fields cover the range from a few to a few tens of μG . Even though the strength of the magnetic field varies from region to region, the magnetic energy density is in general comparable to the gravitational and turbulent energy densities. We can differentiate between two types of clouds according to the strength of the magnetic field threading them: subcritical and supercritical. The cloud is called subcritical if the magnetic field is sufficiently strong to prevent the gravitational collapse of the cloud

no matter what external pressure is applied to it, as long as it is governed by ideal magnetohydrodynamics (MHD). In contrast, the magnetically supercritical clouds have a weaker magnetic fields that can delay, but never prevent a collapse (Mouschovias & Spitzer 1976). Observations indicate the molecular clouds are close to being, but not quite, magnetically subcritical (Crutcher et al. 2009).

1.2 The Lifetime of Giant Molecular Clouds

Star formation is quite inefficient which is a fundamental problem at the heart of any star formation theory. In individual clouds, star formation rates (SFRs) are difficult to estimate. We can statistically estimate their values with a number of infrared or ultraviolet indicators (Kennicutt 1998). In order to do this, one can calculate the star formation rate in an entire galaxy and compare it to the total mass of molecular gas in a galaxy. The result is that no more than a few percent of the total mass in molecular clouds in a galaxy can be converted into stars per dynamical cloud time (Zuckerman & Evans 1974; Krumholz et al. 2006), meaning that the gas converts into stars very slowly. Namely, molecular clouds should collapse under their own weight within a free-fall time (3×10^6 yr for $n = 100 \text{ cm}^{-3}$). Given the $\approx 10^9 M_{\odot}$ of molecular gas in the Milky Way it would lead to a star formation rate of $\approx 10^3 M_{\odot}/\text{year}$, which is much larger than the few M_{\odot}/year observed. Molecular cloud times can not be derived in this manner, but this calculation has demonstrated the importance of learning about their timescales. The molecular cloud timescales are crucial for explaining this discrepancy found between the observed rate of star formation in molecular clouds and the star formation rate calculated from molecular cloud's parameters.

The structures within molecular clouds span a huge range of mass and size scales which is reflected in the range of characteristic time scales. Because of this, molecular clouds do not have a unique, well-defined lifetime. If we assume that the molecular phase of a molecular cloud lasts as long as the atomic/ionised phase, then the cloud lifetimes in the Milky Way have the values of $10^8 - 10^9$ years. This assumption is necessary to ensure the steady-state gas cycle between molecular hydrogen and atomic/ionised gas (Solomon et al. 1979; Scoville et al. 1979). The mass ratios of molecular to atomic gas that were available at the time suggested the lifetimes of $> 10^8$ years. After it was discovered that the mass ratios were overestimated by at least a factor of five Blitz & Shu (1980), the cloud lifetimes were reduced to a few 10^7 years. The evidence for this claim comes from the observations of spiral arms. The time between two arm passages is approximately 10^8 years. Since there are no molecular clouds between spiral arms, their lifetimes must be substantially shorter than the time between two arm passages.

In the more recent past, two different techniques for estimating the molecular clouds lifetimes emerged. The first is based on the statistical associations between molecular clouds and young star clusters. In a given sample of GMCs there are three classes of clouds that form an evolution sequence: young clouds without HII regions or massive stars formation; clouds that have internal HII regions but where the stars which have created them have not yet become optically visible; and clouds where massive star clusters have blown out enough gas and the stars can be viewed directly. The position of the molecular clouds is correlated with the positions of the star clusters, as a function of star cluster age. This correlation points to the duration of this last phase. With this estimate, one can calculate the duration of entire time sequence from the relative numbers of clouds in each of the three classes. This technique has been applied to the LMC (Blitz et al. 2007) and M33 (Engargiola et al. 2003), giving the cloud lifetimes of 27 Myr and 20 Myr respectively. These age estimates apply only to GMCs masses of $\sim 10^5 M_{\odot}$ or larger.

The second technique is applied to the clouds in nearby star-forming regions that have a maximum mass of $\sim 10^5 M_{\odot}$. With this method, molecular cloud age estimate can be obtained independently from the ages of individual young stars within that region. Hartmann et al. (2001) and Ballesteros-Paredes & Hartmann (2007) have shown that the stellar populations older than $\approx 5 \times 10^6$ years are generally not associated with molecular gas anymore, suggesting that molecular clouds can last only for timescales substantially shorter than 10^7 years in order to produce the observed compilation of stellar ages in local star-forming clouds. It has been suggested that the ages of the nearby star clusters span the range from less than 1 Myr up to 3 Myr (Palla & Stahler 2000; Hartmann 2003; Huff & Stahler 2006).

1.3 Molecular Cloud Formation

Being the hosts of all observed Galactic star formation, understanding how GMCs form and evolve has been an important goal of star formation research. However, this still remains an unsolved problem. Traditionally, molecular clouds were viewed as being virialised structures in the interstellar medium (ISM), having relatively long lifetimes and a significant delay between the formation of the cloud and the onset of star formation (see e.g. Zuckerman & Palmer 1974; Woodward 1978; Scoville & Hersh 1979). The reasoning for virial equilibrium, and thus the general stability and longevity of the clouds, was found in the fact that gravitational energy of GMCs, that also exceeds the thermal energy of the clouds by far, is near equipartition with their turbulent and magnetic energies. The fact that molecular clouds have thermal pressures that are roughly one order of magnitude greater than those of the general

ISM is seen as a consequence of the strong self-gravity of the clouds. The magnetic and turbulent energies that provide the support against gravity cannot be incorporated into global ISM models based on thermal pressure equilibrium, such as those by Field et al. (1969); McKee & Ostriker (1977); Wolfire et al. (1995).

Having concluded that the maximum lifetimes of GMCs are $\lesssim 30$ Myr (see section 1.2), the scientific community has encountered the issue of the gas accumulation in the existing models of cloud formation. In order to build a molecular cloud the assembling gas has to reach a column density high enough so that the dust could shield the cloud against the dissociating ambient UV-radiation, and allow molecule formation. Dust shielding becomes efficient at column densities of approximately $N = 2 \times 10^{21}$ cm. With this in mind, and having that the typical values of 1 cm^{-3} for densities and 10 km s^{-1} for velocities for the inter-arm ISM where clouds form, it would take 60 Myr to accumulate the shielding column density, which is obviously too large. Parker (1966) was the first to suggest the mechanism, today known as Parker instability, that allows the formation of molecular clouds within realistically short times. With this mechanism, the accumulation would have a timescale of 30 Myr and would take place of 1 kpc along spiral arms. However, only weak signatures of a Parker instability acting along a spiral arm have been found (Kim & Ostriker 2006).

Finally, the recent studies have suggested that GMCs begin forming stars shortly after they themselves form, and are non-equilibrium entities (see e.g. Ballesteros-Paredes et al. 1999a,b; Elmegreen 2000; Hartmann et al. 2001; Vázquez-Semadeni et al. 2003, 2006). Their formation and evolution are dominated by the effects of supersonic turbulent motions (see e.g. Larson 1981; Myers 1983; Solomon et al. 1987; Falgarone et al. 1992; Heyer & Brunt 2004 and the reviews by Mac Low & Klessen 2004; Elmegreen & Scalo 2004; Scalo & Elmegreen 2004; McKee & Ostriker 2007; Klessen et al. 2009) and are rapid, with a timescale comparable to those of important chemical processes such as the conversion of atomic to molecular hydrogen or the freeze-out of molecules onto the surfaces of interstellar dust grains. This mechanism operates on a scales of tens to hundreds of pc. The supersonic flows involved in this scenario can be produced by a number of different sources. For example, it can be supernova explosions that drive blast waves and superbubbles into the ISM which in combination with supernova remnants and expanding HII regions further drive a turbulent flow. The turbulence could also be caused by magnetorotational instability (Balbus & Hawley 1998) in galaxies that can have velocity dispersion close to that of supernova-driven turbulence even in regions far from recent star formation. Regardless of the turbulence source, the cloud forming flows have a velocity dispersion of $\sim 10 \text{ km s}^{-1}$.

1.4 Chemistry of Molecular Clouds

What determines the chemistry in general is the average density of molecules and their temperature. These two quantities indicate how often molecules collide with one another and with what energy. But not all collisions result in a chemical reaction. Whether a chemical reaction occurs depends on what has to happen to the reactants to become products. In case of molecules, for example, there must be sufficient energy in the collision in order to break a bond. Too much energy results in the bonds of the target reactant being broken. The available energy is measured by the local temperature.

All physical conditions and the molecules available within the local environment on which chemistry depends are controlled by the rate of chemical reactions under the local conditions. The reaction rate is related to the concentration of the species multiplied by a rate constant. Measurements of rate constants in the laboratory show that rate constants follow an empirical temperature dependence called the Arrhenius equation:

$$k(T) = A \exp\left(-\frac{E_a(T)}{RT}\right) \quad (1.1)$$

where A is the temperature dependent pre-exponential factor which varies depending on the order of the reaction, T is temperature, a E_a is the activation energy for the reaction and R is the gas constant. Given that the radicals are extremely reactive, activation energy for radical reaction is zero.

The reaction rate constants for explosions, atmospheres and astrophysical environments are used to calculate the rate coefficient. For two-body reactions for example, the rate coefficient based on the Arrhenius law is given by:

$$k(T) = \alpha \left(\frac{T}{300}\right)^\beta \exp\left(-\frac{\gamma}{T}\right) \quad [\text{cm}^3 \text{ s}^{-1}] \quad (1.2)$$

where α , β and γ are either fitted experimental parameters, derived from theory or in worst cases best guesses. For cosmic-ray-induced photoreactions the rate coefficient is

$$k(T) = \alpha \left(\frac{T}{300}\right)^\beta \frac{\gamma}{1 - \omega} \quad [\text{s}^{-1}] \quad (1.3)$$

where α is the cosmic-ray ionisation rate, γ is the probability per cosmic-ray ionisation that the appropriate photoreaction takes place, and ω is the dust grain albedo in the

FUV. For interstellar photoreactions, the rate is derived as:

$$k(T) = \alpha \exp(-\gamma A_V) \quad [\text{s}^{-1}] \quad (1.4)$$

where α represents the rate in the unshielded interstellar ultraviolet radiation field, A_V is the extinction at visible wavelengths caused by interstellar dust, and γ is the parameter used to take into account the increased extinction of dust at ultraviolet wavelengths.

There is a huge number of chemical reactions that must be considered for networks of chemical processes, whether within a cold dark cloud, a giant molecular cloud, the atmosphere of a planet or other astrophysical environments. Generally, the reactions can be categorised into various classes and the inclusion of such classes depends on the physical properties of the medium to be modelled.

In the ISM, the influence of chemical reactions on the properties of gas and ongoing processes within the gas is tremendous. The presence of various chemical species and their transitions between different phases and energetic states influence the thermal and dynamical evolution of a gas cloud by modifying the cooling ability of the gas. Dust grains are also important as their interactions are observable in a large range of wavelengths with a well defined temperature. As such, they accelerate chemical reactions by providing the excess energy during collisions. In contrast the chemical reactions in the gas phase are much more difficult because atoms and small molecules do not interact as often. In most atomic collisions in the gas phase, the atoms simply bounce off instead of undergoing a chemical reaction. The influence of chemical reactions on the properties of gas and ongoing processes within the gas is enormous. Optical properties of dust grains change under the influence of atoms and molecules and if covered with water or CO ice, the grains have a significantly different optical behaviour. Therefore, physical properties of some observed region rely on the chemical processes. Also, transition lines of different molecules and metals can be used to trace the gas in different regimes which influences the observations. As the result, the formation and destruction of molecules directly influences the interpretation of observations. Chemistry also affects the micro-physics and thus the ability of the gas to respond to the changes in density and temperature. This leads to changes in the equation of state which then directly leads to changes in the hydrodynamic evolution.

1.4.1 Gas thermal balance

Heating of the cloud occurs through cosmic rays and radiation. Photoelectric heating is the dominant process at the surface of molecular clouds. Far-ultraviolet (FUV)

photons hitting a dust grain can create energetic (several eV) electrons. While these electrons diffuse in the grain, they will lose energy through collisions. However, if during this diffusion process they reach the surface with enough energy to overcome the work of the grain and the coulomb potential, they can be injected into the gas phase with excess kinetic energy. The efficiency of ejecting a photoelectron for each incoming photon is close to one for very small grains. In grains that are larger than the typical mean free path of the electron inside the grain, this efficiency drops significantly as the photoelectron has a higher probability to be re-absorbed inside the grain. Note that, even though the photodissociation of molecules is very efficient at the surface of molecular clouds, it is generally a minor heat source. For molecules other than H_2 , the low abundance ($< 10^{-3}$) coupled with typical chemical reaction energies of $\sim 1\text{eV}$ mean that a single formation or destruction of a molecule leads to little heating ($\Delta T < 10\text{ K}$). Therefore, appreciable heating results only when molecules are destroyed and re-formed through many cycles. In such a cycle a hydrogen molecule needs to be formed for each molecule re-formed. Therefore, the heating by photodissociation can be significant only if the energy released per dissociation is greater than the energy released per H_2 formation.

Cosmic rays interact with the interstellar medium via the ionisation of atomic and molecular hydrogen,



which heats up the gas and couples the charged current to the ambient magnetic field. They mainly consist of relativistic protons and a mixture of heavy elements such as iron and electrons. Their energies span a large range between $10\text{--}10^{14}\text{ MeV}$ (see Beatty & Westerhoff 2009). Cosmic ray ionisation has an attenuation length of 96 g cm^{-2} , thus it is the only remaining heating process deep inside molecular clouds. Photons cannot reach here due to the high extinction.

Most of the cooling in molecular clouds is due to collisional ionisation of atoms or molecules and subsequent radiation of a photon that escapes the cloud. The dominant molecular coolants in astrophysical gases are H_2 , ^{12}CO , ^{13}CO , H_2O and OH . As the fraction of molecular hydrogen becomes larger than 1%, H_2 line cooling becomes important and molecular line emission (mainly CO and H_2) cools the gas down to below hundred K. Collisional dissociation of molecules other than H_2 is completely negligible unless the molecules are re-formed and recycled. Re-forming molecules

requires the presence of H_2 . Since H_2 dissociates at a relatively low energy and H_2 is present when molecules recycle, H_2 dissociative cooling dominates all other molecular dissociative cooling rates when dissociative cooling is significant.

Most of the cooling in the warm neutral medium ($T \sim 8000$ K) originates from Lyman- α emission from atomic hydrogen, electron recombination with small grains and PAHs, and fine-structure emission from atomic oxygen (Wolfire et al. 1995, 2003). In the regime of the cold neutral medium ($T < 300$ K), most of the cooling comes from fine-structure emission from ionised carbon, C^+ . Fine-structure emission from oxygen becomes significant in the warmer parts of the CNM. In the thermally unstable temperature regime $300 \text{ K} < T < 8000 \text{ K}$ also C^+ and O cooling play an important role.

Dust grains can also cool the gas if the dust temperature is lower than that of the gas. In that case, gas particles and dust grains will collisionally exchange energy, not affecting the dust radiative equilibrium.

The resulting heating and cooling rate of the gas can be described as a function of the gas density n and temperature T . In the diffuse, warm interstellar gas the heating rate scales (roughly) as

$$\Gamma = \gamma n \tag{1.7}$$

where γ is assumed to be independent of the temperature of the medium, although this restriction is not essential. On the other hand, the energy radiated in the dominant cooling lines scales as

$$\Lambda = \lambda(T) n^2 \tag{1.8}$$

where λ scales as $\sim T$. If the heating and cooling of the gas are in equilibrium, $\Lambda = \Gamma$, anything causing even a small density increase would lead to cooling instability (Field 1965). If the sound-crossing time of the density perturbation is less than its cooling time, then the gas cools. As the temperature of the gas falls, the compressions of the surrounding warmer medium increase the density. The cooling rate is increasing with growing density, but at the same time it is being reduced by the drop in temperature. If the temperature dependence of the cooling rate is weak, then the cooling rate increase is greater than its decrease and the density is growing ever faster. This process will stop when the density dependence of the cooling rate changes. This happens when the level populations of the dominant coolants reach their local thermodynamic equilibrium values. In this case the cooling rate scales only as n . The cooling instability also stops when the temperature dependence of the cooling rate becomes steeper, e.g. at low

temperatures. In the ISM, the thermal instability vanishes once $n \sim 100 \text{ cm}^{-3}$ and $T \sim 50 \text{ K}$ (Wolfire et al. 2003), when the gas develops a two-phase structure (Burkert & Lin 2000; Heiles & Troland 2003).

1.5 Modelling Molecular Cloud Formation

The dynamics and chemistry of the gas are strongly coupled, with one directly influencing the evolution of the other, and they must be modelled together. A promising theory for producing GMCs, as well as for generating turbulence within them, suggests that these clouds form in places where streams of warm atomic gas collide. Work by a number of different groups has shown that the dense sheets and filaments that build up at the interface of the colliding flows become thermally unstable (e.g. Audit & Hennebelle 2005; Vázquez-Semadeni et al. 2007; Hennebelle et al. 2008; Banerjee et al. 2009; Heitsch & Hartmann 2008). The compressed unstable gas rapidly radiates away most of its thermal energy, significantly decreasing its temperature. As the temperature of the gas falls, it is compressed by the warmer material surrounding it, and so the large drop in temperature is associated with a large increase in density. In some regions, strong pressure gradients are created that then act to drive turbulent flows throughout the interaction region. The outcome is a set of dense, cold clumps of gas, embedded in a more diffuse, turbulent flow, and with a filamentary morphology reminiscent of that found by observations of real GMCs (e.g. Men'shchikov et al. 2010; Arzoumanian et al. 2011). Since the dense clumps observed in real GMCs are known to be the sites at which stars form, these results suggest that there is an important link between the large scale physics of GMC formation and the smaller scale physics of star formation.

The formation of molecular clouds by converging flows in the warm neutral medium has been intensively studied in recent years. Various numerical and analytical models have been presented by Ballesteros-Paredes et al. (1999a); Hennebelle & Pérault (1999); Koyama & Inutsuka (2000, 2002); Hartmann et al. (2001); Audit & Hennebelle (2005); Vázquez-Semadeni et al. (2006, 2007); Heitsch & Hartmann (2008), etc. Unfortunately, most three-dimensional studies of this process performed so far make use of highly simplified treatments of the thermal energy balance of the gas. Heating and cooling are modelled using simplified parameterisations that assume that the rates are functions only of density and temperature, and that ignore the effects of chemical changes or dust shielding (see e.g. Vázquez-Semadeni et al. 2007; Banerjee et al. 2009). No effort has been made to determine whether this simplified approach is adequate for describing the dynamics of the gas, or whether we would expect to find significant changes in behaviour if we were to use a more detailed chemistry and cooling model. Given

models are unable to determine when the gas first becomes molecular. This has made it difficult to directly compare the clouds formed in these simulations with observations of real GMCs in a meaningful fashion, and so has greatly limited the usefulness of these studies.

With this thesis, we present our attempt to improve on this situation. The study described here is based on our high-resolution 3D simulations of molecular cloud formation that for the first time include self-consistent model of the assembly of the clouds, the thermal energy balance within them, and chemical evolution of the gas. There are three main scientific objectives we want to address here.

- We want to understand how the use of a more accurate thermal model affects the dynamics of the flow, and the properties of the clumps that are formed. In particular, we expect that the inclusion of the effects of dust shielding will have a large impact on the temperature of the dense gas, making it far easier for this material to become gravitationally unstable and to start forming stars.
 - We want to determine how quickly observable GMCs form in these convergent flows. The timescale on which the dense gas is assembled is well known from current studies, but because these studies do not account for the chemical evolution of the gas, they are unable to determine when the molecular fraction of the gas first becomes large enough to render the cloud detectable in carbon monoxide (CO) emission. By quantifying when the cloud first becomes detectable, and how this compares to the time at which star formation begins, we will be able to determine what fraction of observed GMCs should have not yet begun forming stars. This can then be tested against observations.
 - We want to determine the detailed distribution of C I and CO in the assembling GMCs. Observations of CO are regularly used to infer cloud properties, but until we can understand how the gas traced by the CO relates to the overall gas distribution, we cannot be certain that the observations are not giving us a biased picture of the underlying cloud. We will investigate this by post-processing our simulation results to generate simulated observational maps of the C I and CO emission. These simulated maps can then be analysed using the same tools as are used in the analysis of real observations, and the inferred properties of the clouds can then be compared with their actual properties, allowing us to uncover the biases of the analysis techniques.
-

1.5.1 Grid-based codes

Modelling the thermal evolution of the gas in a meaningful fashion and having a full chemical model of the ISM can easily require one to track several hundred different atomic and molecular species involved in several thousand different reactions, even if reactions on grain surfaces are neglected (see e.g. the UMIST Database for Astrochemistry, as described in Woodall et al. 2007). This is impractical to include in a 3D hydrodynamical code, since it would have an extreme impact on the code's performance. In order to run time-dependent chemical networks efficiently alongside the dynamical evolution of the system one needs to select a number of chemical species and mutual reactions such that the chemical network can be solved in a short enough time while still adequately describing the overall evolution of the system (see Glover & Mac Low 2007a,b). For our purposes we need to be able to follow the formation and destruction of H_2 with a reasonable degree of accuracy (see chapter 2).

To reach these goals, we use and modify the grid based massively parallelised FLASH code in version 2.5, developed by the Center for Astrophysical Thermonuclear Flashes at the University of Chicago (Fryxell et al. 2000). It has initially been designed for thermonuclear runaway problems but it also has support for a variety of different physical processes, including magneto-hydrodynamical (MHD) flows and self-gravity. The most appealing feature of the code is the ability to configure initial and boundary conditions, change algorithms, and add new physics modules with less effort than in other AMR codes. It uses the PARAMESH library to manage a block-structured adaptive grid so that the resolution elements are placed only where they are needed most. For parallelisation is used the Message-Passing Interface (MPI).

Our modifications add a limited treatment of non-equilibrium chemistry treated in an operator-split fashion (Glover & Mac Low 2007a,b). They include a detailed atomic/molecular cooling function and a simplified but accurate treatment of the most important hydrogen chemistry described section 2.2.1. During each hydro step, the coupled set of chemical rate equations for the fluid are solved using the implicit integrator DVODE (Brown et al. 1989), together with the portion of the internal energy equation dealing with compressional and radiative heating and cooling, under the assumption that the other hydrodynamical variables (e.g. density) remain fixed. The advection of the gas energy density is handled as in the unmodified FLASH code.

Chemical abundances in the model are tracked using FLASH standard tracer field implementation. In order to reduce the advection errors, we use the consistent multispecies advection (CMA) (Plewa & Müller 1999). Namely, total flux of element a

with mass fraction x_a is

$$F_a = x_a F_\rho. \quad (1.9)$$

However, the partial fluxes F_i of the species in the element, in general do not sum the total flux F_a

$$F_a \neq \sum_i F_i. \quad (1.10)$$

Hence, in order to assure the conservation law, we have to rescale the fluxes by a factor

$$\phi = \frac{F_a}{\sum_i F_i} \quad (1.11)$$

This method is determined via the runtime parameter *use_cma_advection*.

1.5.2 Equations to solve

The grid-based methods divide the computational domain into small volume elements and follow the fluxes of all relevant quantities from one cell to the other. Since the flow is followed from fixed positions in space, the code solves Eulers equations formulated through a set of partial differential equations such that they relate different flow properties (such as density and velocity) with each other and with thermodynamic quantities (e.g. pressure, temperature or internal energy of the medium). For compressible gas dynamics in three spatial dimensions, neglecting the effects of viscosity, these equations have the following form (Fryxell et al. 2000):

$$\frac{\partial \rho}{\partial t} + \nabla \cdot (\rho \mathbf{v}) = 0 \quad (1.12)$$

$$\frac{\partial(\rho \mathbf{v})}{\partial t} + \nabla \cdot (\rho \mathbf{v} \mathbf{v}) + \nabla P = \rho \mathbf{g} \quad (1.13)$$

$$\frac{\partial \rho \mathbf{v}}{\partial E} + \nabla \cdot [(\rho E + P) \mathbf{v}] + \nabla P = \rho \mathbf{v} \cdot \mathbf{g} \quad (1.14)$$

with ρ being the fluid density, \mathbf{v} velocity, P pressure, \mathbf{g} the gravitational acceleration due to self-gravity, and t the simulation time. The total energy per unit mass, E

represents the sum of kinetic and internal energy:

$$E = \varepsilon + \frac{1}{2}|\mathbf{v}|^2. \quad (1.15)$$

The pressure is obtained from the energy density via

$$P = (\gamma - 1)\rho\varepsilon \quad (1.16)$$

with γ being the ratio of the specific heats. The gravitational acceleration is computed by solving the Poisson equation

$$\nabla^2\phi = 4\pi G\rho. \quad (1.17)$$

Instead of solving the equations for the entire domain, which gets highly challenging in high-resolution simulations, these equations are solved in operator splitting fashion. Following the equations above, it is clear that the gravitational source terms influence the density field in equations 1.13 and 1.14, deciding the following evolution of the equations. However, at the same time, changing density values leads to a change in velocity field (Eq. 1.12). In ideal case, the Euler's equations would be solved simultaneously with the Poisson equation 1.17, but that is computationally highly impractical. Instead, with operator splitting scheme, first we evolve the Euler's equations for half of the desired time step Δt . Then, the gravitational potential gets updated with the solution of the Poisson equation and after that the equations are advanced for the second half of the time step.

Note that by default the internal energy in FLASH is computed by subtracting the specific kinetic energy from the total specific energy (Eq. 1.15). However, in regions where the kinetic energy greatly dominates the total energy due to truncation error this approach can lead to unphysical (e.g. negative) internal energies, giving inaccurate values for pressures and temperatures. This problem can be avoided by evolving the internal energy separately, using the equation

$$\frac{\partial\rho\varepsilon}{\partial t} + \nabla \cdot [(\rho\varepsilon + P)\mathbf{v}] - \mathbf{v} \cdot \nabla P = 0, \quad (1.18)$$

where ρ is the density and P is the gas pressure. The method used within the FLASH code is determined via the runtime parameter *eint_switch*. If the internal energy is smaller than *eint_switch* times the kinetic energy, then the total energy is recomputed using the internal energy from Eq. 1.18 and the velocities from the momentum equation. We have found that by setting *eint_switch* = 10^{-4} , we are able to avoid any problems due to truncation error.

1.5.3 Equation of state (EOS)

Given that the number of variables in the set of equations that needs to be solved is larger than the number of equations, it is necessary to introduce an additional relation, called equation of state (EOS), in order to obtain the unique solution. The purpose of EOS is to define the pressure as function of other thermodynamic variables (see Pompe 1985).

The equation of state for an ideal gas has the form of

$$PV = NkT \quad (1.19)$$

with P being the pressure, V the volume, N the total number of gas particles, k the Boltzmann constant, and T the temperature. As seen in section 1.5.2, the ideal gas law may also be expressed as

$$P = (\gamma - 1)\rho\varepsilon \quad (1.20)$$

where γ is the adiabatic index $\gamma = c_p/c_v$, $\varepsilon = c_v T$ is the internal energy per unit mass (specific internal energy), c_v is the specific heat at constant volume, and c_p is the specific heat at constant pressure. The adiabatic equation of state relates the pressure to the density like

$$P = K\rho^\gamma, \quad (1.21)$$

with K being a constant.

The advantage of these approaches is in circumventing the complexity of physical processes and interactions in large range of densities. However, Boley et al. (2007) have recently pointed out that as the temperature of molecular gas increases, its specific heat capacity at constant volume, c_v , changes due to the fact that first the rotational and then the vibrational energy levels of H_2 become populated and that therefore c_v cannot be considered constant and independent of temperature as has been often assumed in previous numerical studies of star formation. For this reason, we have modified our treatment of the adiabatic index γ . Instead of solving EOS equation, we setup a new EOS module inside the FLASH code that uses a set of lookup tables constructed with the assumption that the H_2 ortho-to-para ratio has its thermal equilibrium value. In these tables, the specific internal energy ε is tabulated as a function of temperature T and fractional abundance of H_2 (x_{H_2}), T is tabulated as a function of ε and x_{H_2} , and the adiabatic index γ is tabulated as a function of ε (or T) and x_{H_2} . To compute the required values for γ or convert from ε to T (or vice versa), we interpolate between

the values stored in the tables. This technique speeds-up the code ten times and more.

1.5.4 Adaptive mesh refinement (AMR)

Numerical solutions to partial differential equations always require to consider a discrete set of points instead of continuous space and time dimensions. The equations above are solved on a cartesian grid, organised in blocks of 8^3 cells per block (see Fig. 1.3). Each block is surrounded by so-called guard cells or ghost cells, that are used to transport the necessary information between the border of the block and the neighbouring CPU. Within one block, the cells have equal sizes in all three dimensions. The cell size determines the spatial resolution of the code.

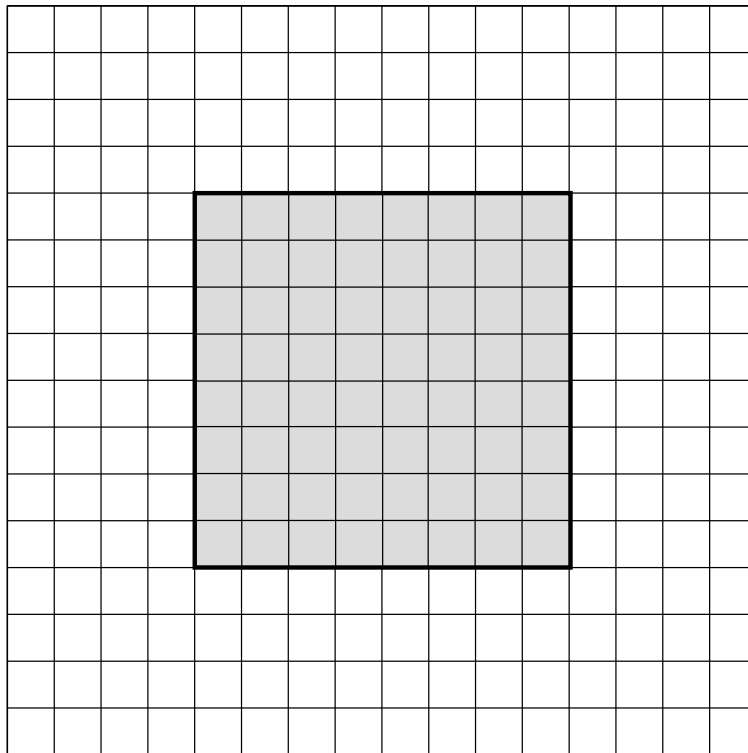


Figure 1.3: Computational block consisting of 8^3 cells (grey cells). A copy of the cells of the neighbouring block is stored in the *ghost cells*, shown in white.

Wherever higher resolution is needed, it can be achieved by refining the grid. This so-called adaptive mesh refinement (AMR) splits the cell in two equal parts in each dimension of the simulation, see Fig. 1.4. There are a number of different approaches to AMR in the literature (Plewa et al. 2005). In a grid-based code it is easy to define or change the criteria for refinement. Whenever a desired quantity exceeds a threshold value, the local grid cell splits. The AMR codes adapt easily to arbitrary complicated

boundaries, however, constructing the mesh is very time consuming and is memory limited. The latter is a simple result of the increasing number of computational elements that have to be stored in the memory of the computer. The more computational cells a simulation contains, the more CPU time is needed to process them.

The time limiter is used to prevent any information to travel more than one computational zone per time step. That way, this so-called 'cfl' parameter ensures the stability of the numerical solution. The maximum evolutionary time step scales as $\Delta t = C \cdot \Delta x$, where the Courant number C is a prefactor that is determined by cfl parameter and is required to be less than 1. Therefore, with decreasing the size of the cell due to the refinement, the time step will also decrease.

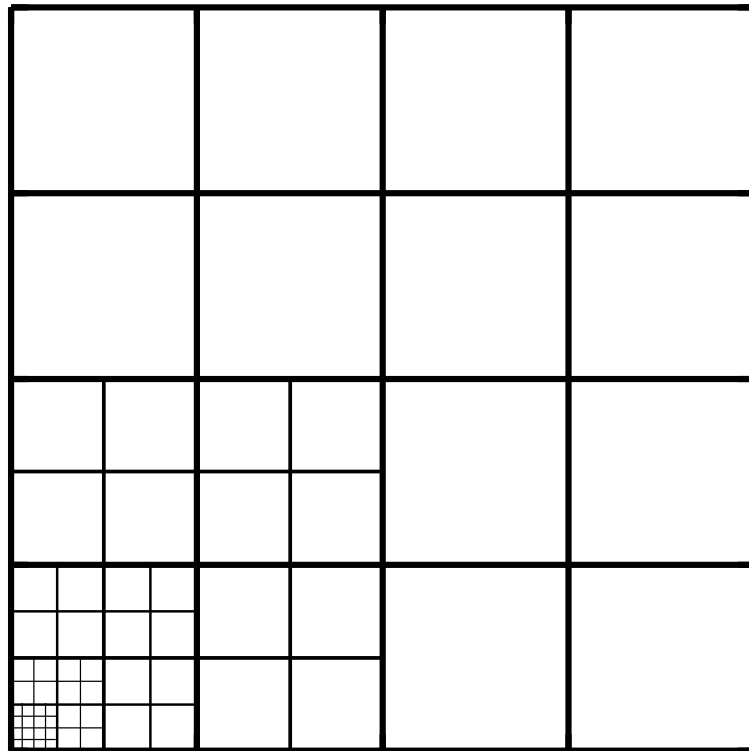


Figure 1.4: Illustration of the adaptive mesh refinement (AMR) in two dimensions. Local cells are split in half in each dimension of the domain.

What equations do not include explicitly is the diffusion of the numerical scheme based on the grid. In case when the motions on the smallest level of the refinement can not be resolved any more, they wash out and diffuse within one cell. This numerical diffusion can dissipate energy even on scales larger than the local minimum cell size. For example, Federrath et al. (2011) have determined that minimum resolution of roughly 30 cells is needed in order to avoid numerical diffusion for turbulent motions. Particular problem occurs when the diffusion scale varies, because it also varies the

energy in the domain. Various solutions have been proposed by Braun & Schmidt (2012) to adequately compute the kinetic energy at the resolution limit. However, these methods have been developed fairly recently and are still not implemented.

2 Modelling H_2 formation in the turbulent ISM: Solenoidal versus compressive turbulent forcing

In this chapter we present results from high-resolution three-dimensional simulations of the turbulent interstellar medium that study the influence of the nature of the turbulence on the formation of molecular hydrogen. We have examined both solenoidal (divergence-free) and compressive (curl-free) turbulent driving, and show that compressive driving leads to faster H_2 formation, owing to the higher peak densities produced in the gas. The difference in the H_2 formation rate can be as much as an order of magnitude at early times, but declines at later times as the highest density regions become fully molecular and stop contributing to the total H_2 formation rate. We have also used our results to test a simple prescription suggested by Gnedin et al. (2009) for modelling the influence of unresolved density fluctuations on the H_2 formation rate in large-scale simulations of the ISM. We find that this approach works well when the H_2 fraction is small, but breaks down once the highest density gas becomes fully molecular.

2.1 – Prologue –

The main chemical constituent of the molecular gas is molecular hydrogen, H_2 , with other molecules such as CO being present only in small amounts, so in practice the study of the formation of molecular gas is usually simply the study of the formation of H_2 . The molecule forms in the interstellar medium primarily on the surface of dust grains. Its formation in the gas phase by radiative association is highly forbidden due to the molecule's lack of a permanent dipole moment and occurs at a negligibly slow rate (Gould & Salpeter 1963), while the gas phase formation via intermediate molecular ions such as H^- or H_2^+ is strongly suppressed by the interstellar radiation field (Glover 2003) and cannot produce molecular fractions much higher than $x_{\text{H}_2} \simeq 10^{-3}$.

Given the relatively slow rate at which H_2 forms, it is natural to ask whether it is possible to produce large amounts of H_2 quickly enough for a model involving rapid cloud formation to be viable. Glover & Mac Low (2007b) have shown that dynamical processes such as supersonic turbulence have a great impact on the effective H_2 formation rate. The presence of turbulence dramatically reduces the time required to form large quantities of H_2 . The density compressions created by supersonic turbulence allow H_2 to form rapidly, with large molecular fractions being produced after only 1–2 Myr, consistent with the timescale required by rapid cloud formation models. It is found that much of the H_2 is formed in high density gas and then transported to lower densities by the action of the turbulence (Federrath et al. 2008a), a phenomenon that certainly has a significant impact on the chemistry of the ISM.

One issue not addressed in the study by Glover & Mac Low (2007b) was the sensitivity of these results to the nature of the turbulent velocity field. Most of the work that has been done to date on the numerical modelling of molecular cloud turbulence has focussed on either purely solenoidal (i.e. divergence-free) turbulence, or weakly compressive turbulence where the solenoidal modes dominate over the compressive (curl-free) modes (see e.g. Klessen et al. 2000; Klessen 2001; Ostriker et al. 2001; Lemaster & Stone 2008). The study by Glover & Mac Low (2007b) is no exception, as it used the same setup for generating weakly compressive turbulence as in earlier work by Mac Low et al. (1998) and Mac Low (1999). Recently, however, Federrath and collaborators have performed a number of studies of fully compressive turbulence (Federrath et al. 2008b, 2009; Schmidt et al. 2009; Federrath et al. 2010). They show that compressive turbulence produces a significantly broader spread of densities than solenoidal turbulence with the standard deviation of the density probability distribution functions (PDFs) differing by a factor of 3 at the same rms Mach number and argue that while solenoidal forcing of turbulence is likely to occur in quiescent regions with low star formation rates like in the Polaris Flare and or Maddalena's Cloud, regions

with a higher star formation activity are more compatible with compressive turbulence (see also, Federrath et al. 2010; Brunt 2010; Price et al. 2011).

The influence of the wide spread of densities produced by compressively driven turbulence on the rate at which molecular hydrogen forms in the ISM has not previously been investigated, but given the strong density dependence of the H₂ formation rate, it is plausible that the effect could be large. To address this issue, we have carried out a numerical investigation of the rate at which H₂ forms in interstellar gas dominated by compressive turbulence, and how this compares to the H₂ formation rate in gas dominated by solenoidal turbulence.

The outline of this chapter is as follows. In §2.2 we describe our numerical method, paying particular attention to the treatment of chemistry and cooling, as well as the method used to generate and maintain turbulence in the gas. In §2.3 we present our results for the H₂ formation rate, and discuss the distributions of density, temperature and H₂ abundance generated in the simulations. We also use our results to test the sub-grid scale model for H₂ formation in turbulent gas put forward by Gnedin et al. (2009). We close with a summary of our findings in section 2.4.

2.2 Numerical Method

We have modified the FLASH v2.5 adaptive mesh refinement code (Fryxell et al. 2000; Calder et al. 2002) to include a detailed atomic/molecular cooling function and a simplified but accurate treatment of the most important hydrogen chemistry (Glover & Mac Low 2007a,b). The overview of our modifications is presented in sections 1.5.1–1.5.3.

2.2.1 Chemistry and cooling

We treat the cooling coming from metals by assuming that the carbon, oxygen and silicon in the gas remain in the form of C⁺, O and Si⁺, respectively, as in the previous studies of Glover & Mac Low (2007a,b). In practice, in the absence of photodissociating radiation (see below), we would expect carbon and silicon to rapidly recombine, and for the carbon to be converted to CO once the H₂ fraction becomes large. However, we know from previous work (Glover & Clark 2012a,b) that the behaviour of the gas is not particularly sensitive to whether the dominant coolant is C⁺ or CO. Cooling from C⁺ alone can reduce the gas temperature to values around 15–20 K, and although CO cooling enables the gas to reach even lower temperatures ($T \sim 10$ K), in realistic

Table 2.1: Reactions in our non-equilibrium chemical model.

No.	Reaction	Reference
1	$\text{H} + \text{H} + \text{grain} \rightarrow \text{H}_2 + \text{grain}$	1
2	$\text{H}_2 + \text{H} \rightarrow \text{H} + \text{H} + \text{H}$	2
3	$\text{H}_2 + \text{H}_2 \rightarrow \text{H} + \text{H} + \text{H}_2$	3
4	$\text{H}_2 + \text{e}^- \rightarrow \text{H} + \text{H} + \text{e}^-$	4
5	$\text{H} + \text{c.r.} \rightarrow \text{H}^+ + \text{e}^-$	See §2.2.3
6	$\text{H}_2 + \text{c.r.} \rightarrow \text{H} + \text{H}$	See §2.2.3
7	$\text{H}_2 + \text{c.r.} \rightarrow \text{H} + \text{H}^+ + \text{e}^-$	See §2.2.3
8	$\text{H} + \text{e}^- \rightarrow \text{H}^+ + \text{e}^- + \text{e}^-$	5
9	$\text{H}^+ + \text{e}^- \rightarrow \text{H} + \gamma$	6
10	$\text{H}^+ + \text{e}^- + \text{grain} \rightarrow \text{H} + \text{grain}$	7

References: 1: Hollenbach & McKee (1979), 2: Mac Low & Shull (1986), 3: Martin et al. (1998), 4: Trevisan & Tennyson (2002), 5: Abel et al. (1997), 6: Ferland et al. (1992), 7: Weingartner & Draine (2001a)

models of GMCs, the characteristic temperature of the fully molecular gas is generally in the range of 10 – 20 K (Glover & Clark 2012b). As the H_2 formation rate does not have a strong dependence on temperature, the approximate nature of our thermal treatment will have little influence on the H_2 formation rate in the gas. However, making this simplification allows us to minimize the computational requirements for our simulations by using a considerably simplified chemistry that follows only four species: free electrons, H^+ , H , and H_2 . We follow directly the fractional abundances of molecular hydrogen x_{H_2} and ionised hydrogen x_{H^+} (where these symbols denote the fraction of the available hydrogen found in these forms) by adding to the FLASH code an extra field variable for the mass density of each species. The abundances of the other two species - atomic hydrogen (x_{H}) and electrons (x_{e}) - are computed from the two conservation laws: conservation of charge

$$x_{\text{e}} = x_{\text{H}^+} + x_{\text{C}^+} + x_{\text{Si}^+} \quad (2.1)$$

and conservation of the number of hydrogen nuclei

$$x_{\text{H}} = x_{\text{H,tot}} - x_{\text{H}^+} - x_{\text{H}_2} \quad (2.2)$$

where $x_{\text{H,tot}}$ is the total abundance of hydrogen nuclei in all forms, and x_{C^+} and x_{Si^+} are the abundances of ionised carbon and silicon, respectively, which remain fixed throughout the simulations. These species undergo the reactions listed in Table 2.1. The radiative and chemical heating and cooling of the gas is modelled with a cooling

Table 2.2: Processes included in our thermal model.

Process	Reference
C ⁺ fine structure cooling	Glover & Mac Low (2007a)
O fine structure cooling	Glover et al. (2010)
Si ⁺ fine structure cooling	Glover & Mac Low (2007a)
H ₂ rovibrational lines	Glover & Abel (2008)
Gas-grain energy transfer	Hollenbach & McKee (1989)
Recombination on grains	Wolfire et al. (2003)
Atomic resonance lines	Sutherland & Dopita (1993)
H collisional ionisation	Abel et al. (1997)
H ₂ collisional dissociation	See Table 2.1
H ₂ formation on dust grains	Hollenbach & McKee (1989)
Cosmic ray ionisation	Goldsmith & Langer (1978)

function that contains contributions from the processes listed in Table 2.2.

To test our modified version of the FLASH code, we performed static and turbulent simulations using both our new FLASH implementation and our existing ZEUS-MP implementation (Glover & Mac Low 2007a,b) of the same physics, and verified that the codes produced comparable results.

2.2.2 Turbulent driving and hydrodynamics

We have applied our chemistry model to simulations of forced supersonic turbulence driven by fully solenoidal (divergence-free or rotational) and fully compressive (curl-free or dilatational) forcing (Federrath et al. 2008b, 2009, 2010), as two limiting cases to investigate the influence of the nature of the driving on the formation of H₂. These simulations use the piecewise parabolic method (PPM) (Colella & Woodward 1984) implementation of the FLASH code to integrate the equations of hydrodynamics on 3D periodic uniform grids with 256³ grid points.

As a control parameter in our simulations, we use the rms velocity of the turbulence. We use this in preference to the rms Mach number because the latter quantity depends on the sound speed of the gas, and in our non-isothermal simulations this is not constant, but varies in both space and time. To excite a turbulent flow with a specified

rms turbulent velocity, we include a forcing term \mathbf{f} in the gas momentum equation

$$\frac{\partial \mathbf{v}}{\partial t} + (\mathbf{v} \cdot \nabla) \mathbf{v} = -\frac{\nabla P}{\rho} + \mathbf{f}. \quad (2.3)$$

We model the random correlated stochastic forcing term \mathbf{f} such that it varies smoothly in space and time using the Ornstein-Uhlenbeck (OU) process. The OU process is a well-defined stochastic process with a finite autocorrelation timescale T . It describes the evolution of the forcing term \hat{f} in Fourier space (k -space) with the stochastic differential equation:

$$d\hat{f}(k, t) = f_0(k) \underline{\mathcal{P}}^\zeta(k) dW(t) - \hat{f}(k, t) \frac{dt}{T} \quad (2.4)$$

where $W(t)$ is a Wiener process, a random process that adds a Gaussian random increment to the vector field given in the previous time step dt , followed by the projection tensor $\underline{\mathcal{P}}^\zeta(k)$ in Fourier space. The projection operator reads

$$\mathcal{P}_{ij}^\zeta(k) = \zeta \mathcal{P}_{ij}^\perp(k) + (1 - \zeta) \mathcal{P}_{ij}^\parallel(k) = \zeta \delta_{ij} + (1 - 2\zeta) \frac{k_i k_j}{|k|^2}, \quad (2.5)$$

where δ_{ij} is the Kronecker symbol, and $\mathcal{P}_{ij}^\perp = \delta_{ij} - k_i k_j / k^2$ and $\mathcal{P}_{ij}^\parallel = k_i k_j / k^2$ are the fully solenoidal and the fully compressive projection operators, respectively (see e.g. Schmidt et al. 2009; Federrath et al. 2010).

By changing the value of the parameter ζ , we can determine the power of the compressive modes with respect to the total forcing power. For $\zeta = 1$ in the projection operator, we obtain a purely solenoidal force field, and with $\zeta = 0$, we obtain a purely compressive force field. Any combination of solenoidal and compressive modes can be constructed by choosing $\zeta \in [0, 1]$.

The large-scale stochastic forcing that we use, as the one closest to the observational data (Ossenkopf & Mac Low 2002; Brunt et al. 2009), models the kinetic energy input from large-scale turbulent fluctuations, breaking up into smaller structures. We thus drive the modes $k = [1, 3]$ in units of $\frac{2\pi}{L}$, where L is the box size. The forcing amplitude $A(k)$ has a parabolic dependence on k , such that most power is injected at $|\vec{k}| = 2$ and $A(1) = A(3) = 0$.

2.2.3 Initial conditions

Using the forcing module described above, and starting from zero velocities, we excite turbulent motions in a box with 256^3 grid points and of side length $L = 20$ pc, filled with

initially uniform atomic gas, using periodic boundary conditions. We perform purely hydrodynamical simulations, and neglect any complications introduced by magnetic fields or the effects of self-gravity. The abundances for carbon, oxygen and silicon were taken from Sembach et al. (2000) and are: $x_{\text{C}^+} = 1.41 \times 10^{-4}$, $x_{\text{O}} = 3.16 \times 10^{-4}$ and $x_{\text{Si}^+} = 1.5 \times 10^{-5}$. We assume that the dust-to-gas ratio has the standard solar value, and fix the dust temperature at 10 K in every run. We adopt a rate $\zeta_{\text{H}} = 10^{-17} \text{ s}^{-1}$ for the cosmic ray ionisation of atomic hydrogen (reaction 5 in Table 2.1). In the case of molecular hydrogen, we assume that all of the H₂⁺ ions produced in the reaction



are destroyed by dissociative recombination, yielding two hydrogen atoms, and so adopt a rate $\zeta_{\text{H}_2,6} = 2.22\zeta_{\text{H}}$ for reaction 6 that includes this contribution as well as that coming from direct dissociation of the H₂. For reaction 7, we adopt the rate $\zeta_{\text{H}_2,7} = 0.037\zeta_{\text{H}}$. In both cases, we assume that the ratio between the H₂ destruction rates and the ionisation rate of atomic hydrogen is the same as given in Woodall et al. (2007).

We perform two sets of simulations with different initial number densities: $n_0 = 30 \text{ cm}^{-3}$ and $n_0 = 300 \text{ cm}^{-3}$. For each initial density, we perform simulations with rms turbulent velocities of 0.4 km s⁻¹, 2 km s⁻¹ or 4 km s⁻¹, and examine both purely solenoidal and purely compressive forcing in each case, meaning that we perform a total of twelve simulations. We evolve each simulation for ten dynamical times $T = L/2v_{\text{rms}}$. For the first two dynamical times, the chemistry module is switched off, and the turbulence is allowed to reach a statistically steady state (Federrath et al. 2009, 2010; Price & Federrath 2010). After that, we consider the chemical evolution and follow the gas for a further eight dynamical times. Note also that in our later discussion of the time evolution of the H₂ fraction, we take the time at which we switch on the chemistry module to be $t = 0$, meaning that the simulations run from $t = -2T$ until $t = 8T$.

For simplicity, we set the ambient radiation field strength to zero in all of our simulations, thereby avoiding the necessity of modelling the penetration of Lyman-Werner band photons into the simulation volume, and allowing us to focus purely on the influence of the turbulent density enhancements on the overall H₂ formation rate. We note that the mean column density through our low n_0 simulations is approximately $20M_{\odot}\text{pc}^{-2}$, which is more than sufficient to adequately shield the H₂ in the gas against photodissociation (Krumholz et al. 2009), provided that the incident radiation field is close to the standard Galactic value. We have shown in other work (Glover & Mac Low 2011) that H₂ formation in clouds with surface densities of this value or higher is primarily limited by

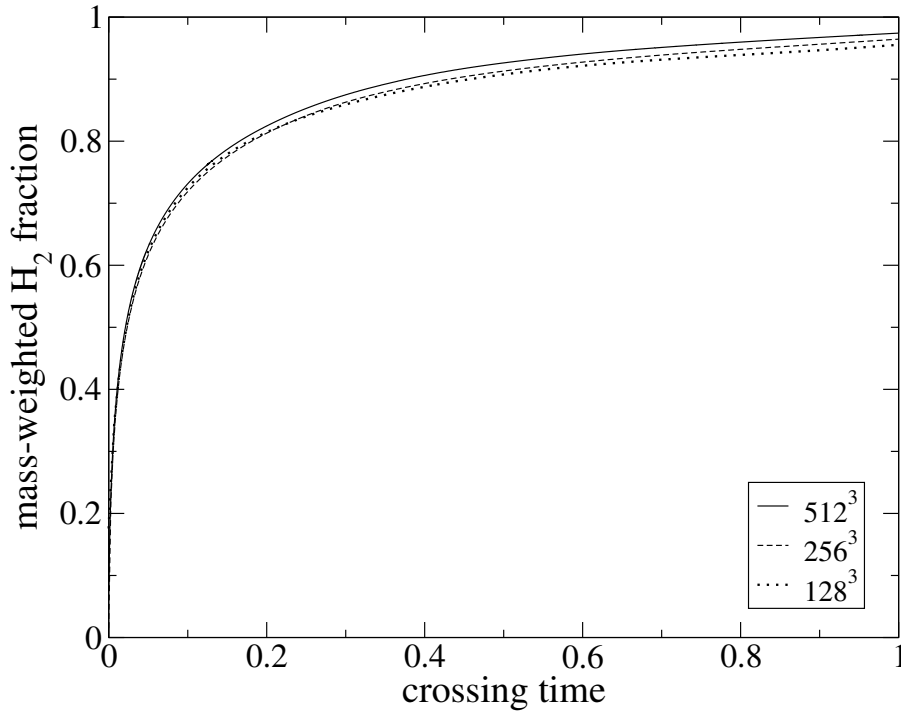


Figure 2.1: Time evolution of the mass-weighted H₂ abundance in units of the turbulent crossing time for $n_0 = 300 \text{ cm}^{-3}$ and $v_{\text{rms}} = 4 \text{ km s}^{-1}$ in simulations with numerical resolutions of 128^3 grid points (dotted), 256^3 grid points (dashed) and 512^3 grid points (solid).

the time required to form the H₂, rather than by the influence of UV photodissociation. We therefore would not expect this omission to have a large impact on our results. At late times, we will tend to under-predict the amount of atomic hydrogen in the gas, and to over-predict the amount of H₂, particularly in our low density runs, but previous work suggests that the effect will be small (Glover & Mac Low 2011). We note, however, that this approximation will break down for clouds immersed in UV radiation fields that are significantly stronger than the standard Galactic value (Glover, in preparation).

2.2.4 Numerical resolution

Glover & Mac Low (2007b) and Mac Low & Glover (2012) examined the sensitivity of the H₂ formation timescale in simulations of the turbulent ISM to the numerical resolution of the simulation, using numerical resolutions ranging from 64^3 to 512^3 zones. They found that there was some dependence on the numerical resolution of the simulation at early times, owing to the ability of the higher resolution to better

model the details of the highest density structures formed by the turbulence (see Federrath et al. 2010; Price & Federrath 2010), although it should be noted that in these simulations the turbulence was not driven to a statistical steady-state before the switch-on of the chemistry, which will tend to exacerbate any resolution dependence. These previous studies found that although there remain some signs of resolution-dependence at 256^3 zones, the difference between the 128^3 , 256^3 and 512^3 results is very small. However, these resolution tests were performed only for the case of solenoidal turbulence. Therefore, to test the sensitivity of H₂ formation to numerical resolution in the simulations with compressively driven turbulence, we have performed a resolution study for the run with $v_{\text{rms}} = 4 \text{ km s}^{-1}$ and $n_0 = 300 \text{ cm}^{-3}$. This is the run in which the highest densities are produced, and so if this is well-resolved, then it is reasonable to assume that our lower density and lower v_{rms} runs will also be well-resolved. In our resolution study, we performed simulations with resolutions of 128^3 , 256^3 , and 512^3 grid cells.

In Figure 2.1, we show how the mass-weighted mean abundance of H₂ (defined in section 3.1 below) evolves in runs with different resolution during the first crossing time. We see that there is almost no difference in the evolution of the H₂ abundance in the three simulations, and conclude that a numerical resolution of 256^3 grid cells should be enough to accurately model the growth of the H₂ fraction in our simulations.

2.3 Results

2.3.1 Time dependence of H₂ abundance

To quantify the rate at which H₂ forms in our simulation we compute the mass-weighted mean molecular fraction, $\langle x_{\text{H}_2} \rangle_{\text{M}}$, given by

$$\langle x_{\text{H}_2} \rangle_{\text{M}} = \frac{\sum_{i,j,k} \rho_{\text{H}_2}(i,j,k) \Delta V(i,j,k)}{M_{\text{H}}} \quad (2.7)$$

where we sum over all grid cells, and where $\rho_{\text{H}_2}(i,j,k)$ is the mass density of H₂ in computational cell (i,j,k) , $\Delta V(i,j,k)$ is the volume of the cell (i,j,k) , M_{H} is the total mass of hydrogen present in the simulation. In Figure 2.2, we plot the evolution of $\langle x_{\text{H}_2} \rangle_{\text{M}}$ as a function of time for both sets of runs, comparing different mean densities, rms velocities and types of driving. In Table 2.3, we give the time in Myr required for the mass-weighted mean molecular fraction to reach 50% ($t_{50\%}$) and 90% ($t_{90\%}$).

Looking at the evolution of H₂ fraction with time in Figure 2.2, we see that the time required to convert a large fraction of the initial atomic hydrogen to molecular hydrogen

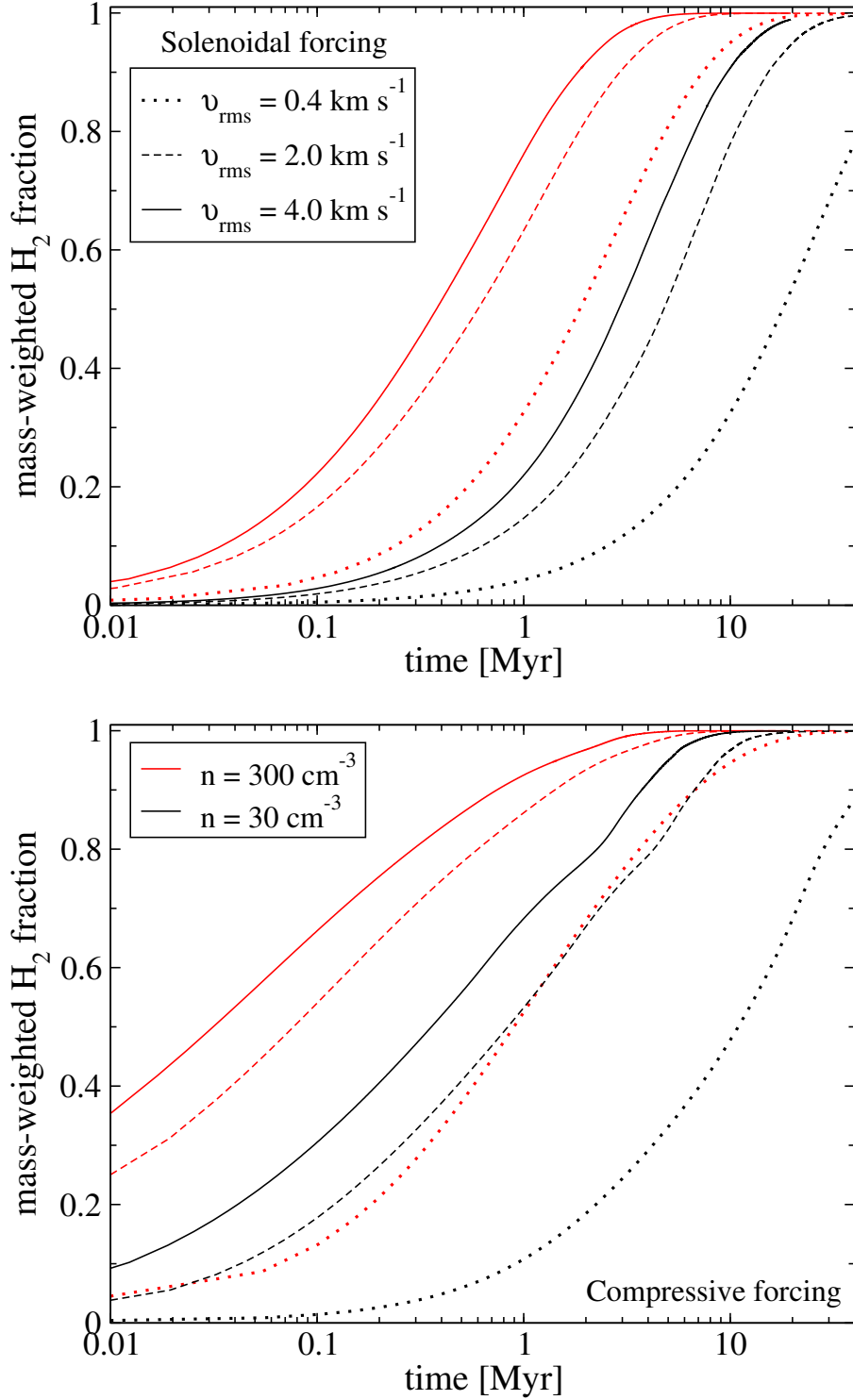


Figure 2.2: Evolution with time of the mass-weighted mean H₂ fraction $\langle x_{\text{H}_2} \rangle_{\text{M}}$ in runs with mean densities of 30 cm^{-3} (black) and 300 cm^{-3} (red). Three different values of the rms turbulent velocity v_{rms} are considered: 0.4 km s^{-1} (dotted), 2 km s^{-1} (dashed) and 4 km s^{-1} (solid). The upper panel shows the results for purely solenoidal forcing, while the lower panel shows the results for purely compressive forcing.

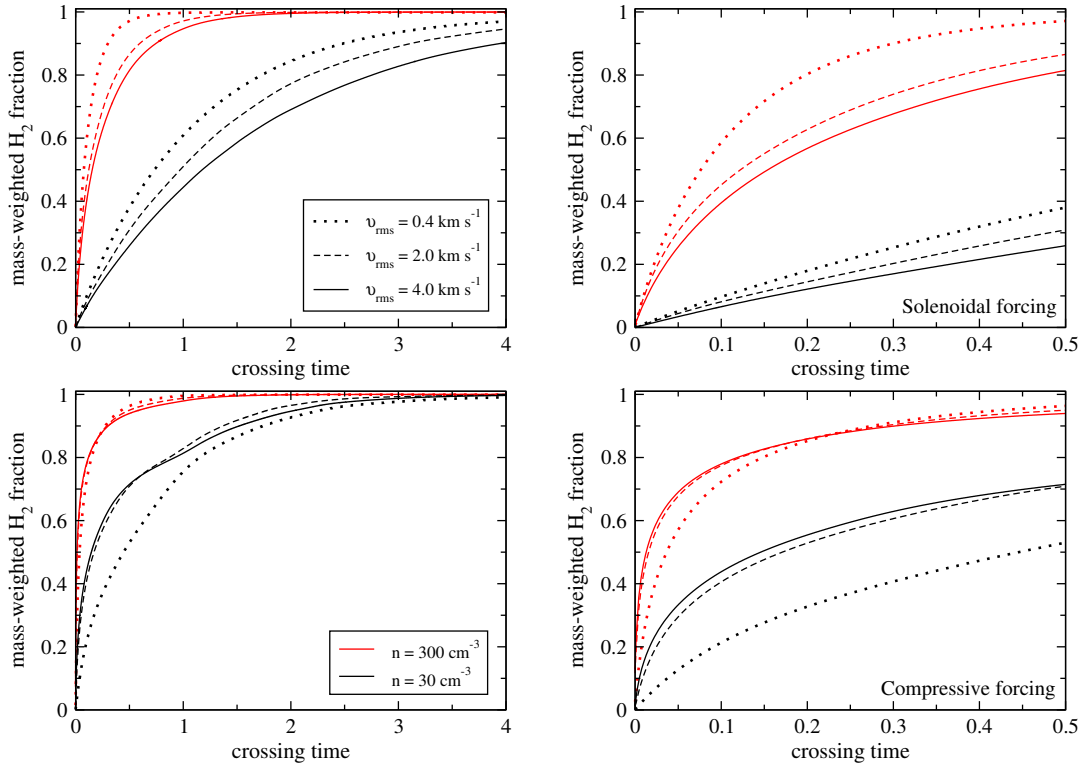


Figure 2.3: As Figure 2.2, but showing the evolution of $\langle x_{\text{H}_2} \rangle_{\text{M}}$ as a function of the turbulent crossing time T , rather than the absolute time. The left-hand panels show the evolution of $\langle x_{\text{H}_2} \rangle_{\text{M}}$ from $t = 0$ to $t = 4T$, while the right-hand panels zoom in on the period between $t = 0$ and $t = 0.5T$. As before, we plot results for three different values of the rms turbulent velocity – 0.4 km s^{-1} (dotted), 2 km s^{-1} (dashed) and 4 km s^{-1} (solid) – and two different mean densities – 30 cm^{-3} (black) and 300 cm^{-3} (red).

decreases as we increase the density or the strength of turbulent driving, in line with the previous findings of Glover & Mac Low (2007b). Comparing the two panels, we see that compressively-driven turbulence leads to more rapid formation of H₂ than turbulence driven by solenoidal forcing. The difference is particularly pronounced at early times, and in runs with high rms velocities: for instance, $t_{50\%}$ is roughly a factor of ten smaller in the compressive run with $v_{\text{rms}} = 4 \text{ km s}^{-1}$ and $n_0 = 300 \text{ cm}^{-3}$ than in the corresponding solenoidal run. At later times, the differences between the compressive and solenoidal runs become much smaller, with $t_{90\%}$ varying by less than a factor of three even in the most turbulent runs.

In Figure 2.3, we show the evolution of the mass-weighted mean H₂ abundance as a function of the turbulent crossing time. Here we see that most of the dependence on the rms velocities vanishes when the time is measured in units of the crossing time. Regardless of the strength of the turbulence or the nature of the forcing, the molecular

Table 2.3: Time in Myr when the gas becomes 50% and 90% molecular in all our runs.

Initial number density	$n_0 = 30 \text{ cm}^{-3}$		$n_0 = 300 \text{ cm}^{-3}$	
Solenoidal forcing	$t_{50\%}$	$t_{90\%}$	$t_{50\%}$	$t_{90\%}$
$v_{\text{rms}} = 0.4 \text{ km s}^{-1}$	17.94	60.97	1.91	7.36
$v_{\text{rms}} = 2.0 \text{ km s}^{-1}$	4.79	15.30	0.64	2.96
$v_{\text{rms}} = 4.0 \text{ km s}^{-1}$	2.88	9.67	0.38	1.83
Compressive forcing	$t_{50\%}$	$t_{90\%}$	$t_{50\%}$	$t_{90\%}$
$v_{\text{rms}} = 0.4 \text{ km s}^{-1}$	10.95	42.73	0.9	6.74
$v_{\text{rms}} = 2.0 \text{ km s}^{-1}$	0.87	6.74	0.11	1.44
$v_{\text{rms}} = 4.0 \text{ km s}^{-1}$	0.36	3.73	0.036	0.74

fraction reaches 50% within only 0.1 – 0.2 crossing times in the high density model. For the low density case it takes approximately 0.5 – 1.0 crossing times to form the same amount of molecular gas, regardless of v_{rms} .

Larger rms velocities yield more dense gas, resulting in a broader density PDF. On the other hand, they also lead to shorter turbulent crossing times, leaving less time for H_2 to form. As shown in Figure 2.3, these two effects largely compensate for each other. In the solenoidal case, the latter effect dominates, and the H_2 formation timescale, in units of the crossing time, decreases with decreasing v_{rms} . In runs with compressive forcing, on the other hand, the increased width of the density PDF with increasing v_{rms} is the dominant effect.

2.3.2 Density and temperature distributions

As Table 2.3 demonstrates, the H_2 formation time does not scale linearly with changes in the density of the gas. We find that an increase in density by a factor of ten causes the gas to become 90% molecular only 5 – 8 times faster in the solenoidal case and 4 – 6 times faster in the compressive case for the same rms turbulent velocities. The reason we see less dependence than one might naively expect is clear if we look at how the density distribution varies as we change the mean density n_0 . In Figure 2.4 we plot a volume-weighted number density PDF at $t = 0.5$ crossing times. As we decrease the density, the entire PDF moves to low densities. Most of the H_2 forms in dense gas, and so it is not surprising that reducing the amount of dense gas available has a significant effect on x_{H_2} . However, the densest gas quickly becomes fully molecular and thereafter does not contribute to the total H_2 formation rate (see Fig. 2.5), reducing the effect of density increase on the amount of formed H_2 . We therefore find a smaller difference between the H_2 formation rates in the solenoidal and compressive runs than one might

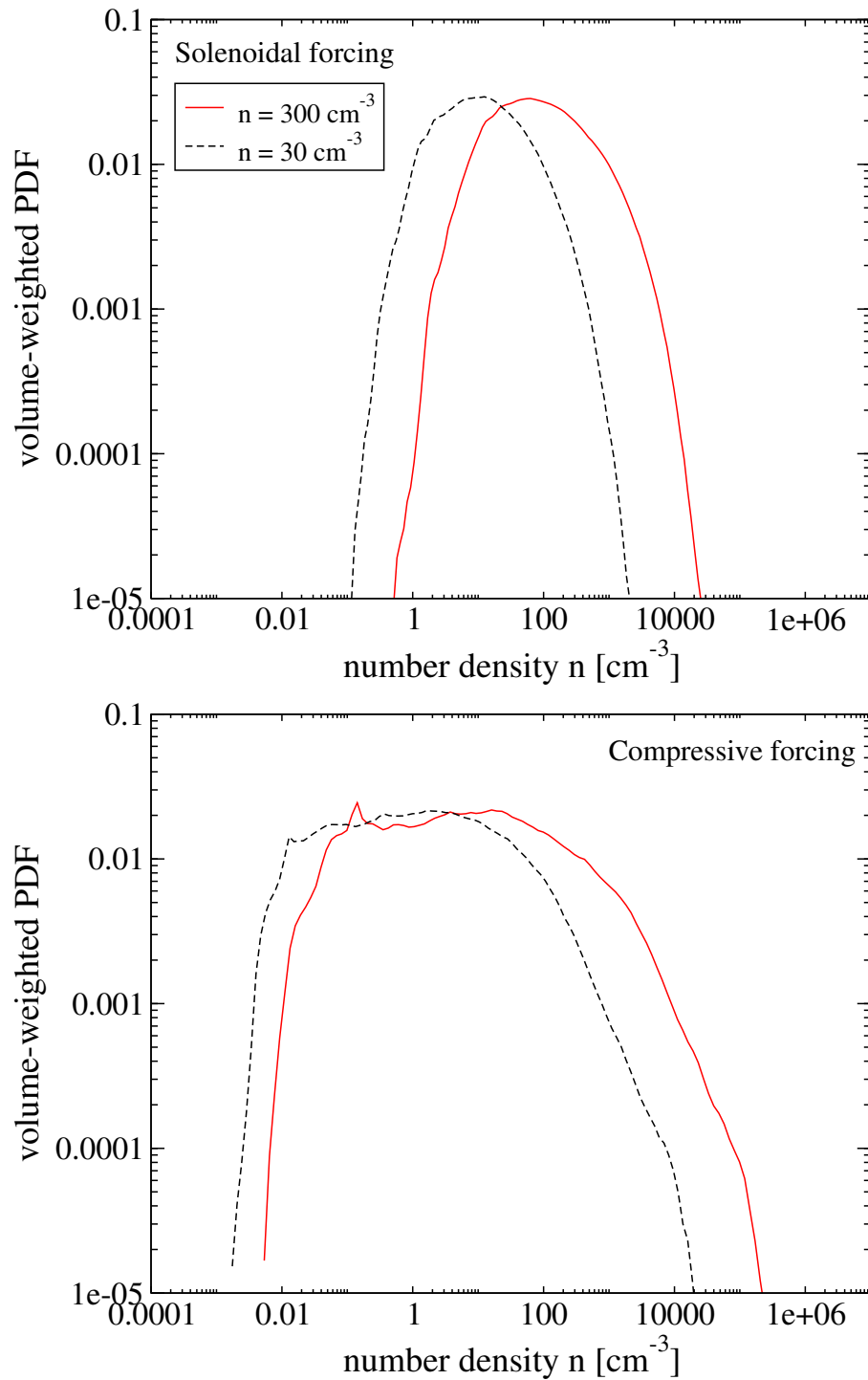


Figure 2.4: Volume-weighted density PDF for solenoidal (top) and compressive (bottom) forcing at time $t = 0.5$ crossing time in runs with $v_{\text{rms}} = 2 \text{ km s}^{-1}$. The red solid line presents the PDF in the run with mean density 300 cm^{-3} , while the black dashed line shows the PDF in the run with mean density 30 cm^{-3} .

expect given the significant difference in the density PDF.

In order to more quantitatively describe the H_2 distribution, we examine how the H_2 fraction varies with density. We compute x_{H_2} and n for each of the cells in the simulation volume and then bin the data by number density. We then compute the mean and standard deviation for x_{H_2} in each bin. The resulting values at $t = 0.5$ turbulent crossing times after the chemistry module is turned on are plotted in Figure 2.5. We clearly see a considerable scatter in the value of x_{H_2} at a given density. However, there is still an obvious underlying trend in the distribution of x_{H_2} with n , telling us that high density gas is more highly molecular, as expected (e.g. Hollenbach et al. 1971). At this point in the high density simulation the gas is almost fully molecular, whereas in the low density case $x_{\text{H}_2} \simeq 0.3$ for solenoidal and $x_{\text{H}_2} \simeq 0.7$ for compressive forcing (see Fig. 2.3). Despite this, however, there are regions where the H_2 fraction is already much higher, and we can see that gas with a number density $n > 10^3 \text{ cm}^{-3}$ is already almost entirely molecular in all of the simulations.

We also examine how the gas temperature varies as a function of number density in our simulations. Just as with the H_2 fraction above, we use the temperature output from our runs, bin it by number density n , and then compute the mean temperature and the standard deviation in the mean for each bin. We plot the resulting values again at $t = 0.5$ turbulent crossing time in Figure 2.6. Strong shocks present in the turbulent simulations lead to high post-shock temperatures that can reach several thousand Kelvin. In low density gas, these shocks cause a significant scatter in the temperatures. In high density gas, their effect is less pronounced, owing to the significantly shorter cooling time. In the case of compressive forcing, the gas is found to have a wider range of densities than the gas in the case of solenoidal forcing. As discussed before, this is a result of the stronger compressions produced by the turbulent forcing.

A final notable feature in the temperature distributions is the fact that in the low density solenoidal run, the temperature of the gas at $\log n \geq 3.5$ is clearly higher than in the other runs. This occurs because in this run, there is still a significant quantity of atomic hydrogen present at these densities (see Fig. 2.5), allowing heating due to H_2 formation to contribute significantly to the thermal balance of the gas. In the other runs, the atomic hydrogen fraction at these densities is very much smaller, and H_2 formation heating does not play a significant role in determining the gas temperature.

2.3.3 Dependence on the density clumping factor

As we are using periodic boundary conditions in our simulations, which prevent any of the H_2 molecules that form from escaping from the simulation volume, it is relatively

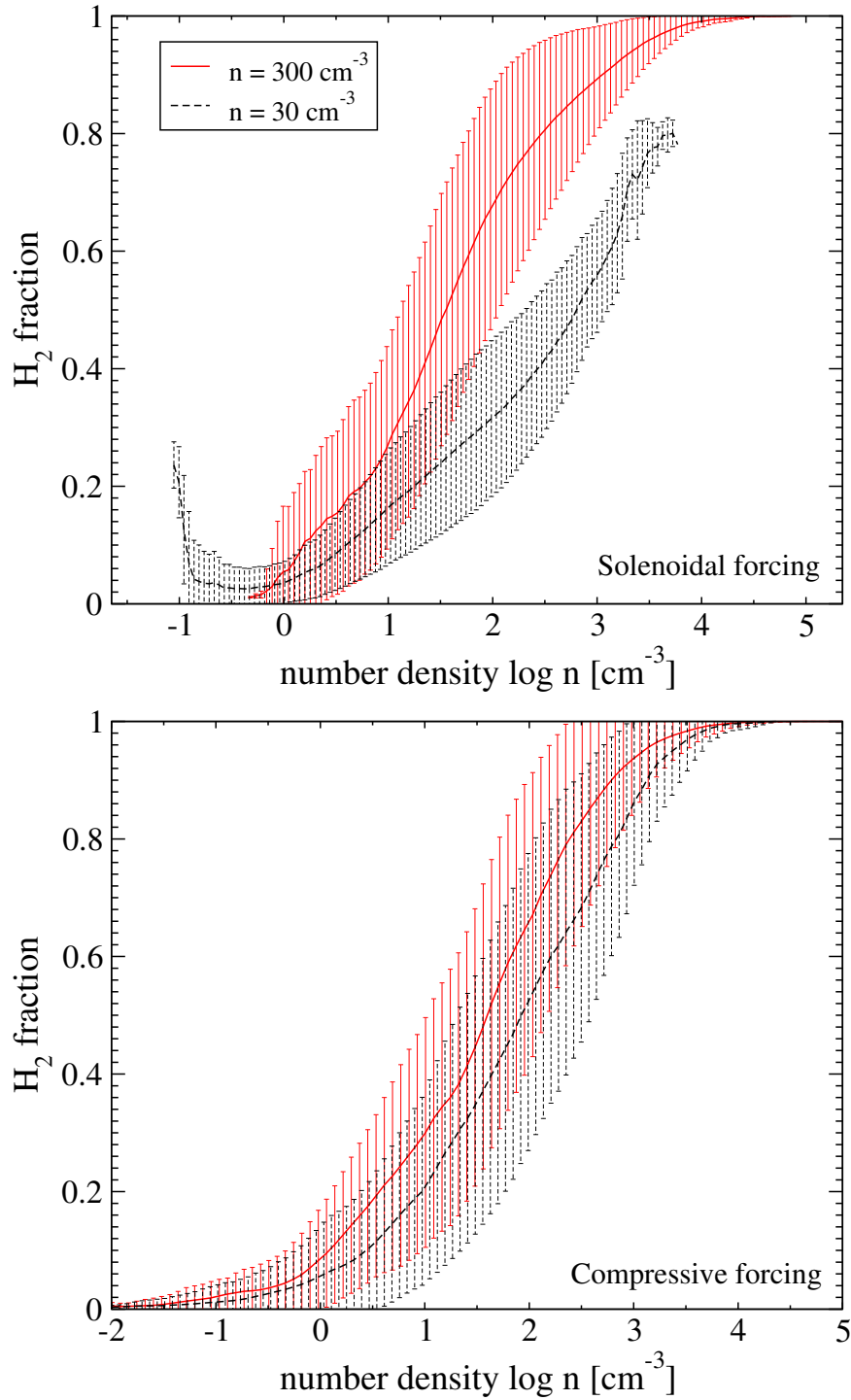


Figure 2.5: Mean H₂ fraction, plotted as a function of the number density n of the gas at time $t = 0.5$ crossing time in runs with $v_{\text{rms}} = 2 \text{ km s}^{-1}$ that use solenoidal (top) and compressive (bottom) forcing. The red solid line indicates the runs with mean density $n_0 = 300 \text{ cm}^{-3}$, and the black dashed line indicates the runs with mean density $n_0 = 30 \text{ cm}^{-3}$. To compute these values, we binned the data by number density and computed the mean value of x_{H_2} for each bin. The standard deviation in the value of x_{H_2} in each bin is indicated by the error bars.

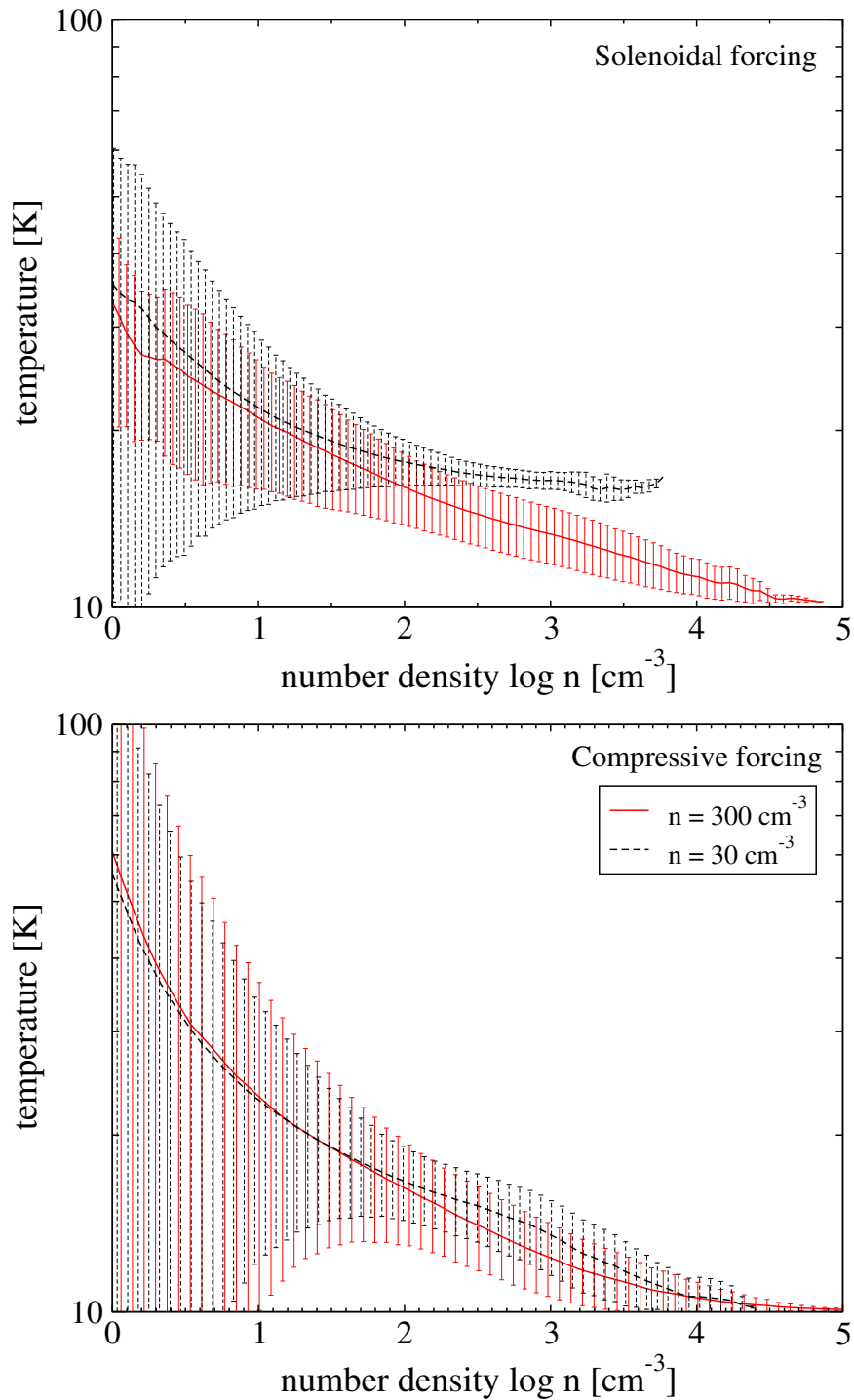


Figure 2.6: Mean gas temperature plotted as a function of the number density n at time $t = 0.5$ crossing time in runs with $v_{\text{rms}} = 2 \text{ km s}^{-1}$ using solenoidal (top) and compressive (bottom) forcing. The red solid line indicates the run with mean density of 300 cm^{-3} and the black dashed line indicates the run with mean density of 30 cm^{-3} . The data were binned in a similar fashion as for Figure 2.5. The standard deviation in the mean value in each bin is also indicated.

straightforward to show that the evolution of the mass-weighted mean H₂ abundance with time is described by the following equation

$$\frac{d\langle x_{\text{H}_2} \rangle_{\text{M}}}{dt} = \langle 2R_{\text{H}_2}(T, T_{\text{d}})x_{\text{H}}n - D_{\text{H}_2}x_{\text{H}_2}n \rangle_{\text{M}}, \quad (2.8)$$

where $R_{\text{H}_2}(T, T_{\text{d}})$ is the rate coefficient for H₂ formation on dust grains (reaction 1), and D_{H_2} is a destruction term depending on both temperature and density that accounts for the loss of H₂ in reactions 3, 4, 6 and 7 in Table 2.1. In practice, the impact of this destruction term is very small, unless $x_{\text{H}} \ll x_{\text{H}_2}$, and so to a good approximation

$$\frac{d\langle x_{\text{H}_2} \rangle_{\text{M}}}{dt} \simeq \langle 2R_{\text{H}_2}(T, T_{\text{d}})x_{\text{H}}n \rangle_{\text{M}}. \quad (2.9)$$

As it stands, Eq. 2.9 is not particularly useful, as in order to solve for the time dependence of $\langle x_{\text{H}_2} \rangle_{\text{M}}$, we need to know how R_{H_2} , x_{H} , and n are correlated, and how this correlation evolves with time. However, we can convert Equation 2.9 to a more useful form if we make a few further approximations. First, when the fractional ionisation of the gas is small, as it is throughout our simulations, we have $x_{\text{H}} \simeq 1 - x_{\text{H}_2}$, and hence

$$\frac{d\langle x_{\text{H}_2} \rangle_{\text{M}}}{dt} \simeq \langle 2R_{\text{H}_2}(T, T_{\text{d}})(1 - x_{\text{H}_2})n \rangle_{\text{M}}. \quad (2.10)$$

Second, in our simulations we keep the dust temperature fixed, and we know that most of the gas has a temperature that lies within the fairly narrow range of 10 – 40 K (see Fig. 2.6). As the dependence of $R_{\text{H}_2}(T, T_{\text{d}})$ on T is weak when the temperature is low, we do not introduce a large error by treating the gas temperature (and hence R_{H_2}) as if it were uncorrelated with the density, allowing us to write Equation 2.10 as

$$\frac{d\langle x_{\text{H}_2} \rangle_{\text{M}}}{dt} \simeq 2R_{\text{H}_2}(\langle T \rangle_{\text{M}}, T_{\text{d}})\langle (1 - x_{\text{H}_2})n \rangle_{\text{M}}, \quad (2.11)$$

where $\langle T \rangle_{\text{M}}$ is the mass-weighted mean temperature.

To proceed further, it is necessary to make an additional assumption regarding the correlation between the H₂ fraction and the density. Given the presence of the turbulence, it is appealing to assume that this turbulence perfectly mixes the gas on a timescale much shorter than the chemical timescale. If we make this assumption, then we can treat x_{H_2} as being uncorrelated with density, allowing us to rewrite

Equation 2.11 as

$$\frac{d\langle x_{\text{H}_2} \rangle_{\text{M}}}{dt} = 2R_{\text{H}_2}(\langle T \rangle_{\text{M}}, T_{\text{d}})\langle (1 - x_{\text{H}_2}) \rangle_{\text{M}}\langle n \rangle_{\text{M}} \quad (2.12)$$

$$= 2R_{\text{H}_2}(\langle T \rangle_{\text{M}}, T_{\text{d}})(1 - \langle x_{\text{H}_2} \rangle_{\text{M}})C_n\langle n \rangle_{\text{V}}, \quad (2.13)$$

where $\langle n \rangle_{\text{V}}$ is the volume-weighted mean of n , defined as

$$\langle n \rangle_{\text{V}} \equiv \frac{1}{V} \int_{\text{V}} n dV. \quad (2.14)$$

This quantity is related to the mass-weighted mean of n by

$$\langle n \rangle_{\text{M}} = \frac{1}{M} \int_{\text{V}} \rho n dV, \quad (2.15)$$

$$= \frac{1.4m_{\text{H}}}{M} \int_{\text{V}} n^2 dV, \quad (2.16)$$

$$= \frac{1.4m_{\text{H}}}{1.4m_{\text{H}}\langle n \rangle_{\text{V}}V} \langle n^2 \rangle_{\text{V}}, \quad (2.17)$$

$$= C_n \langle n \rangle_{\text{V}}, \quad (2.18)$$

where $C_n \equiv \langle n^2 \rangle_{\text{V}} / \langle n \rangle_{\text{V}}^2$ is the density clumping factor, and where we have used the fact that $\rho = 1.4m_{\text{H}}n$, and hence that $M \equiv \langle \rho \rangle_{\text{V}}V = 1.4m_{\text{H}}\langle n \rangle_{\text{V}}V$.

Equation 2.13 demonstrates that if our assumption of rapid mixing of the H_2 were true, then the evolution of the mass-weighted mean H_2 fraction in a gas cloud would be related in a very simple fashion to the mean density of the cloud and its density clumping factor. This fact has been used by Gnedin et al. (2009) as the basis of a simple sub-grid scale model of H_2 formation for cosmological simulations, or for other large-scale simulations without sufficient resolution to model the small-scale structure within molecular clouds. They write the formation rate of H_2 in a similar form to Eq. 2.13, and argue that $C_n \sim 3\text{--}10$ in typical turbulent clouds. Gnedin & Kravtsov (2011) further developed this idea, and showed that this sub-grid model does a good job of reproducing the dependence of the average atomic and molecular gas surface densities on the total hydrogen surface density that is observed in nearby spiral galaxies (Wong & Blitz 2002), and the dependence of the mean H_2 fraction on the total hydrogen column density observed in our own Galaxy (Gillmon et al. 2006; Wolfire et al. 2008).

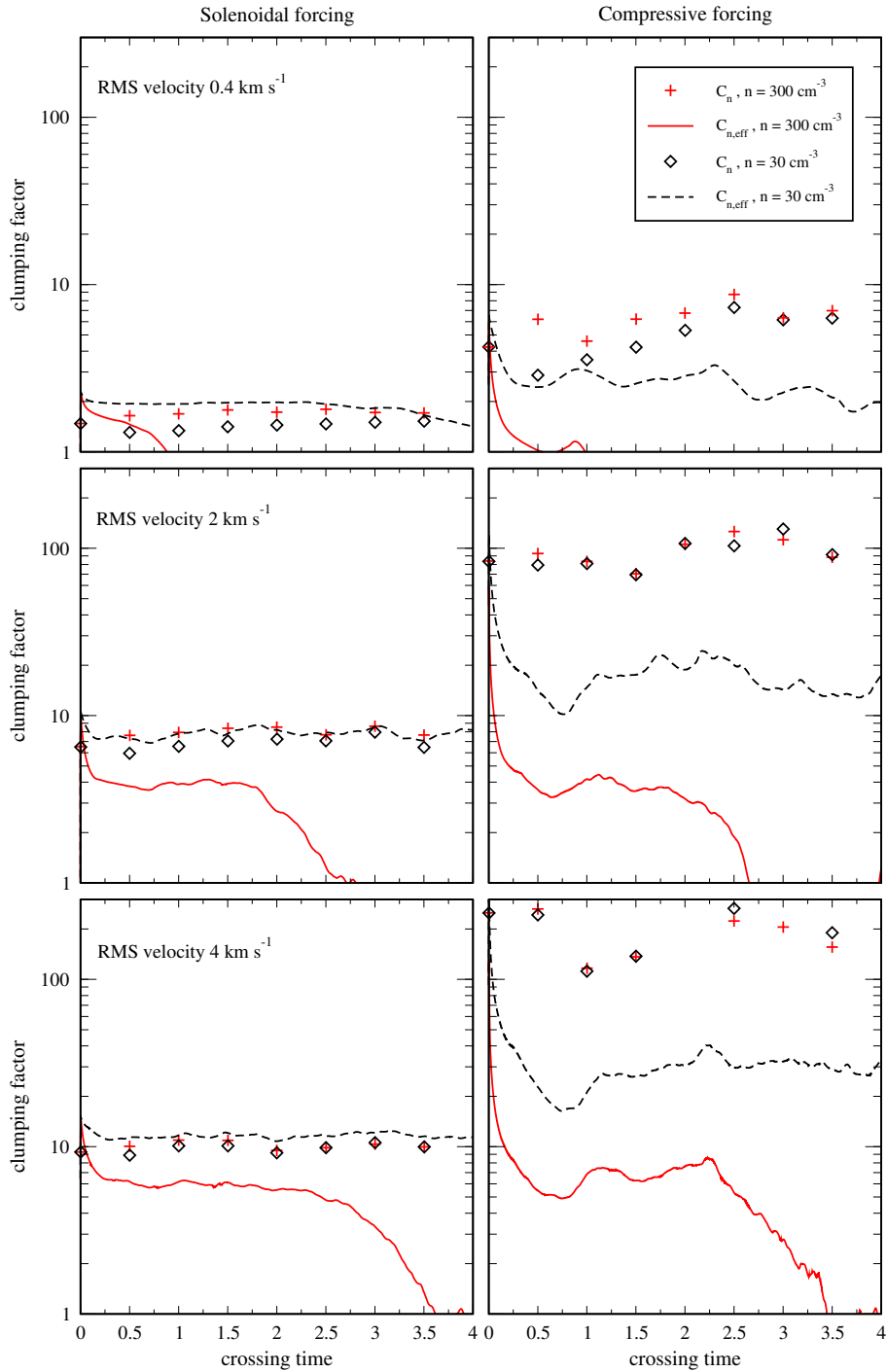


Figure 2.7: Evolution of the effective clumping factor $C_{n,\text{eff}}$ (lines) and the true clumping factor C_n (symbols) as a function of the turbulent crossing time T in runs with mean densities of 30 cm^{-3} (black) and 300 cm^{-3} (red). We plot results for three different values of the rms turbulent velocity: 0.4 km s^{-1} (top), 2 km s^{-1} (middle) and 4 km s^{-1} (bottom). The left-hand panels show the results for purely solenoidal forcing, while the right-hand panels show the results for purely compressive forcing.

However, the fact that we see a clear correlation between x_{H_2} and n in our simulations (see Fig. 2.5) implies that the assumption of rapid mixing that we used to derive Equation 2.13 is incorrect. In reality, it takes roughly one-third of a turbulent crossing time to fully mix material from overdense clumps into their lower density surroundings for solenoidal turbulence (Federrath et al. 2008a), and potentially longer than this for compressive turbulence. Therefore, a prescription such as that in Eq. 2.13 will overestimate the H_2 formation rate.

Our present simulations of solenoidal and compressive turbulence provide a useful test-bed for quantifying the extent to which Eq. 2.13, and by extension the Gnedin et al. sub-grid model, overestimates the H_2 formation rate. To do this, we define an ‘effective’ density clumping factor

$$C_{n,\text{eff}} = \frac{d\langle x_{\text{H}_2} \rangle_{\text{M}}/dt}{2R_{\text{H}_2}(\langle T \rangle_{\text{M}}, T_{\text{d}})(1 - \langle x_{\text{H}_2} \rangle_{\text{M}})\langle n \rangle_{\text{V}}}, \quad (2.19)$$

and compute how it evolves with time in each of our simulations, using our results for $\langle x_{\text{H}_2} \rangle_{\text{M}}$ and $\langle T \rangle_{\text{M}}$ discussed earlier. We then compare this with the true density clumping factor C_n computed at a number of different times during the simulations. The results of this comparison are plotted in Figure 2.7 (which shows the evolution between 0 and 4 crossing times) and Figure 2.8 (which shows an expanded view of the first 0.5 crossing times).

We see that at the very earliest times in the runs, there is a reasonable level of agreement between our inferred effective clumping factor $C_{n,\text{eff}}$ and the measured clumping factor C_n . Our computed values of $C_{n,\text{eff}}$ are typically some 20–40% larger than C_n , but an error of this magnitude is plausibly explained by our use of the mass-weighted mean temperature in our calculation of R_{H_2} : in reality, the dense gas, whose contribution initially dominates the H_2 formation rate, will generally be colder than this mean temperature.

However, this initial level of agreement between $C_{n,\text{eff}}$ and C_n is very quickly lost in most of the runs. In all of the simulations, the true clumping factor C_n remains approximately constant, varying by at most a factor of two in the compressive case, and by much less than this in the solenoidal case. On the other hand, in most of the runs, $C_{n,\text{eff}}$ decreases rapidly with time; only in the low density solenoidal model it does remain approximately constant during the lifetime of the simulation. The strong and almost immediate decrease of the effective clumping factor visible in Figures 2.7 and 2.8 is caused by the increase in the H_2 abundance in the dense gas. As the dense regions that initially dominate the H_2 formation rate become almost fully molecular, their contribution decreases rapidly, causing a significant fall in the mean H_2 formation

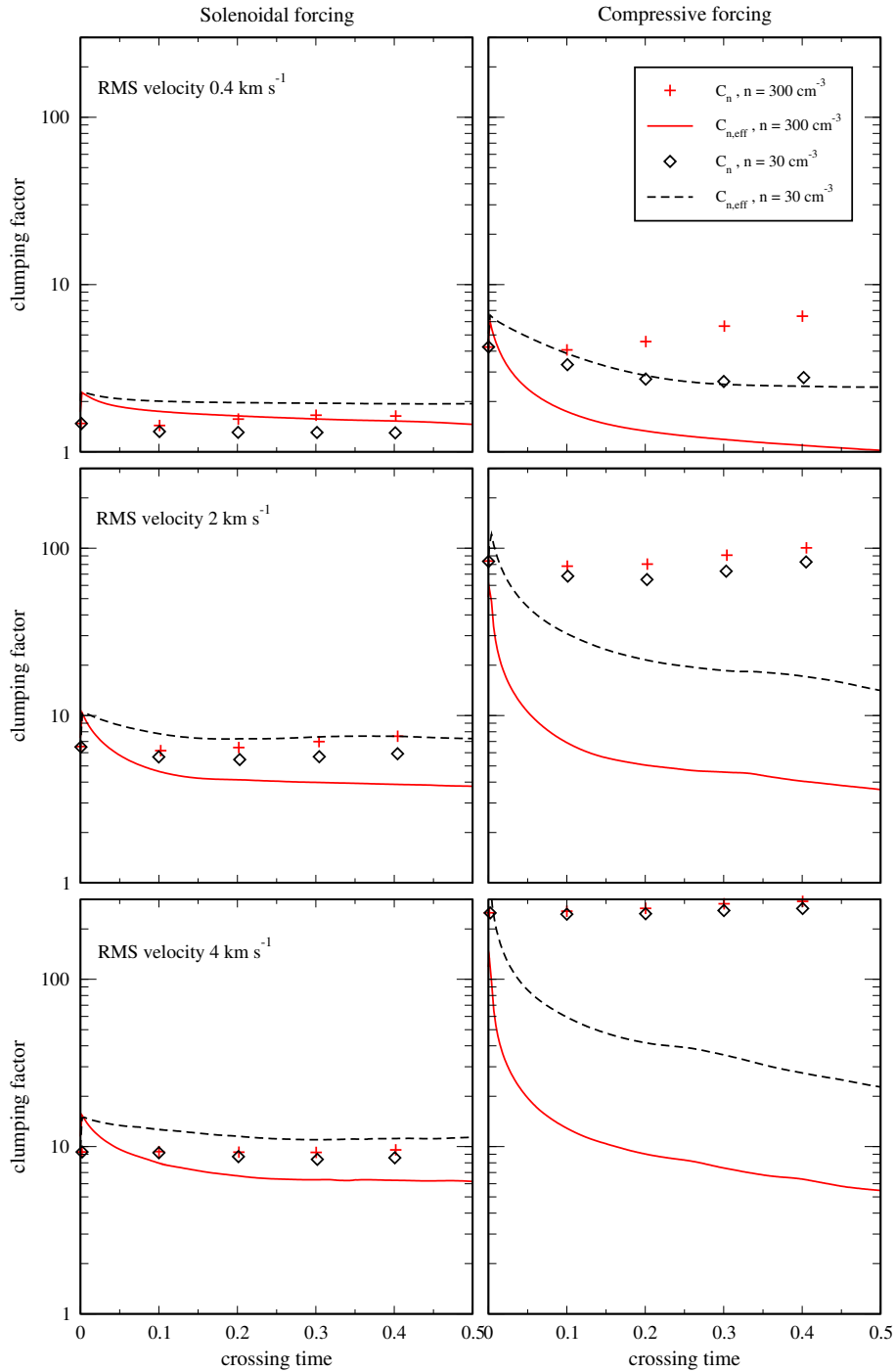


Figure 2.8: As Figure 2.7, but showing an expanded view of the first 0.5 crossing times. As before, three different values of the rms turbulent velocity v_{rms} are considered: 0.4 km s⁻¹ (top), 2 km s⁻¹ (middle) and 4 km s⁻¹ (bottom) - and two different mean densities - 30 cm⁻³ (black) and 300 cm⁻³ (red). The left-hand panels show the results for purely solenoidal forcing, while the right-hand panels show the results for purely compressive forcing.

rate within the simulation, and hence a significant decrease in $C_{n,\text{eff}}$. This effect is particularly pronounced in the compressively-forced runs, owing to their broad density PDFs. If we closely compare the results plotted in Figure 2.8 with the time evolution of the H_2 fraction shown in Figure 2.3, we can see that the Gnedin et al. (2009) approach starts to break down when the gas is about 30% molecular. In the high density solenoidal runs, the H_2 formation rate is almost immediately overestimated by a factor of 2, while in the compressive runs, the rate is overestimated by a factor of 4 in the low density case, and by a factor of 10 in the high density case.

It is clear from this analysis that in most cases there is no simple way to relate the mean number density of the gas and the current mass-weighted mean H_2 abundance to the current H_2 formation rate, given the strong time variation that we see in $C_{n,\text{eff}}$. This time variation is absent only when the characteristic H_2 formation timescale is longer than a turbulent crossing time, as is the case in our low-density solenoidal runs, as only in this case is our assumption of rapid turbulent mixing justified. One must therefore be careful when using the Gnedin et al. (2009) sub-grid model to describe the H_2 formation rate in numerical simulations.

2.4 Summary

We have presented the results of a study of H_2 formation in the turbulent ISM that examines the influence of the amplitude and mode of both solenoidal and compressive turbulent driving. We have performed high-resolution 3D hydrodynamic simulations using the massively parallel code FLASH, which we have modified to include a detailed treatment of atomic/molecular cooling and the most important hydrogen chemistry. Even though the chemical network we use is significantly simplified compared to the most detailed models available, it performs with acceptable accuracy for our purposes. We have performed simulations with numerical resolutions of 128^3 , 256^3 and 512^3 zones, and have demonstrated that our results are well-converged in our 256^3 runs. Our results also serve as a proof-of-concept application for our implementation of our non-equilibrium chemical model within the FLASH adaptive mesh refinement code.

We find that with both compressively and solenoidally driven turbulence, molecular hydrogen forms faster in gas with a higher mean density, or an environment with stronger turbulence. Although initially (during the first million years), H_2 formation is significantly faster with compressive turbulence than with solenoidal turbulence, at later times the differences become smaller, with the time taken to reach a molecular hydrogen fraction of 90% varying by at most a factor of three between the compressive and solenoidal runs. In almost all of our simulations, the gas becomes highly molecular

within a much shorter time than the 10–20 Myr that would plausibly be required to assemble the cloud from the diffuse ISM (Ballesteros-Paredes et al. 1999a; Elmegreen 2000; Hartmann et al. 2001).

We have also shown that when time is measured in the units of turbulent crossing time, the H₂ formation timescale becomes much less dependent on the strength of the turbulence. Increasing the strength of the turbulence produces more dense gas and reduces the time taken to form H₂. However, it also reduces the turbulent crossing time of the gas. In the solenoidal case, the reduction in the turbulent crossing time is the dominant effect, and so H₂ formation takes *longer* (in units of the crossing time) as we increase v_{rms} . On the other hand, in the compressive case, the broadening of the density PDF is the dominant effect, and increasing v_{rms} leads to a moderate decrease in the H₂ formation timescale measured in units of the crossing time.

The differences we have found between the compressive and solenoidal runs can largely be understood by considering the differences in the density PDFs in Figure 2.4. Compressive forcing produces a much wider spread of densities than solenoidal forcing, and since the H₂ formation rate per unit volume scales almost linearly with density when x_{H_2} is small, this allows the compressive runs to form H₂ much more rapidly at early times. However, rapid H₂ formation in the dense gas leads to its conversion to fully molecular form, at which point it no longer contributes to the total H₂ formation rate. This phenomenon occurs in both the solenoidal and the compressive runs, but has a greater effect in the compressive runs owing to the faster initial H₂ formation rate in these runs.

Finally, we have also used the results of our study to show that the Gnedin et al. (2009) prescription for correcting for the influence of unresolved density fluctuations on the H₂ formation rate in large-scale Galactic or cosmological simulations must be used with caution. The Gnedin et al. (2009) prescription assumes rapid gas mixing, when in reality it takes about one-third of a turbulent crossing time to mix the material from overdense clumps into the low density regions in the case of solenoidal forcing, and possibly even longer in the case of compressively-driven turbulence (Federrath et al. 2008a). We have shown that the effective clumping factor calculated with the assumption of rapid mixing over-predicts the H₂ formation rate. In the case of high density and strong compressive forcing, the H₂ formation rate can be overestimated by more than an order of magnitude at all but the very earliest times. For applications where one simply wants to determine which regions of the ISM become H₂-dominated (i.e. more than 50% molecular) and how quickly this occurs, their approach remains reasonably accurate, since $C_{n,\text{eff}}$ shows little variation while $\langle x_{\text{H}_2} \rangle_{\text{M}}$ remains small. On the other hand, if one is interested in the final, equilibrium state of the gas (as in

e.g. Krumholz & Gnedin 2011), then this approach may be problematic, as it will systematically over-predict the H_2 formation rate in highly molecular regions, with the result that the H_2 abundance will reach equilibrium too rapidly.

3 Cloud formation in colliding flows: Influence of the choice of cooling function

In this chapter we study the influence of the choice of cooling function on the formation of molecular clouds in high-resolution three-dimensional simulations of converging flows. We directly compare the results obtained using the simple, parametrized cooling function introduced by Koyama & Inutsuka (2002) and used by a number of converging flow studies with the results of the detailed calculation of the non-equilibrium chemistry and thermal balance of the gas. We find that a number of the cloud properties, such as the mass and volume filling fractions of cold gas, are relatively insensitive to the choice of cooling function. On the other hand, the cloud morphology and the large-scale velocity distribution of the gas do strongly depend on the cooling function. We show that the differences that we see can largely be explained by differences in the way that Lyman- α cooling is treated in the two complementary approaches, and that a proper non-equilibrium treatment of the ionisation and recombination of the gas is necessary in order to model the high-temperature cooling correctly.

We also investigate the properties of the dense clumps formed within the cloud. In agreement with previous models, we find that the majority of these clumps are not self-gravitating, suggesting that some form of large-scale collapse of the cloud may be required in order to produce gravitationally unstable clumps and hence stars. Overall, the physical properties of the dense clumps are similar in both simulations, suggesting that they do not depend strongly on the choice of cooling function. However, we do find a systematic difference of around 10 K in the mean temperatures of the clumps produced by the two models.

3.1 – Prologue –

The goal of this study is to overcome the restrictions encountered by most previous models of molecular cloud formation due to the complexity of chemical reaction networks and its inclusion in hydrodynamical codes. We have introduced the reader with this problem in section 1.5.

Here we present our high-resolution 3D simulations of cloud formation in colliding flows, and directly compare the results obtained from a simplified cooling model with those that we obtain from a self-consistent treatment of the cooling and chemistry of the gas. Our main goal is to understand how the use of a more accurate thermal model affects the dynamics of the flow and the nature of the structures that form within it.

3.2 Numerical Model

3.2.1 The numerical code and setup

We consider the atomic phase of the interstellar medium (ISM), whose behaviour is governed by the equations

$$\frac{\partial \rho}{\partial t} + \nabla \cdot (\rho \mathbf{v}) = 0 \quad (3.1)$$

$$\frac{\partial(\rho \mathbf{v})}{\partial t} + \nabla \cdot (\rho \mathbf{v} \mathbf{v}) = -\nabla P + \frac{1}{4\pi} (\nabla \times \mathbf{B}) \times \mathbf{B}, \quad (3.2)$$

$$\frac{\partial E}{\partial t} + \nabla \cdot [(E + P)\mathbf{v}] = n\Gamma - n^2\Lambda(T), \quad (3.3)$$

$$\frac{\partial \mathbf{B}}{\partial t} = \nabla \times (\mathbf{v} \times \mathbf{B}), \quad (3.4)$$

where ρ is the gas density, \mathbf{v} is the fluid velocity, \mathbf{B} is the magnetic field strength, which also must satisfy the constraint $\nabla \cdot \mathbf{B} = 0$, $E = P/(\gamma - 1) + \rho|v|^2/2$ is the total energy per unit volume, P is the thermal pressure, and $\gamma = 5/3$ is the adiabatic index. In the energy equation, n is the number density of hydrogen nuclei, which is related to the mass density via $n = \rho/(1.4m_p)$, where m_p is the proton mass, $n\Gamma$

is the radiative heating rate per unit volume and $n^2\Lambda$ is the radiative cooling rate per unit volume. In writing down this set of equations, we have assumed that we can neglect the effects of the self-gravity of the gas. We make a similar assumption in the simulations presented in this chapter, and defer investigation of the more computationally demanding self-gravitating case to future work.

We model the collision of two large cylindrical streams of warm atomic gas using a modified version of the adaptive mesh refinement (AMR) code FLASH (Fryxell et al. 2000). Our modifications include the addition of a simplified but accurate treatment of the most important hydrogen chemistry, together with a detailed atomic and molecular cooling function. They are described in detail in Micic et al. (2012a).

We use a similar setup to that studied in Banerjee et al. (2009), which itself was based on model L256 Δv 0.17 from the study of Vázquez-Semadeni et al. (2007). The two cylindrical streams, each 112 pc long and 32 pc in radius, are given an initial, slightly supersonic inflow velocity so that they collide at the centre of the numerical box ($x = 0$ pc). The $(256 \text{ pc})^3$ simulation box is periodic, and the streams are completely contained within it, such that the resulting cloud occupies a relatively small volume far from the boundaries, and interacts freely with its diffuse environment, with relatively little effect from the boundaries. The box is initially filled with warm atomic gas with a uniform number density $n = 1 \text{ cm}^{-3}$. This corresponds to an initial mass density of $\rho = 2.12 \times 10^{-24} \text{ g cm}^{-3}$, if we adopt a 10:1 ratio of hydrogen to helium, by number. The initial temperature of the atomic gas is $\sim 5000\text{K}$, corresponding to an isothermal sound speed of 5.7 km s^{-1} . The initial velocity of each flow is 7 km s^{-1} , and so the flows have an initial isothermal Mach number of 1.22. At temperature of $T = 5000\text{K}$ for the warm phase, this implies that the cold phase comes into hydrostatic thermal pressure balance with the warm gas at a density of roughly 100 cm^{-3} (see e.g. Wolfire et al. 1995, 2003). Furthermore, we add 10% random velocity perturbations to the bulk stream. Finally, we note that we include a magnetic field, which we assume to be oriented parallel to the inflow. The initial magnetic field strength is taken to be $3 \mu\text{G}$, consistent with estimates of the mean Galactic magnetic field strength (Beck 2001). This corresponds to a critical mass-to-flux ratio (see Vázquez-Semadeni et al. 2011).

We follow the collision of the streams of gas with up to 11 AMR refinement levels corresponding to a maximum effective resolution of 8192^3 grid cells, or a grid spacing of $\Delta x = 0.03 \text{ pc}$ in each direction. We use a Jeans-type criterion (Truelove et al. 1997; Federrath et al. 2011) for the dynamical mesh refinement which requires that the local Jeans length is resolved with at least 10 grid cells while refinement is active. Although our simulations do not include the effects of self-gravity, our use of a Jeans-type criterion ensures that we resolve any significant temperature or density gradients

within the gas.

3.2.2 Cooling and heating

The simulations of Vázquez-Semadeni et al. (2007) and Banerjee et al. (2009) used a cooling function derived from the one-dimensional colliding flow models of Koyama & Inutsuka (2000). A simple analytical fit was provided by Koyama & Inutsuka (2002), and has the form¹:

$$\Gamma = 2.0 \times 10^{-26} \text{ erg s}^{-1}, \quad (3.5)$$

$$\frac{\Lambda(T)}{\Gamma} = 10^7 \exp\left(-\frac{1.184 \times 10^5}{T + 1000}\right) + 1.4 \times 10^{-2} \sqrt{T} \exp\left(-\frac{92}{T}\right) \text{ cm}^3. \quad (3.6)$$

where T is the gas temperature in Kelvin. With this cooling function, the simulated ISM is thermally unstable in the density range $1 \lesssim n \lesssim 10 \text{ cm}^{-3}$, corresponding to equilibrium temperatures in the range $500 \lesssim T \lesssim 5000 \text{ K}$.

This simplified treatment of the heating and cooling of the gas does not account for any chemical effects. It assumes that the photoelectric heating efficiency is constant, whereas in practice it is known to depend on the electron number density (see e.g. Bakes & Tielens 1994; Wolfire et al. 1995). It also assumes that Lyman- α cooling is extremely efficient: the high temperature cooling rate assumed in the Koyama & Inutsuka (2002) function corresponds to the cooling one would expect in a gas in which the electron and atomic hydrogen number densities are approximately equal. In our present study, we investigate how the results that we obtain when we properly account for these effects compare with the results produced by this more simplified treatment.

To do this, we perform two simulations using the setup described in Section 3.2.1. In one, we use the Koyama & Inutsuka (2002) cooling function, as in Banerjee et al. (2009). In the other, we use the time-dependent chemical model and cooling function described in Glover & Mac Low (2007a,b). This model follows the abundances of four chemical species – free electrons, H^+ , H , and H_2 – linked by the reactions listed in Table 3.1. It assumes that any carbon in the gas remains in the form of C^+ and that any oxygen remains in atomic form, and so underestimates the cooling rate in regions

¹Note that the version of this fit printed in Koyama & Inutsuka (2002) suffers from a significant typographical error, which has the effect of making the low-temperature cooling rate far too large. The version we quote here is the corrected version of their fit, as given in Vázquez-Semadeni et al. (2007).

Table 3.1: Reactions in our non-equilibrium chemical model.

No.	Reaction	Reference
1	$\text{H} + \text{H} + \text{grain} \rightarrow \text{H}_2 + \text{grain}$	1
2	$\text{H}_2 + \text{H} \rightarrow \text{H} + \text{H} + \text{H}$	2
3	$\text{H}_2 + \text{H}_2 \rightarrow \text{H} + \text{H} + \text{H}_2$	3
4	$\text{H}_2 + \text{e}^- \rightarrow \text{H} + \text{H} + \text{e}^-$	4
5	$\text{H} + \text{c.r.} \rightarrow \text{H}^+ + \text{e}^-$	See §3.2.2
6	$\text{H}_2 + \text{c.r.} \rightarrow \text{H} + \text{H}$	See §3.2.2
7	$\text{H}_2 + \text{c.r.} \rightarrow \text{H} + \text{H}^+ + \text{e}^-$	See §3.2.2
8	$\text{H} + \gamma_{\text{X}} \rightarrow \text{H}^+ + \text{e}^-$	5
9	$\text{H} + \text{e}^- \rightarrow \text{H}^+ + \text{e}^- + \text{e}^-$	6
10	$\text{H}^+ + \text{e}^- \rightarrow \text{H} + \gamma$	7
11	$\text{H}^+ + \text{e}^- + \text{grain} \rightarrow \text{H} + \text{grain}$	8

Notes: “c.r.” denotes a cosmic ray particle, and γ_{X} denotes an X-ray photon

References: 1: Hollenbach & McKee (1979), 2: Mac Low & Shull (1986), 3: Martin et al. (1998), 4: Trevisan & Tennyson (2002), 5: Wolfire et al. (1995), 6: Abel et al. (1997), 7: Ferland et al. (1992), 8: Weingartner & Draine (2001a)

dominated by CO. However, Glover & Clark (2012b) have shown that this does not have a strong effect on the dynamics of the gas on scales larger than those of individual pre-stellar cores, and so making this simplifying assumption should not greatly affect our results.

We use an implementation of the Glover & Mac Low model within FLASH that is described in detail in Micic et al. (2012a). Our approach uses FLASH’s standard tracer field implementation to directly follow the advection of the fractional abundances of molecular hydrogen (x_{H_2}) and ionised hydrogen (x_{H^+}). The abundances of the other two species – atomic hydrogen (x_{H}) and electrons (x_{e}) – are computed from the conservation laws for charge

$$x_{\text{e}} = x_{\text{H}^+} + x_{\text{C}^+} + x_{\text{Si}^+} \quad (3.7)$$

and for the total amount of hydrogen

$$x_{\text{H}} = x_{\text{H,tot}} - x_{\text{H}^+} - 2x_{\text{H}_2}. \quad (3.8)$$

Here, $x_{\text{H,tot}}$ is the total abundance of hydrogen nuclei in all forms, which we normalize to unity, and x_{C^+} and x_{Si^+} are the abundances of ionised carbon and silicon, respectively, which remain fixed throughout the simulations.

We assume that carbon, oxygen and silicon remain in the form of C^+ , O and Si^+

throughout the simulation, and adopt fractional abundances for these species given by $x_{\text{C}^+} = 1.41 \times 10^{-4}$, $x_{\text{O}} = 3.16 \times 10^{-4}$ and $x_{\text{Si}^+} = 1.5 \times 10^{-5}$, respectively (Sembach et al. 2000). The radiative and chemical heating and cooling of the gas is modelled with a cooling function that contains contributions from a range of processes, of which the most important are C^+ and O fine structure cooling, Lyman- α cooling, and photoelectric heating. Full details of these processes, along with the other contributions to our cooling function, can be found in Glover & Mac Low (2007a,b) and Micic et al. (2012a).

In our run with the Glover & Mac Low chemistry and cooling model, we adopt a value of $G_0 = 1.0$ for the strength of the interstellar radiation field in units of the Habing field (Habing 1968). We take the cosmic ray ionisation rate of atomic hydrogen to be $\zeta_{\text{H}} = 10^{-17} \text{ s}^{-1}$ and assume that the ratio of this rate to the cosmic ray ionisation rate of H_2 is the same as given in the UMIST astrochemistry database (Le Teuff et al. 2000). We include the effects of X-ray ionisation and heating using the prescription given in Appendix A of Wolfire et al. (1995), and assume a uniform absorbing column density of warm atomic hydrogen $N_{\text{w}} = 10^{19} \text{ cm}^{-2}$. In our present study, we do not include the effects of self-gravity, magnetic fields, dust shielding, or H_2 self-shielding. We note that although we expect dust shielding to have a significant effect on the thermal state of the gas regions with mean visual extinctions $\bar{A}_V > 1$, these account for only a small fraction of the simulation volume.

3.3 Results

3.3.1 Density and temperature distributions

The sequence of events that occurs within our two simulations is broadly similar in both cases, and is also in good agreement with the results of previous studies (see e.g. Vázquez-Semadeni et al. 2007; Banerjee et al. 2009). We therefore begin by briefly describing this sequence of events, before moving on to look at the differences that do occur between the two runs.

At the interface where our transonic, converging flows collide, the gas is shocked and moderately compressed. This compression destabilises the gas, triggering a thermal instability (TI) that causes the gas to cool rapidly. As the gas cools, it is compressed by the thermal pressure of the surrounding warm gas, leading to a rapid increase in its density. This process comes to an end once the gas reaches the equilibrium temperature of the cold neutral medium (CNM) phase, which for the conditions simulated here is below 100 K. The cool dense gas initially forms a sheet that then fragments into

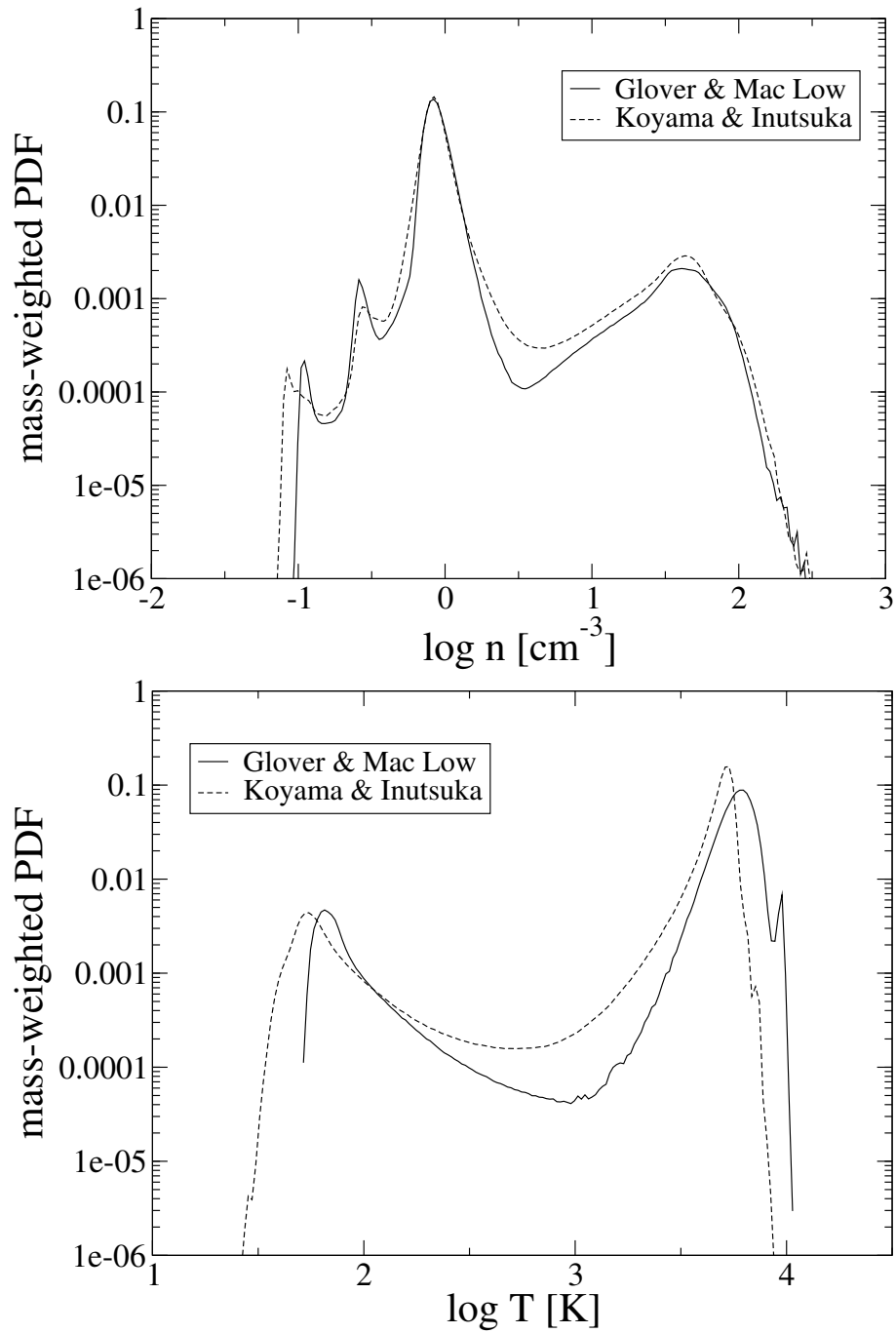


Figure 3.1: Mass-weighted density (top panel) and temperature (bottom panel) probability distribution function (PDF) at time $t = 22$ Myr. The solid line presents the PDF in the run with non-equilibrium chemical model, while the dashed line corresponds to the PDF in the run with Koyama & Inutsuka cooling function.

filaments and ultimately into small, pressure-confined clumps. As the thermal pressure of the dense gas is in close balance with the total (thermal plus ram) pressure of the warm neutral medium (WNM) outside it, the cold gas can easily reach number densities of the order of 100 cm^{-3} , comparable to the mean density of the gas in many GMCs (see e.g. Roman-Duval et al. 2010; Hughes et al. 2010).

The cloud of gas that forms in the interface region is composed of a mixture of diffuse and dense gas, including a significant fraction of material in the thermally unstable region intermediate between the CNM and WNM phases (see Figure 3.1). Rather than the classical picture of a two-phase medium, we find instead a continuous distribution of densities and temperatures, albeit one with clear peaks corresponding to the CNM and WNM regimes (see also Vázquez-Semadeni et al. 2000; Gazol et al. 2001, 2005; Audit & Hennebelle 2005).

In Figure 3.1 we plot mass-weighted density (top panel) and temperature (bottom panel) probability distribution functions (PDFs) for both models at a time $t = 22 \text{ Myr}$, several million years after the end of the inflow. It is clear from the Figure that these PDFs do not differ by much between the two runs. The main difference that is apparent is that the temperatures that we recover for the CNM and WNM phases (the two clear peaks in the temperature PDF) are slightly smaller in the simulation run using the Koyama & Inutsuka cooling function than in the simulation using the Glover & Mac Low treatment. This difference in behaviour is relatively simple to understand. At high temperatures ($T > 7000 \text{ K}$), the Koyama & Inutsuka cooling rate coefficient is given approximately by

$$\Lambda_{\text{KI}}(T) \simeq 2 \times 10^{-19} \exp\left(-\frac{1.184 \times 10^5}{T + 1000}\right). \quad (3.9)$$

The main coolant in the Glover & Mac Low treatment at these temperatures is Lyman- α cooling, for which they use the following expression from Cen (1992)

$$\Lambda_{\text{Ly-}\alpha} = \frac{7.5 \times 10^{-19}}{1 + \sqrt{T/10^5}} \exp\left(-\frac{118348}{T}\right) x_e x_{\text{H}}, \quad (3.10)$$

where $x_e \equiv n_e/n$ is the fractional abundance of electrons and $x_{\text{H}} \equiv n_{\text{H}}/n$ is the fractional abundance of atomic hydrogen. Comparing these two cooling rates, we find that they produce comparable amounts of cooling only when $x_e \simeq x_{\text{H}} \simeq 1/2$, i.e. only when the chemical state of the gas is such that we get roughly the maximum amount of Lyman- α cooling possible. In highly ionised gas with $n_e \gg n_{\text{H}}$, or predominantly neutral gas with $n_e \ll n_{\text{H}}$, the Lyman- α cooling rate is considerably smaller, and hence in these conditions, the Koyama & Inutsuka treatment significantly overestimates the

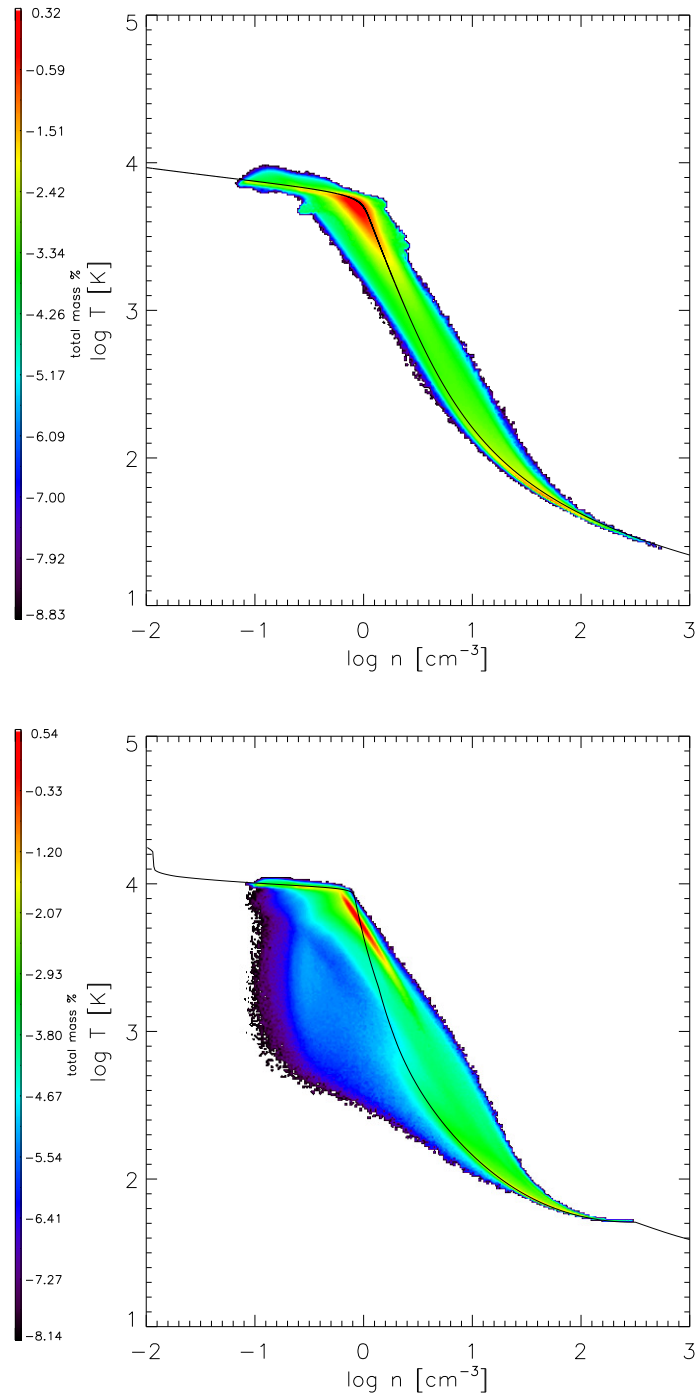


Figure 3.2: Two-dimensional PDFs of temperature and density for the two simulations, for a time $t = 22$ Myr. The top panel shows the results from the simulation that used the Koyama & Inutsuka cooling function, and the bottom panel shows the results from the simulation using the full non-equilibrium treatment. The fraction of mass in each region of the density-temperature space is indicated by the colour scale. The solid line shows the equilibrium temperature as a function of density, derived under the assumption that the gas is also in chemical equilibrium.

true cooling rate of the gas. The exponential temperature dependence of the cooling rate means that a large error in the value of the rate leads to only a small error in the gas temperature, but this is sufficient to explain the offset in the characteristic temperature of the WNM that we find when we compare our two simulations.

The difference in the CNM temperatures is not caused by a difference in the low temperature cooling rates, but rather by a difference in the radiative heating rate. In the Koyama & Inutsuka treatment, the heating rate throughout the gas is simply $\Gamma = 2 \times 10^{-26} \text{ erg s}^{-1}$. In the Glover & Mac Low treatment, on the other hand, the heating rate is sensitive to the chemical composition of the gas owing to the fact that the photoelectric heating efficiency is a function of the electron density (Bakes & Tielens 1994; Weingartner & Draine 2001b). In cold, dense gas, photoelectric heating is relatively efficient, and the heating rate is given approximately by $\Gamma_{\text{pe}} \simeq 5 \times 10^{-26} \text{ ergs}^{-1}$, i.e. it is roughly 2.5 times larger than assumed in the Koyama & Inutsuka treatment. It is therefore not surprising that the gas can cool to somewhat lower temperatures in this case.

In order to investigate the dependence of temperature on density in our two simulations, we plot in Figure 3.2 the two-dimensional (2D) PDFs of these quantities. The results for the Koyama & Inutsuka run are shown in the upper panel, while the results of the non-equilibrium run are shown in the lower panel. The equilibrium temperature of the gas is indicated using the solid line. In the case of the simulation using the non-equilibrium treatment of chemistry and cooling, we derived an equilibrium temperature at each density by assuming that the gas was also in chemical equilibrium. We see from Figure 3.2 that in the simulation with the Koyama & Inutsuka cooling function, most of the gas has a temperature close to the equilibrium value. In the simulation with the Glover & Mac Low chemistry and cooling, on the other hand, the departures from equilibrium are more pronounced. The gas is close to the equilibrium temperature at densities $n < 1 \text{ cm}^{-3}$ and $n > 30 \text{ cm}^{-3}$, but the equilibrium temperature curve does not give a good description of the distribution of gas temperatures at intermediate densities. In this intermediate regime, the temperature falls off less rapidly with increasing density than predicted by the equilibrium temperature curve. This is a consequence of the sensitivity of the photoelectric heating rate to the electron number density, n_e . As n_e increases, the net positive charge of the dust grain population decreases, or even becomes negative. This makes it easier for incoming photons to cause the ejection of photoelectrons. Consequently, the photoelectric heating efficiency tends to increase with increasing electron number density, up to a limiting value of a few percent (Bakes & Tielens 1994; Wolfire et al. 1995; Weingartner & Draine 2001b). In the density and temperature regime where we see the greatest deviations from the equilibrium temperature curve, the photoelectric heating efficiency has not yet reached

this limiting value, and hence any difference between the actual electron number density and the equilibrium value leads to a photoelectric heating rate that also differs from the value that it would have in equilibrium. As the recombination timescale in this gas is relatively long, of the order of a few Myr or more, the gas is generally slightly more ionised than it would be in equilibrium, and hence is heated slightly more efficiently.

Finally, as we know that stars form in cold gas, it is interesting to examine how the cold gas fraction differs in our two simulations. As we have already seen, the cold and warm phases in our simulations are not completely distinct, and a significant fraction of the mass of the cloud lies intermediate between these two phases. The definition of "cold" gas is therefore somewhat subjective. Here, we define cold gas to be gas with a temperature $T < 300$ K. (We note from Figure 3.2 that in both simulations, the majority of the gas with a temperature as low as this has a density $n > 10 \text{ cm}^{-3}$). In Figure 3.3, we plot how the mass fraction (top panel) and volume fraction (bottom panel) of the cold gas evolves with time in both simulations.

Prior to the end of the inflow, at $t \sim 16$ Myr, both simulations show extremely similar behaviour. The amount of cold gas is small – it accounts for only 5% of the total mass and only a tiny fraction of the total volume of the simulation – and the cold gas fraction increases only slowly with time. After the end of the inflow, however, greater differences become apparent between the two runs. In the run with the non-equilibrium cooling and chemistry, the cold gas fraction remains small up to $t \sim 25$ Myr, but thereafter begins to increase rapidly. On the other hand, in the run with the Koyama & Inutsuka cooling function, the cold gas fraction grows steadily from time $t \sim 20$ Myr until the end of the simulation, at a somewhat faster rate than during the inflow phase. In the interval $20 < t < 28$ Myr, there is more cold gas in the Koyama & Inutsuka run than in the non-equilibrium run, but at later times the latter run has the most cold gas. Figure 3.3 also indicates that the volume filling factor of the cold gas in the Koyama & Inutsuka run is larger than in the other run, although the difference between the two is not large. We can understand the difference in the behaviour of the cold gas fraction in the two run by looking at how the velocity field generated in the cloud differs between the runs, which we examine in the next section.

3.3.2 Cloud structure and velocity

In Figure 3.4, we show projections of the column density of hydrogen nuclei, N , along the axis of the flow at three comparable output times for both of our simulations. The left-hand panels show the results for the run with the Koyama & Inutsuka cooling function, while the right-hand panels show the results from our non-equilibrium

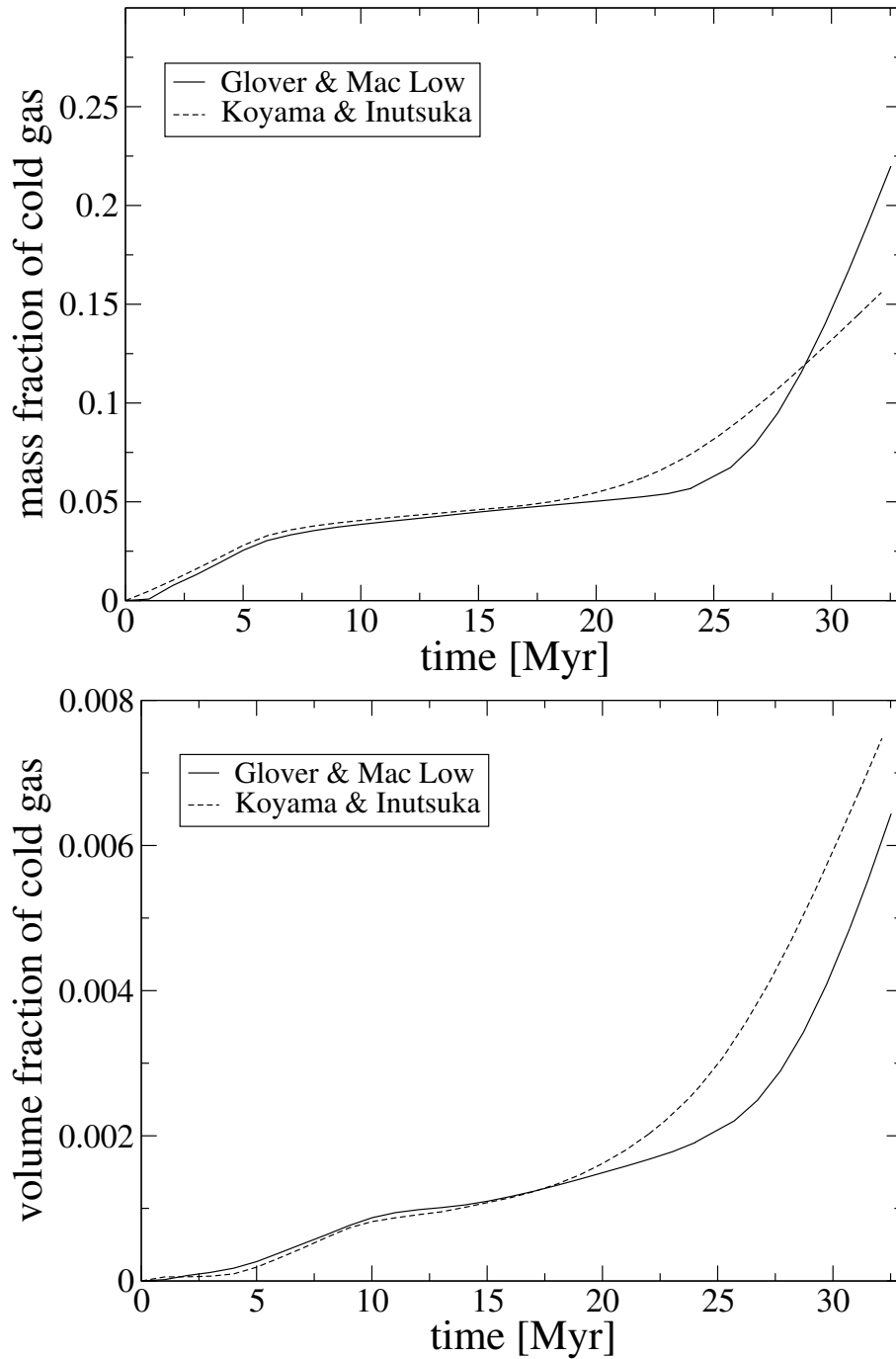


Figure 3.3: Evolution with time in our two simulations of the mass (top panel) and volume (bottom panel) fractions of cold gas, defined here as gas with temperature $T \leq 300\text{K}$. The solid line is for the run with the non-equilibrium chemical model, while the dashed line is for the run with the Koyama & Inutsuka cooling function.

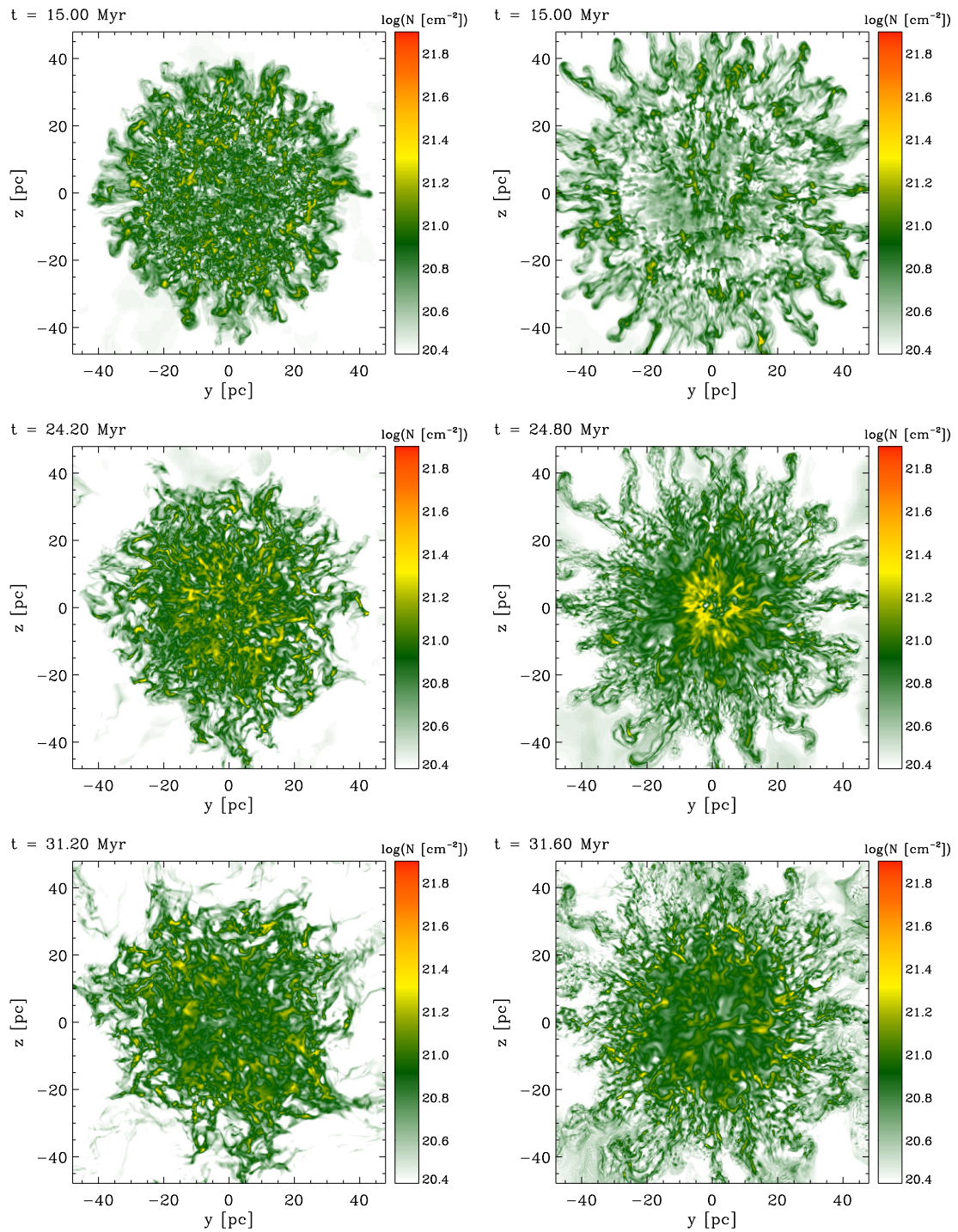


Figure 3.4: Column density of the inner region of the dense cloud viewed face-on at three different output times: $t \sim 15$ Myr, $t \sim 25$ Myr and $t \sim 32$ Myr. The left-hand panels show the results from the run that used the Koyama & Inutsuka cooling function, while the right-hand panels show the results from the run with the full non-equilibrium treatment. Note that output times considered here and in Figures 3.5–3.6 below are slightly different in the two runs owing to minor differences in the timing of the output snapshots produced by FLASH in the two different simulations.

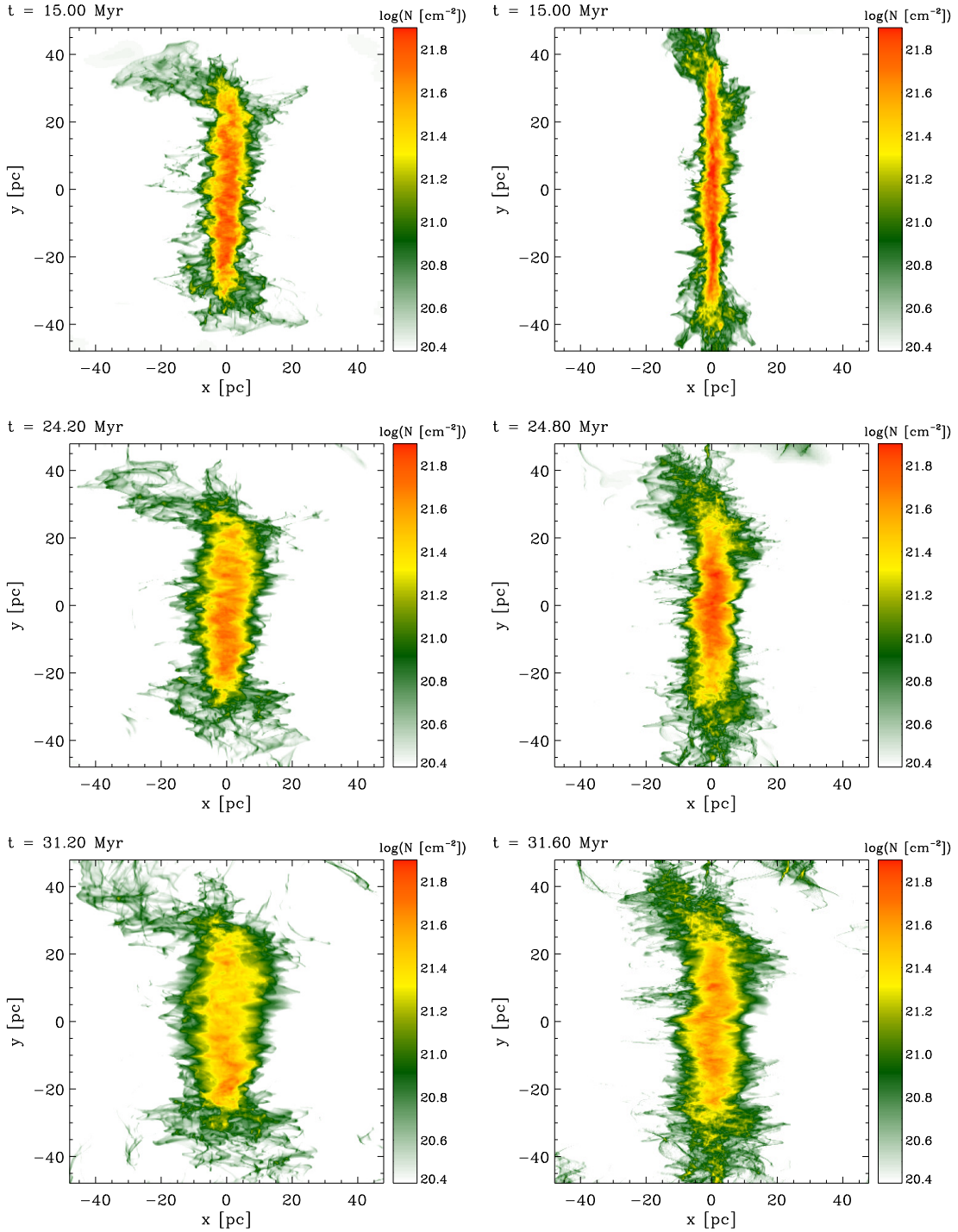


Figure 3.5: Column density of the inner region of the dense cloud viewed edge-on at three different output times: $t \sim 15$ Myr, $t \sim 25$ Myr and $t \sim 32$ Myr. The left-hand panels show the results from the run that used the Koyama & Inutsuka cooling function, while the right-hand panels show the results from the run with the full non-equilibrium treatment.

chemistry run. Figure 3.5 shows a similar comparison, but for a direction perpendicular to the flow.

The images in Figure 3.4 show us clearly that the cloud is not a homogeneous entity, but rather is composed of numerous dense clumps embedded in lower density filaments. Moreover, by comparing the results of the two runs, one can see clearly that the cloud morphology is sensitive to the details of the thermal treatment adopted. In the run with the Koyama & Inutsuka cooling function, the clumps and filaments are contained within a region that is still roughly circular, and that has a radius that is only slightly larger than the initial radius of our inflowing gas ($R \sim 37$ pc at $t = 15$ Myr, compared with $R = 32$ pc initially). On the other hand, in the non-equilibrium chemistry run, the dense gas occupies a significantly larger region, and is less circular, having an edge that is dominated by long, thin filaments of gas. The larger size of the cloud in the non-equilibrium run is also clearly apparent in the side-on view (Figure 3.5).

Looking at the velocity distribution of the gas perpendicular to the flow (i.e. the radial velocities shown in Figure 3.6 for a slice through the centre of the dense cloud), we see that the immediate cause of the difference in morphologies is a difference in the velocity distributions. In the Koyama & Inutsuka run, the net outward velocity of the dense gas is very small. In the non-equilibrium chemistry run, on the other hand, the gas near the axis of the inflow is relatively static, but the dense gas close to the edges of the distribution is largely flowing outwards. In particular, the gas in the filaments has outward velocities of as much as 2 km s^{-1} .

As the dense gas moves outwards in the non-equilibrium chemistry run, it drags the magnetic field lines along with it. The magnetic tension generated by this disturbance of the field lines exerts an inwards force on the expanding gas, and this force eventually becomes strong enough to reverse the direction of the flow. This effect can be seen quite clearly when we look at the column density distribution and velocity field at $t \sim 25$ Myr (the middle panels of Figures 3.4–3.6). The gas distribution has become more compact, resulting in higher column densities, particularly close to the central axis of the flow, and more of the gas is flowing in than is flowing out. At an even later time ($t \sim 32$ Myr; bottom panels in Figures 3.4–3.6), the flow has “bounced” and has begun to re-expand once more. Looking at the results from the run with the Koyama & Inutsuka cooling function, we see hints of similar behaviour, but in this case both the initial outflow and the subsequent inflow are much weaker.

The root cause of the difference in behaviour between the two runs is the thermal evolution of the shock-heated gas in the central cloud. The two inflowing streams of gas each are moving at a speed of 7 km s^{-1} , and so their relative velocity is 14 km s^{-1} ,

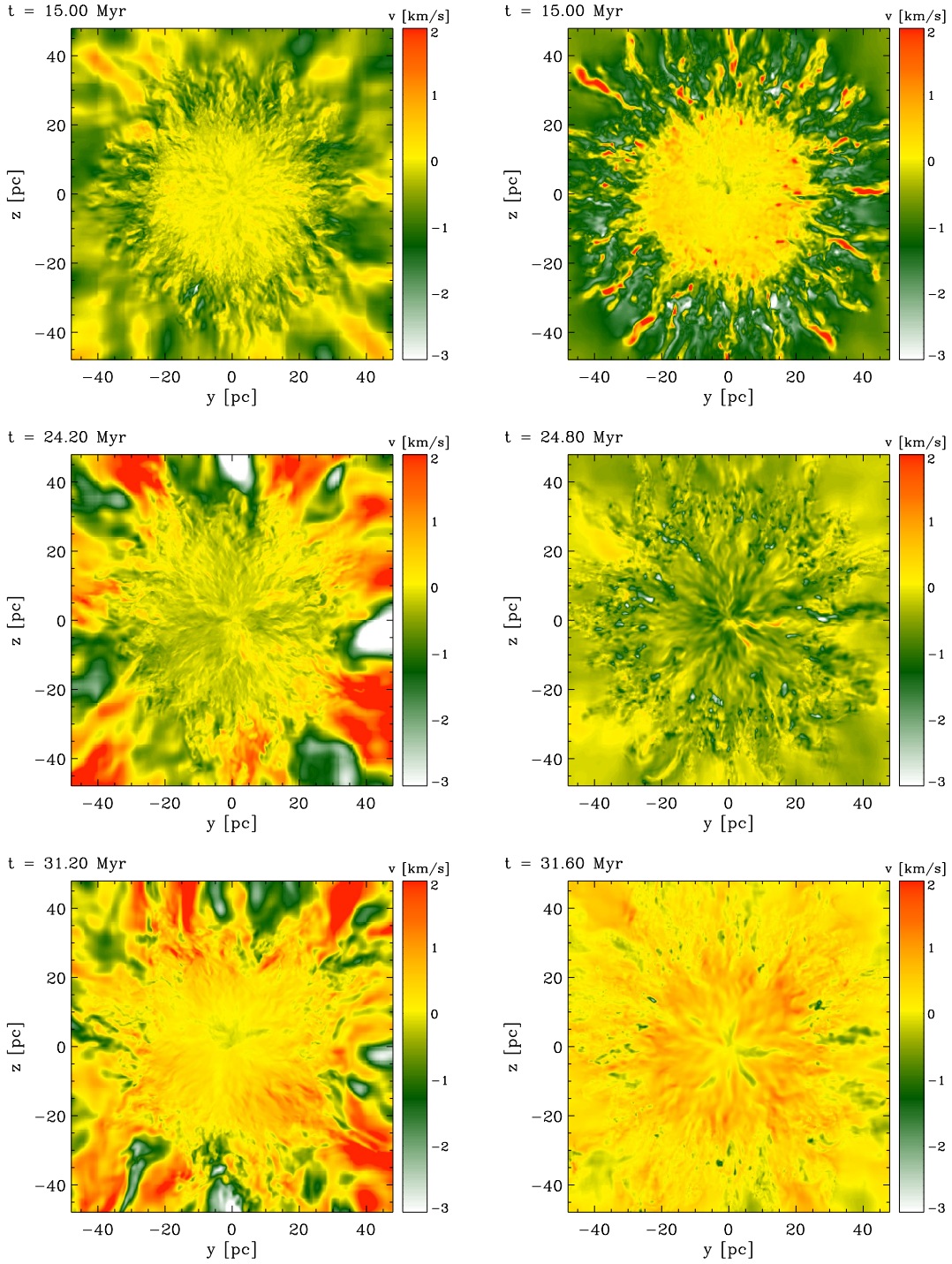


Figure 3.6: Radial velocity of the gas in a slice through the centre of the cloud, relative to the gas at the centre of the cloud. As in Figures 3.4 and 3.5, we plot results from three different output times ($t \sim 15$ Myr, $t \sim 25$ Myr and $t \sim 32$ Myr) for both the simulation using the Koyama & Inutsuka cooling function (left-hand panels) and the full non-equilibrium treatment (right-hand panels).

or around 2.5 times the speed of sound in the warm gas. When the gas collides, it passes through a shock, which heats it and compresses it. We can estimate the post-shock density and temperature by applying the standard shock jump conditions. Since the magnetic field in our simulations is oriented along the flow, it plays no role in determining the post-shock conditions, and the same conditions apply as for a purely hydrodynamical shock. For the density, we therefore have the relationship

$$\frac{\rho_2}{\rho_1} = \frac{(\gamma + 1)\mathcal{M}^2}{(\gamma - 1)\mathcal{M}^2 + 2}, \quad (3.11)$$

where ρ_1 is the pre-shock density, ρ_2 is the post-shock density, and γ is the adiabatic index of the gas. For the temperature, we have the relationship

$$\frac{T_2}{T_1} = \frac{\left(1 + \frac{\gamma-1}{2}\mathcal{M}^2\right) \left(\frac{2\gamma}{\gamma-1}\mathcal{M}^2 - 1\right)}{\mathcal{M}^2 \left(\frac{2\gamma}{\gamma-1} + \frac{\gamma-1}{2}\right)}, \quad (3.12)$$

where T_1 and T_2 are the pre-shock and post-shock temperatures, respectively. For the case of $\mathcal{M} = 2.5$ and $\gamma = 5/3$, we therefore find that $\rho_2 \simeq 2.7\rho_1$ and $T_2 \simeq 2.8T_1$. The post-shock thermal pressure is therefore a factor of around 7.6 larger than the pre-shock thermal pressure, which itself is the same as the thermal pressure of the surrounding gas not participating in the inflow. The shocked gas is therefore over-pressured relative to its surroundings, and the resulting pressure gradient causes the gas to expand in the directions perpendicular to the inflow. In the inflow direction, it is confined by the ram pressure of the flow. The effectiveness with which this pressure gradient can accelerate gas outwards from the central cloud depends on the length of time the gas remains in this over-pressured state. If we assume that the initial cooling of the gas is isochoric (i.e. that there is no change in its density), then it will cease to be over-pressured once its temperature drops below $T_1\rho_1/\rho_2$, which for the case considered above and an initial temperature of 5000 K yields $T \sim 1850$ K.

In Figure 3.7, we show how the temperature of a parcel of gas with density $n = 2.7\text{cm}^{-3}$ and temperature $T = 14000$ K changes as a function of time when we model heating and cooling using the Koyama & Inutsuka cooling function (dashed line) or our full non-equilibrium treatment (solid line). In the latter case, we take the initial chemical state of the gas to be the same as in our simulations. We see that when we use the Koyama & Inutsuka cooling function, the gas cools very rapidly at early times, returning to its original temperature after only 0.3 Myr. Subsequently, it cools more slowly, and it ceases to be over-pressured with respect to the unperturbed gas after around 1.3 Myr. On the other hand, when we model the chemistry and cooling of the gas using our non-equilibrium model, we see that it takes considerably longer for the

gas too cool. In this case, the temperature of the gas returns to its original value after around 1.2 Myr, and the gas remains over-pressured until $t \sim 2.45$ Myr. These results demonstrate that when we use our non-equilibrium treatment to model the cooling of the gas, it remains significantly over-pressured for a much longer period than when we use the Koyama & Inutsuka cooling function. In the former case, therefore, the gas is accelerated by an outward-pointing pressure gradient for a longer period of time, and hence attains a significantly higher outward velocity, accounting for the differences we see in the morphology of the cloud and the velocity structure of the gas.

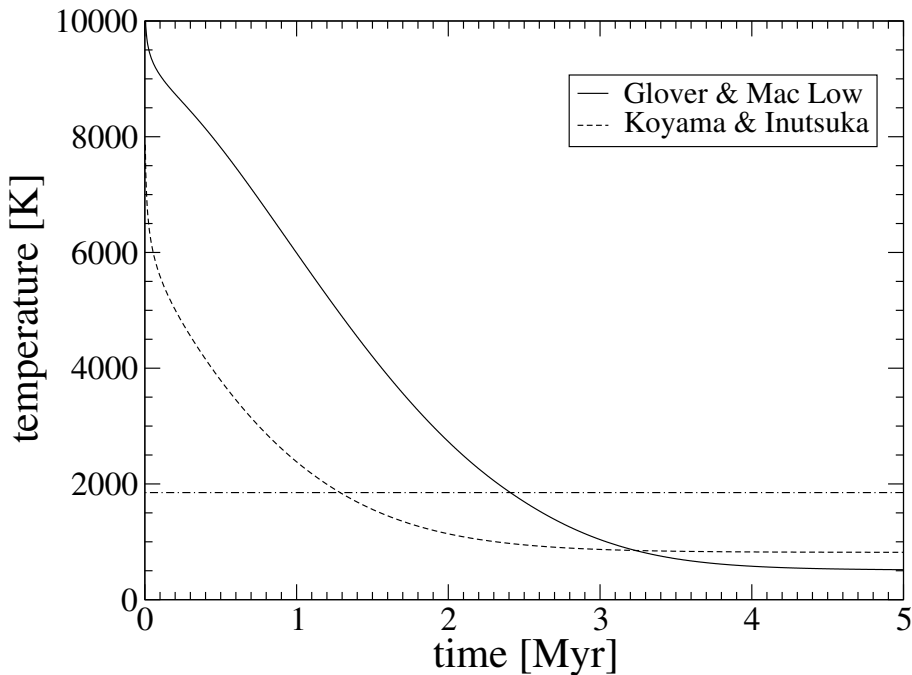


Figure 3.7: Evolution with time of the temperature of a fluid element with initial density $n_i = 2.7 \text{ cm}^{-3}$ and initial temperature $T_i = 14000 \text{ K}$, evolving at constant density. The initial chemical state of the gas, the strength of the UV radiation field, the cosmic ray ionisation rate and the metallicity are all taken to be the same as in our colliding flow simulations. The solid line shows the temperature evolution that we obtain when we model the gas using our non-equilibrium chemical model and cooling function, while the dashed line shows the results that we obtain when we use the Koyama & Inutsuka cooling function. The horizontal dash-dotted line shows the temperature at which the thermal pressure of the gas is the same as that of the unperturbed WNM in our colliding flow simulations.

3.3.3 Clump properties

Finally, we explore whether the differences in cloud morphology and in the velocity field of the gas lead to significant differences in the statistical properties of the dense

clumps formed in the flow. Although the fact that we do not include self-gravity in our models prevents us from following the further evolution of this dense gas in detail, we know from previous studies that it is the ongoing growth and merger of these dense clumps that eventually leads to the formation of gravitationally unstable pre-stellar cores and, ultimately, stars (see e.g. Banerjee et al. 2009; Vázquez-Semadeni et al. 2011). Differences in the clump properties at an early stage may therefore be indicative of differences in the ability of the clouds to form stars.

We identify clumps in our simulations by searching for connected regions with densities above 50 cm^{-3} . For reasons of computational efficiency, we restrict our search for clumps to radial distances $R \leq 40 \text{ pc}$ from the central axis of the flow, but from Figure 3.4 we can clearly see that this region contains almost the entire mass of dense gas, and so we are unlikely to miss many clumps. In Figure 3.8, we show some of the averaged internal properties of the clumps at times $t \sim 15 \text{ Myr}$, $t \sim 25 \text{ Myr}$, and $t \sim 32 \text{ Myr}$ for both models.

The top panels of these figures show the ratio of the clump mass M to the local Jeans mass M_J , plotted as a function of the clump mass. The masses of the clumps span a wide range, $0.1\text{--}10^3 M_\odot$. However, the vast majority of the clumps are not self-gravitating, since they have $M/M_J < 1$. The only exceptions are a couple of clumps present at $t = 15 \text{ Myr}$ that have $M \sim 1\text{--}2 M_J$. We therefore see that in order to form a significant number of self-gravitating clumps – a necessary pre-requisite for star formation – the compressions produced by the collision of the flows and the consequent thermal instability are not sufficient; some form of large-scale collapse of the cloud is also required. This is also evident in simulations including self-gravity, where in the case of a critical setup the presence of magnetic fields suppress star formation (Vázquez-Semadeni et al. 2011). Similar results have been found in a number of other studies (see e.g. Koyama & Inutsuka 2002; Heitsch et al. 2005; Vázquez-Semadeni et al. 2007).

Comparing the clump properties in the different models, we see that the mean density of the clumps is not particularly sensitive to the way in which the cooling of the gas is modelled, although there is a tentative hint that the clumps in the simulation with the Koyama & Inutsuka cooling function may be slightly denser than in those in the other simulation. A more pronounced difference is apparent in the mean temperature of the clumps, which we find is roughly 10 K higher when we use the non-equilibrium treatment than when we use the Koyama & Inutsuka cooling function. This difference is due to the difference in the photoelectric heating rate assumed in the two simulations, as noted in Section 3.3.1 above, and leads to minor differences in the Jeans masses that we determine for our clumps, as one can see from the upper panels in Figure 3.8.

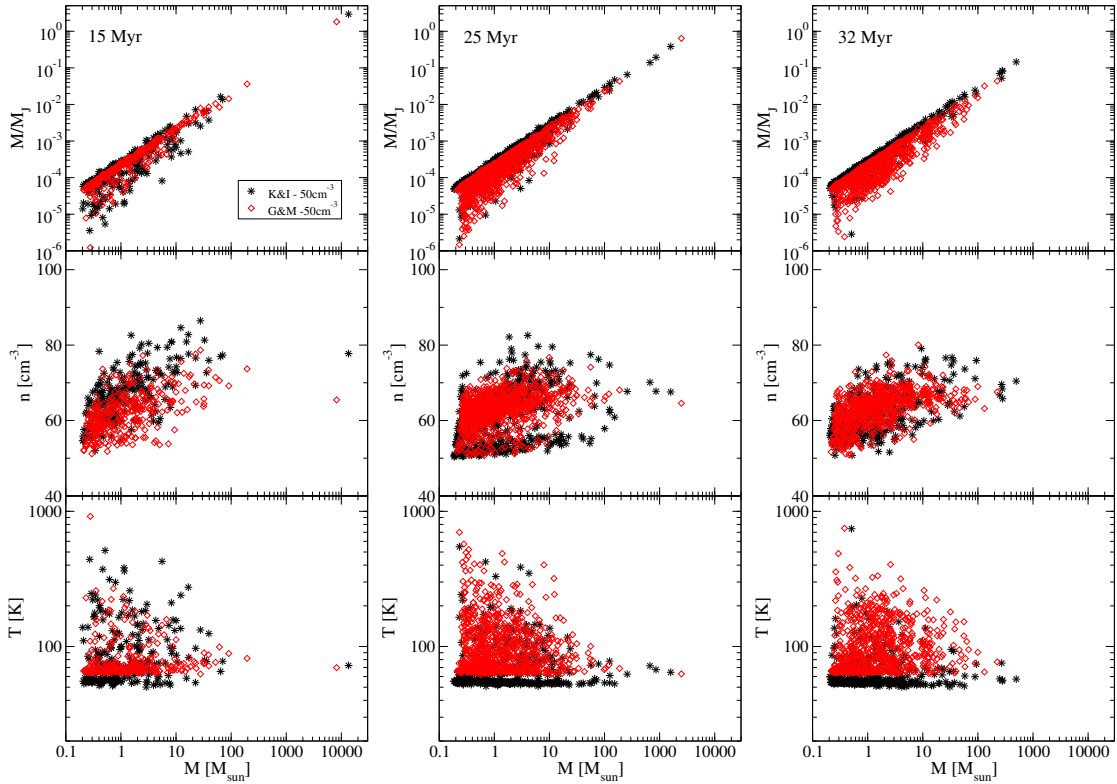


Figure 3.8: Properties of the set of dense clumps identified as described in Section 3.3.3. Results are shown for three output times: $t \sim 15$ Myr (left-hand panels), $t \sim 25$ Myr (central panels) and $t \sim 32$ Myr (right-hand panels). The upper row of panels shows the ratio of the clump mass to the local Jeans mass, M/M_J , the central row shows the mean density of the clumps and the lower row shows the mean temperature. In each case, we plot these quantities as a function of the total clump mass.

However, it should be noted that *both* simulations likely overestimate the temperature of these dense clumps, owing to their neglect of the effects of dust shielding (c.f. Glover & Clark 2012b,c; Clark et al. 2012b).

3.4 Summary

We have presented the results of a study that examines the influence of two different thermal models on the formation of cold, dense clouds within converging flows of warm atomic gas, and on the nature of the clumps that form within these clouds. To do this, we performed high-resolution 3D MHD simulations using the massively parallel code FLASH, modified to include a detailed treatment of atomic and molecular cooling, and a simplified but accurate treatment of the most important hydrogen chemistry (Micic et al. 2012a). We directly compare the results obtained from this model with

those that we obtain if we use a simplified cooling function, taken from the work of Koyama & Inutsuka (2002), that has been used in a number of other studies of cloud formation in converging flows (see e.g. Banerjee et al. 2009).

We find that the density and temperature PDFs produced in the two simulations are qualitatively similar, although some minor quantitative differences exist. In common with previous work (e.g. Vázquez-Semadeni et al. 2007; Hennebelle et al. 2008; Banerjee et al. 2009) we find that in addition to clear CNM and WNM phases, there is also a significant fraction of mass located in the thermally unstable region between these two phases. The temperatures recovered for the CNM and WNM phases are slightly smaller in the simulation run with the Koyama & Inutsuka cooling function, as their approach significantly overestimates the cooling rate of hot ($T \sim 10^4$ K) gas and underestimates the photoelectric heating rate in the CNM regime by a factor of 2.5. In the Koyama & Inutsuka model, most of the gas is in thermal equilibrium, while in the full non-equilibrium model, significant deviations from thermal equilibrium are apparent for gas in the density range $1 < n < 30 \text{ cm}^{-3}$. In this intermediate density regime, the photoelectric heating efficiency has not yet reached its limiting value and increases with increasing electron number density. Due to the relatively long recombination timescale, the gas is slightly more ionised than it would be in chemical equilibrium, and hence is heated slightly more efficiently.

We have also shown that the cloud morphology is sensitive to the choice of the thermal treatment. The cloud formed in the non-equilibrium chemistry run is larger and more filamentary than the cloud formed in the run with the Koyama & Inutsuka cooling function. This difference in morphology is caused by a difference in the velocity distribution of the gas, which itself can be understood as a consequence of the difference in the cooling time of hot gas in the two models. In the Koyama & Inutsuka model, the high temperature, shock-heated gas cools very rapidly, and the gas remains over-pressure with respect to its surroundings for only a very short time. With the full non-equilibrium treatment, however, the cooling time is significantly longer and hence the cloud remains over-pressured for longer. Consequently, the gas is accelerated outwards more efficiently, resulting in a larger, more disordered gas distribution.

Finally, we have investigated whether the properties of the clumps that form in the clouds differ significantly between the two runs. We have identified clumps with masses in a range of $0.1\text{--}10^3 M_{\odot}$ in both simulations, but find that almost all of these structures are not self-gravitating, having $M/M_J < 1$. This suggests that the compressions produced by the collision of the flows followed by thermal instability are not sufficient to lead to the formation of gravitationally unstable pre-stellar cores and stars. In order for star formation to happen, some form of large-scale collapse of

the cloud appears to be necessary, as previously noted by Koyama & Inutsuka (2002), Heitsch et al. (2005), and Vázquez-Semadeni et al. (2007). Most of the properties of the clumps are very similar in our two models, with the most significant difference being a systematic offset of roughly 10 K between the mean clump temperatures in the Koyama & Inutsuka model and those in the non-equilibrium model. However, it should be noted that both models overestimate the temperature of the clumps, owing to their neglect of the effects of dust shielding.

4 Modelling C I emission: C I as a column density tracer

In this chapter we study C I and CO emission from molecular clouds in comparison to their column densities and the total column density, as we look for the way to trace the structure of the cloud. For this purpose, we adopt the smooth particle hydrodynamics (SPH) simulations of a typical nearby molecular cloud, performed by Glover & Clark (2012c).

We find that the intensity of integrated C I emission increases as the function of total column density toward the center of the cloud until the density becomes so large that the emission reaches saturation at maximum intensity as most of the atoms are in the excited state. As the result C I emission is not a good tracer of C I column density.

On the other hand, C I is a good tracer of the cloud structure. We find that the velocity integrated intensity of C I matches the intensity of CO in almost the entire cloud. Only at the edges the C I intensity becomes dominant as photodissociation destroys CO molecules. Since C I dominates the shell at the surface of the cloud, it is also a good tracer of low extinction material.

4.1 – Prologue –

Earlier we have mentioned that our galaxy, the Milky Way, is transparent at radio wavelengths. The interstellar gas in its various phases emits radio lines that can be observed in emission over large areas of the sky and, therefore, most of the studies of the interstellar medium on large scales have been pursued through radio surveys. The line shapes are easily resolved by radio spectroscopic techniques and reflect the motion of the ISM on the galactic scale and the internal dynamics of clouds. Having that molecular clouds are primarily composed of molecular hydrogen, H_2 , which is difficult to observe due to the lack of a dipole moment and the unstable conditions within the clouds to excite its rotational transitions, through many years the main focus of molecular cloud research has been on the second-most abundant molecular species – carbon monoxide CO. CO has a dipole moment with rotational transitions that are easily excited at typical MC temperatures (10 – 100 K) and densities ($\gtrsim 100 \text{ cm}^{-3}$), explaining why CO observations are often employed to investigate the properties of molecular clouds and revolutionise our understanding of the birthplaces of all stars.

One of the important revelations was the existence of a thin layer of neutral atomic carbon, C I or C^0 , found between C^+ and CO, that traces the photon-dominated regions in the outer envelopes of molecular clouds (Tielens & Hollenbach 1985). These photodissociation regions (PDRs) represent the transition between atomic and molecular phases of the interstellar medium. UV photons with energies greater than the hydrogen ionisation threshold of 13.6 eV, originating for example from a neighbouring early-type star, create an H II region surrounding the energetic star. UV photons with energy less than this threshold escape from the H II region into neighbouring molecular cloud, where photodissociation of dominant molecules such as H_2 and CO takes place. In these regions also comes to the photoionisation of the atoms with an ionisation threshold lower than that of hydrogen. Such atom is carbon that ionises with photon energies as low as 11.26 eV and has already been predicted to be abundant in the regions of low visual extinction where UV radiation can penetrate and dissociate CO (Langer 1976; Meixner & Tielens 1993). The combined effect of CO photodissociation and C^0 photoionisation by UV photons produces a layered structure of $\text{C}^+/\text{C}^0/\text{CO}$ surrounding the H II region and extending into the molecular cloud.

Originally has been expected that the abundance of C I would be high only at cloud surfaces subjected to a FUV radiation field (Langer 1976), but in reality, the emission from the fine-structure line of carbon at 492 GHz is observed to be widespread, even in clouds where there are no strong sources of UV radiation, such as TMC-1 (Schilke et al. 1995). This widespread observation of C I in molecular clouds has been shown to have significant contributions to the emission from atoms deep within the cloud where

A_V is as high as 50–100 (Frerking et al. 1989; Little et al. 1994).

Neutral carbon plays important role in cooling and chemical processes in interstellar clouds. The observable C I transition at 492GHz has a minimum excitation temperature of 24 K and critical density $n \sim 10^3 \text{ cm}^{-3}$ for collisions with H_2 (see e.g., Schroder et al. 1991). Therefore, it is easily excited in dense interstellar gas.

However, none of the proposed numerical models until now have performed the study of C I emission in real GMCs fashion, with self-consistent thermal and chemical treatment of the gas in molecular clouds. Therefore, in this chapter, we address this issue by exploring the properties of C I distribution in a model of a typical, small molecular cloud found in the neighbouring environment in the Milky Way.

The outline of this chapter is as follows. In §4.2 we describe our numerical method, paying particular attention to the principles used to calculate the radiative transfer of level populations. In §4.3 we discuss our results and close with a summary of our findings in section 4.4.

4.2 Numerical Method

For this study we adopt the simulations performed by Glover & Clark (2012c). Their simulations of the molecular cloud model track the evolution of gas using a modified version of smooth particle hydrodynamics (SPH) code GADGET 2 (Springel 2005). It has been modified in the manner to include treatment of the gas-phase chemistry introduced in Glover & Mac Low (2007a,b), and the radiative heating and cooling from a number of atomic and molecular species (Glover & Jappsen 2007; Glover et al. 2010; Glover & Clark 2012b). The hydrogen chemistry network in the model (described also in sections 2.2.1 and 3.2.2) is combined with the treatment of CO formation and destruction proposed by Nelson & Langer (1999). The modifications do not include the effects of the freeze-out of CO on to dust grains, as they have a very little effect on the thermal balance of the gas (Goldsmith 2001). Dust extinction, H_2 self-shielding, CO shielding and the shielding of CO by H_2 is treated with TREECOL algorithm developed by Clark et al. (2012a). We refer the reader to Glover & Clark (2012c) for further details of their inclusions to the model.

The cloud is initially in the form of an uniform sphere with radius of approximately 6 pc. An initial total mass of the sphere is $\sim 10^4 M_\odot$, with initial hydrogen nucleus number density of 300 cm^{-3} . The simulated cloud is corresponding to the environments found in a small, nearby molecular clouds, such as e.g. the Perseus or Taurus molecular

clouds. We follow the evolution of the gas with constant solar metallicity, where the turbulence is allowed to freely decay via shocks and compression-triggered cooling. The initial turbulent velocity field has the wavenumber of $\propto k^{-4}$, leading to the initial rms turbulent velocity of $\sim 3 \text{ km s}^{-1}$. The initial gas and dust temperatures are set to 20 K and 10 K, respectively. These values couple rapidly at the beginning of the simulation, as the gas and dust relax towards thermal equilibrium.

Finally, all of the available carbon is assumed to be in the form of C^+ at the start of the simulation. We also assume that all of the available oxygen starts in neutral atomic form. We adopt the cosmic ray ionisation rate of 10^{17} s^{-1} .

4.2.1 Radiative transfer

The level transition in C I line emission is modelled with the three-dimensional radiative transfer code RADMC-3D (Dullemond 2012). Further details on the operation of the code can be also found in Shetty et al. (2011). Here we briefly show the basic principles of the radiative transfer used in our calculations.

In order to calculate the line radiative transfer one needs to solve equations for the population levels of the atomic or molecular species in question. The occupation of a given energy level of an atom depends on the incident radiation field, and the frequency of collisions with other atoms or molecules, both acting as excitation or de-excitation mechanisms. Detailed balance of the relative population of level i , f_i , in statistical equilibrium is described with the equation:

$$\sum_{j>i} [f_j A_{ji} + (f_j B_{ji} - f_i B_{ij}) \bar{J}_{ji}] - \sum_{j<i} [f_i A_{ij} + (f_i B_{ij} - f_j B_{ji}) \bar{J}_{ij}] + \sum_j [f_j C_{ji} - f_i C_{ij}] = 0 \quad (4.1)$$

where A_{ij} is the Einstein coefficient for spontaneous emission for a transition from level i to level j , B_{ij} is the Einstein coefficient for stimulated emission from level i to level j , and B_{ji} is the corresponding coefficient for absorption. The last summation accounts for collisions, where C_{ij} is the collisional rate for a transition from level i to level j . The collisional rate depends on the rate coefficient K_{ij} and the density of species that the atom in consideration is colliding with, n_{col} : $C_{ij} = n_{col} K_{ij}$. In molecular clouds, the main collisional partners of C I are H_2 and CO , thus we neglect the effect of collisions with other partners.

The first two summations in Equation 4.1 account for the influence of radiation on

setting the level populations by including the mean integrated intensity J_{ij} of the radiation field in the line corresponding to the transition from i to j . This equation is coupled with the equation of radiative transfer

$$\frac{dI_\nu}{d\tau_\nu} = -I_\nu + S_\nu, \quad (4.2)$$

where I_ν is the specific intensity, S_ν the source function, and τ_ν is the optical depth. The amount of radiation emitted from molecules in a given location is dependent on the level populations through

$$S_{ij} = \frac{f_i A_{ij}}{f_j B_{ji} - f_i B_{ij}}, \quad (4.3)$$

and:

$$\bar{J}_{ij} = \frac{1}{4\pi} \int I_{ij} \phi_{ij} d\Omega, \quad (4.4)$$

where the integral is taken over all solid angles Ω . At the same time the level populations depend on the amount of incident radiation at that location. Solving this problem numerically can be computationally expensive. However, certain situations allow us to make suitable approximations that will significantly reduce the computational costs. In particular, in gaseous systems such as the one under our consideration, the collisional processes dominate line emission meaning that the temperature is the only parameter that is required to calculate the population levels. This is done through the use of a partition function, assuming the local thermodynamic equilibrium (LTE) in regions with high H_2 and CO densities.

4.2.2 The Sobolev approximation

In order to solve for the population levels of an atomic or molecular species, we use the Shetty et al. (2011) implementation of the Sobolev approximation (Sobolev 1957) into RADMC-3D. This method, also known as the Large Velocity Gradient (LVG) method, uses the large spatial variations in velocity present in turbulent molecular clouds to define line escape probabilities and essentially provides a solution to the equation of detailed balance (Eq. 4.1 (see e.g. Mihalas 1978)).

Let us, for example, consider a photon emitted in a transition from level i to level j . Moving away from the position where this photon is emitted, its Doppler-shifted frequency associated with the i to j transition starts to differ from the initial one due to the velocity gradient in the medium. At a certain distance, the frequency becomes

sufficiently different so that the photon cannot interact with the matter at this nor any subsequent position and propagates freely out of the cloud. Then the LVG escape probability of the photon can be determined from the optical depth τ :

$$\beta = \frac{1}{\tau} \int_0^\tau e^{-\tau'} d\tau' = \frac{1 - e^{-\tau}}{\tau} \quad (4.5)$$

Once the optical depth is computed in accordance to (van der Tak et al. 2007), we can determine the local radiation field by

$$\bar{J}_{ij} = S_{ij}(1 - \beta). \quad (4.6)$$

By obtaining these expressions for τ , β , \bar{J} and the local velocity gradient, one can iteratively solve for the population levels in equation 4.1.

4.2.3 C I emission

In this chapter we investigate how well C I emission can trace the intrinsic C I and CO column densities N_C and N_C respectively, CO integrated intensity and the total column density of hydrogen nuclei N_{tot} . The intrinsic column densities are calculated directly from the simulation by integrating the C I, H₂ and hydrogen nuclei volume densities along a given axis. Accordingly, in order to perform the calculation of radiative transfer, the simulation cube is oriented such that the C I line is observed along the same axis for which the column densities are computed.

Given that H₂, the major constituent of N_{tot} in molecular clouds, is difficult to observe directly, observers are often required to indirectly measure the total column density by measuring the extinction A_V . By doing so, they estimate the total amount of dust along the line of sight, that further, using the assumption for the dust-to-gas ratio, directly gives the value of total gaseous column density (Bohlin et al. 1978). In order to allow direct comparison of models with observational analyses, we adopt the conversion of N_{tot} to an extinction A_V and vice versa:

$$A_V = \frac{N_{\text{tot}}}{1.87 \times 10^{21}} \left(\frac{Z}{Z_\odot} \right), \quad (4.7)$$

where Z is the metallicity of the gas.

The 3D spectral (position-position-velocity, or PPV) cubes of the C I line, produced in radiative transfer calculations, indicate the intensity I_ν in a given frequency or velocity

channel of width $d\nu$ at each 2D position, in units of $\text{erg s}^{-1} \text{cm}^{-2} \text{Hz}^{-1} \text{sr}^{-1}$. Given that the C I line is located in the Rayleigh-Jeans part of the spectrum and, thus, $I_\nu \propto T_B$, we can express the intensity as a velocity-integrated brightness temperature:

$$W_C = \frac{1}{2k_B}(c/\nu)^2 \int I_\nu d\nu \quad [\text{K km s}^{-1}]. \quad (4.8)$$

This integrated intensity is, in fact, a measure of total C I emission along the line of sight.

4.3 Results

4.3.1 C I column density and intensity distribution

We start investigating C I emission by looking at the correlation of velocity integrated C I intensity W_C with the total column density N_{tot} , presented in Figure 4.1. The bottom abscissa of the figure represents N_{tot} , while the top abscissa shows the corresponding A_V (see equation 4.7). We see that the intensity of integrated C I emission increases with the increasing total column density. This is expected as the lower density regions correspond to the line of sight through the cloud outskirts. As the column density increases toward the cloud center, the collisional excitation becomes greater and so does the intensity of integrated C I emission. However, as the density increases, more atoms are at the excited states and the emission reaches saturation at maximum intensity of $\sim 10 \text{ K km s}^{-1}$.

C I line saturation is not clearly evident from Fig. 4.1, having that the distribution of C I intensity gets wider with higher extinctions. Even though neutral carbon is mainly destroyed by FUV ionisation, its column density is insensitive to the strength of the external FUV field, as discussed by Tielens & Hollenbach (1985). They have shown that only the depth at which the $\text{C}^+/\text{C}/\text{CO}$ transition occurs is depending on the FUV field (see also Hollenbach et al. 1991; Kaufman et al. 1999). Given that the neutral carbon is formed by FUV photodissociation of carbon-containing molecules (beside electron recombination with C^+ and neutralisation of C^+ by negatively charged PAHs), the intensity of C I emission is seen up to high densities and extinction. In low-density regions, molecules such as CH and CH_2 are not able to react quickly with O to form CO, and are being photodissociated, contributing to the abundance of C. At high densities, photodissociation of CH_2 and CH_3 maintains the C abundance, as well as the reaction $\text{H} + \text{CH} \rightarrow \text{C} + \text{H}_2$.

In Figure 4.2 we show the probability distribution functions (PDFs) of C I column

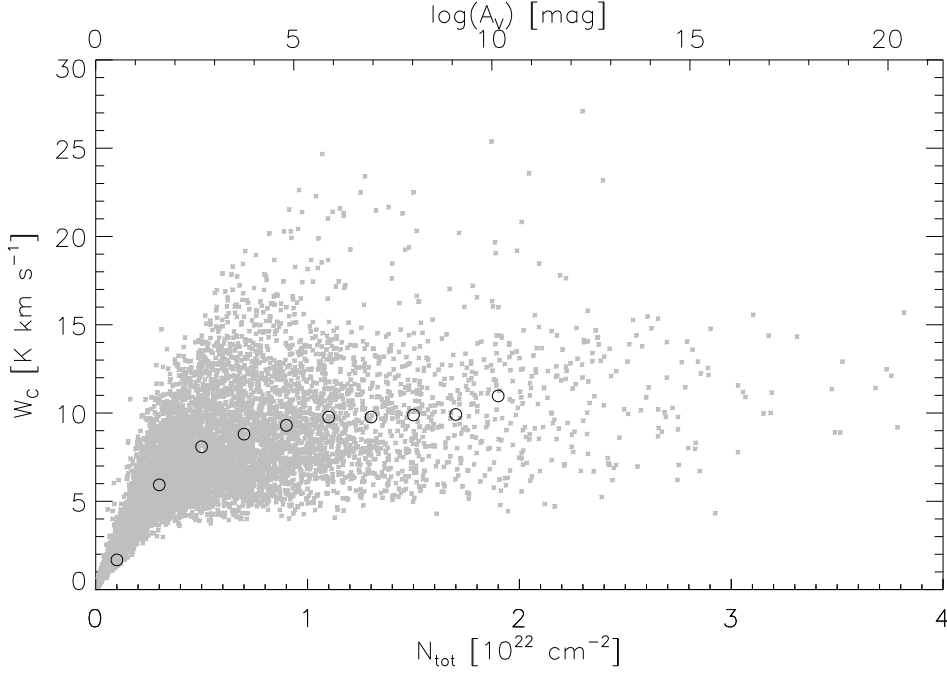


Figure 4.1: Relationship between integrated C I intensity W_C and total column density N_{tot} (bottom abscissa) or extinction A_V (top abscissa). Circles show average W_C values in A_V bins.

density N_C and velocity-integrated C I intensity W_C . The top axis shows the scale of W_C which has the equivalent extend as the scale in N_C shown on the bottom axis. We are expecting that the C I emission should trace the C I density in low-density regime where gas is optically thin. Therefore, we have chosen the absolute scale such that low W_C and N_C values are matching each other as best as possible. It is clear that the shape of the W_C differs significantly of underlying N_C . Even though there is a good correspondence at low densities, at high densities the intensity PDF has a steep gradient, resulting in peak that is not corresponding to the peak of N_C . One possible explanation for this discrepancy might be found in the saturation of C I line. Namely, as a result of the saturation, regions with different C I column densities may have similar intensities, producing the apparent 'piled-up' PDF intensity profile at value of $\log(W_C) = 0.8$.

The solid lines in Fig. 4.2 mark the low-intensity range $-1.5 \leq \log(W_C) \leq -0.1$ where the increase in the intensity corresponds to a similar increase in C I column density in the range of $14.8 \leq \log(N_C) \leq 16.2$. In order to have a closer look of this correlations, in Figure 4.3 we show images of C I column density and line intensity, where each side of the image has a length of 16.2 pc. The solid contours in these figures indicate the

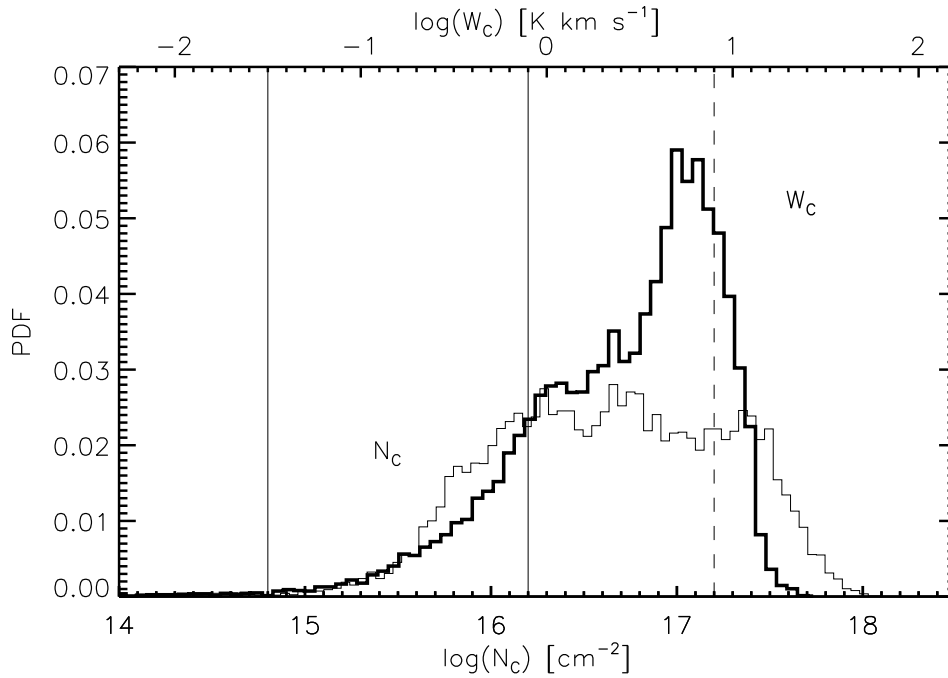


Figure 4.2: C I column density N_C (thin) and integrated C I intensity W_C (thick) PDFs. The bottom abscissa indicate N_C values and top abscissa indicate W_C values. The solid lines mark $\log(N_C) = 14.8$, 16.2 and $\log(W_C) = -1.5$, -0.1 and the dash line mark $\log(N_C) = 17.2$ and $\log(W_C) = 0.9$, for comparison with Fig. 4.3.

same N_C and W_C values as the solid lines in Figure 4.2, showing very good agreement. However, at high intensities, it is evident that the C I emission is not a good tracer of the C I column density. The PDF intensities at $\log(W_C) \geq 0.9$, marked by a dashed line in Fig. 4.2, are presented with dashed contours indicating the corresponding regions in the N_C and W_C maps. The most prominent differences are seen in the morphology of the regions contained within these contours. In the most dense regions, the area within the intensity contour is rather smaller than the one covering the same values in the N_C map. There is clearly no simple correlation between the observed C I intensities and intrinsic C I column densities.

4.3.2 C I and CO correlation

If C I is a good tracer of cloud structure, then one would expect that C I emission comes from the same parts of the cloud with a similar intensity as CO emission. In fact, this is what we find in Figure 4.4. This figure shows velocity integrated intensity ratio between C I and CO emission. For the largest part of the cloud, the intensity of C I emission is quite comparable to CO emission since the ratio is close to one

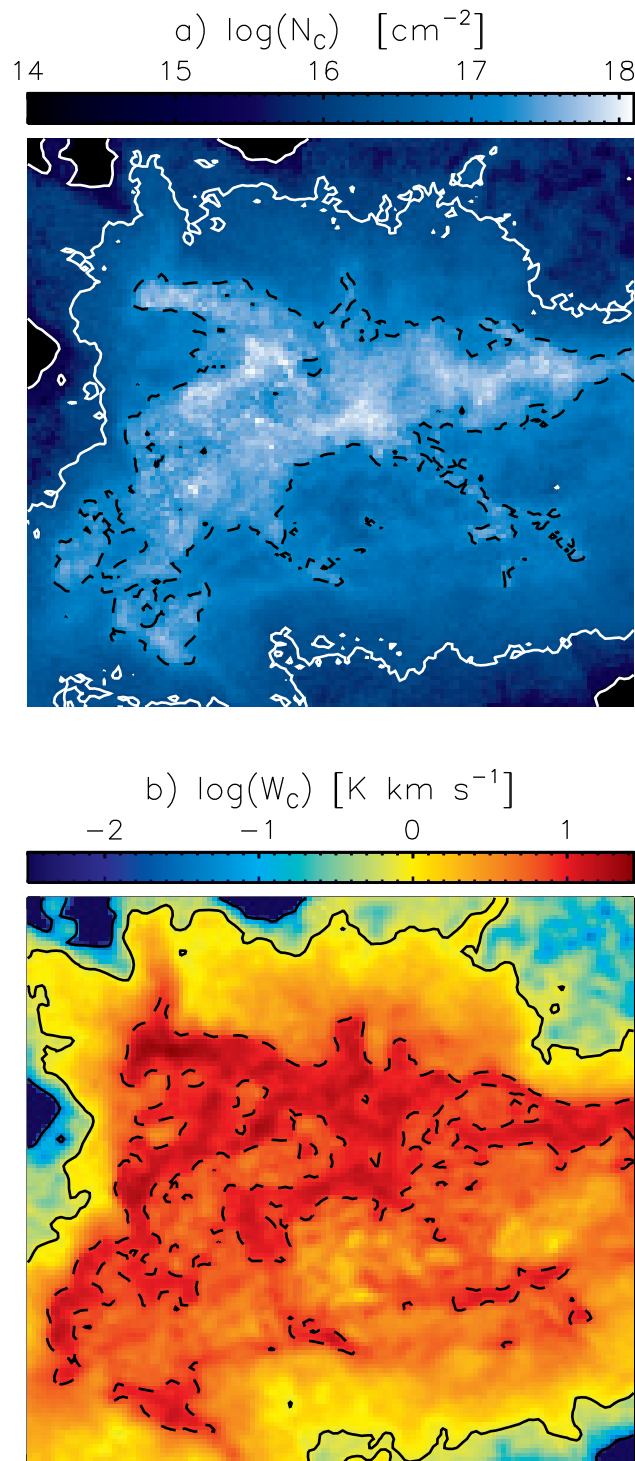


Figure 4.3: Images of (a) N_C and (b) W_C . Each side has a length of 16.2 pc. The solid contours indicate $\log(N_C) = 14.8, 16.2$ and $\log(W_C) = -1.5, -0.1$; dashed contours indicate $\log(N_C) = 17.2$ and $\log(W_C) = 0.9$.

almost everywhere. Only at the edges of the cloud we can see the decrease in CO emission. Dissociation of CO molecules increases toward the outskirts of the cloud and the number density of C I increases. With it, the intensity of C I emission starts dominating over CO emission. This result becomes clear in the following plots.

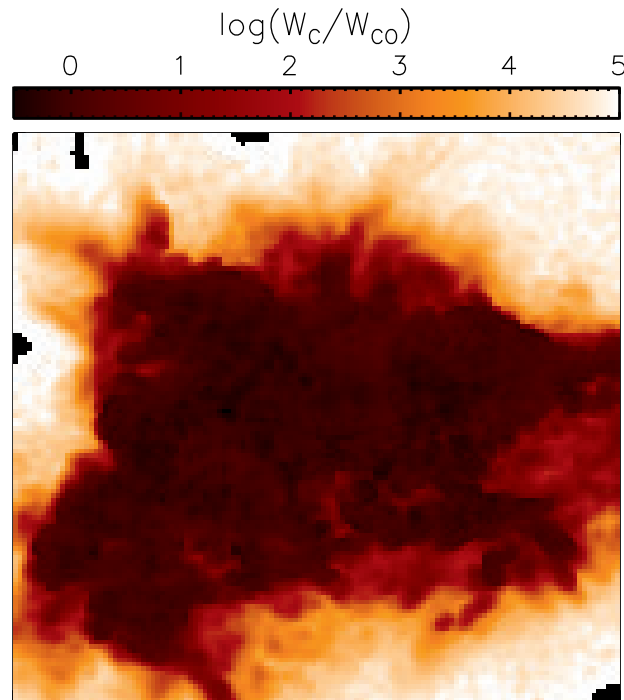


Figure 4.4: Image of C I/CO velocity-integrated intensity ratio W_C/W_{CO} .

In Figure 4.5 we show the C I/CO velocity-integrated intensity ratio as a function of extinction A_V . We find that in the regions where CO is prominent, $A_V > 2$, integrated intensity of C I line emission is in excellent correlation with CO emission. The intensity ratio in these regions is close to unity and is observed even in high density regions. This result is not expected from the classical spherical PDR models. In these models carbon is abundant only in a thin layer on the outside of the cloud at extinction $A_V < 3$ (Keene et al. 1997) where it is being formed by photodissociation of CO. However, our findings are in agreement with the observations of real GMCs suggesting that C I emission indeed trace the CO emission fairly well. The coextensiveness of the C I and CO emission is usually attributed to the clumpy structure of the cloud that is porous to UV radiation (Stoerzer et al. 1996) allowing carbon formation in deeper regions of the cloud.

Figure 4.6 confirms these findings. Here we plot the ratio of C I (solid line) and CO (dashed line) column densities with total hydrogen column density as a function of

extinction. We find that in respect to the total column density, C I density only slightly decreases with increasing extinction values, even for $A_V > 15 - 20$, indicating the presence of neutral carbon in a relatively large range of densities. With this in mind, if we now look at the image of C I/CO intensity ratio (see Fig. 4.4), we can conclude that carbon is a fairly good tracer of cloud structure.

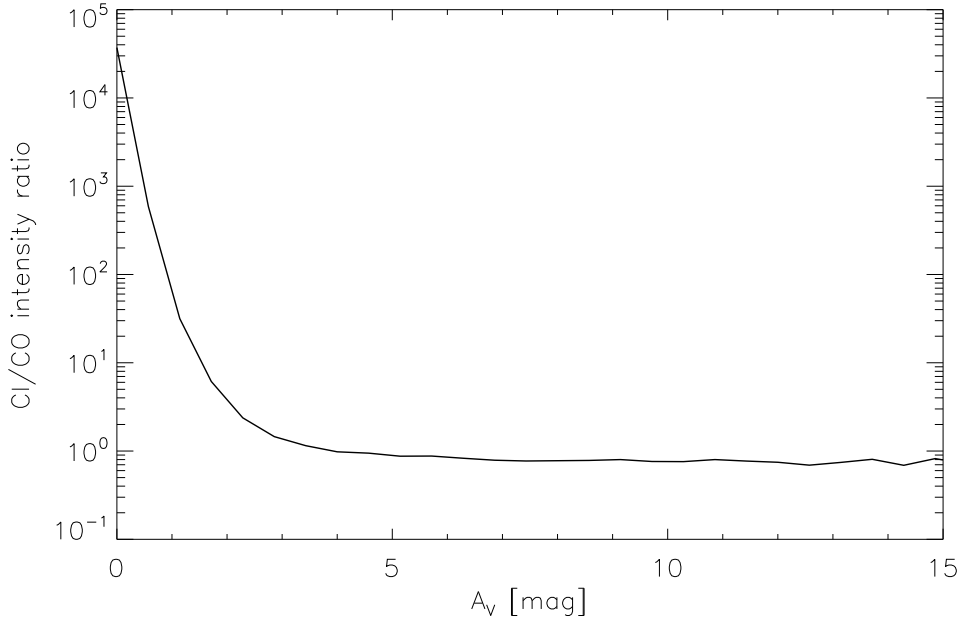


Figure 4.5: C I/CO velocity-integrated intensity W_C/W_{CO} as a function of extinction A_V . The intensity ratio is averaged in A_V bins.

Figure 4.5 also reveals that C I is a better tracer of the low extinction material than CO. Pineda et al. (2008) have shown that threshold extinction above which CO is detected is ~ 1 mag. Below this extinction value, the CO line intensity falls off very fast, in contrast to C I emission. In Fig. 4.1 we have seen that there is no significant range of extinction without associated C I emission. This causes the sharp rise in the intensity ratio, allowing carbon to be a better tracer of the low extinction material than CO.

4.4 Summary

In this chapter, in order to study C I emission from molecular clouds, we have used the simulations performed by Glover & Clark (2012c), using modified version of SPH code GADGET 2, to model a typical, small, nearby molecular cloud, such as Perseus

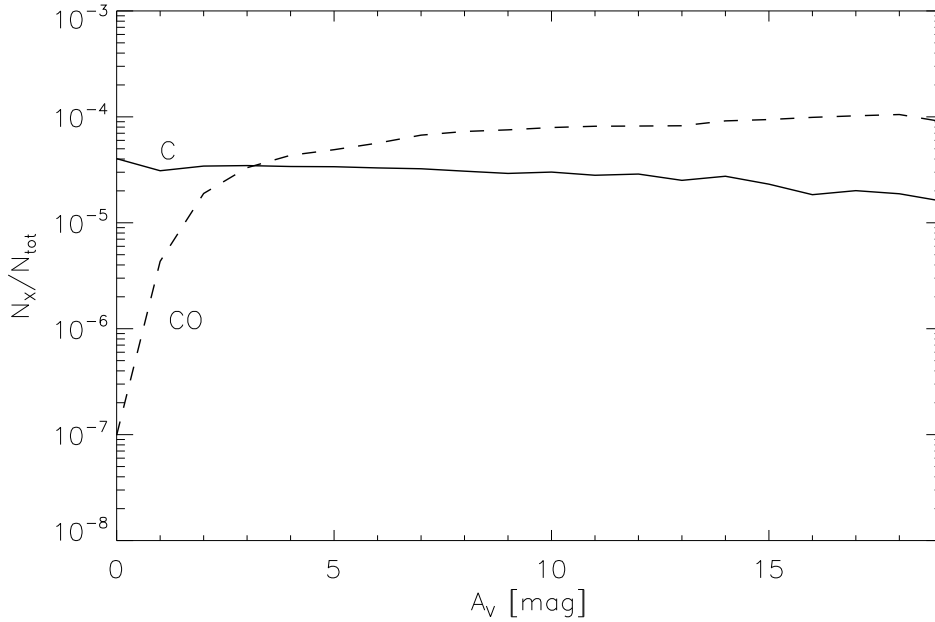


Figure 4.6: Column density ratios N_C/N_{tot} (solid line) and $N_{\text{CO}}/N_{\text{tot}}$ (dashed line) as a function of extinction A_V .

or Taurus. Along the general hydrodynamical and thermal treatment of the gas, this model also includes the treatment of the chemistry that tracks the formation of H_2 and CO proposed by Glover & Mac Low (2007a,b), and radiative heating and cooling proposed by Glover & Jappsen (2007). For the radiative transfer calculations, we use the Sobolev (LVG) method to solve for C I and CO level populations.

We find that the intensity of C I emission increases with the increasing total column density, reflecting the greater collisional excitation with density, but only until the critical column density value of $\sim 0.7 \times 10^{22} \text{ cm}^{-2}$, when the C I line emission reaches the maximum intensity. This further cause the flattening of intensity of integrated C I emission. For the same reason the C I integrated emission is not a good tracer of the C I column density. One might expect that the observed C I emission reveals the C I distribution but the PDF of velocity integrated C I intensity matches the C I column density PDF only at low densities. This can also be seen in the images of C I column density and line intensity. On the other hand, PDFs of C I column density and total column density match well.

We also show that C I is a good tracer of cloud structure. Velocity integrated intensity ratio between C I and CO is close to one for almost the entire cloud area. This correlation is particularly strong for the extinction value larger than 2. This defies the

classical picture where C I is almost non-existent inside the cloud but only in the thin shell around it. However, observations clearly show that C I emission does trace the CO emission well. Because of the photodissociation, C I is also a good tracer of the low extinction material at the surface of the cloud. At low extinction CO emission drops rapidly as CO dissociates into C I. Overall, C I emission is almost constant in the entire range of the extinction value.

5 Conclusions and outlook

In this thesis we have focused on the chemical aspect of molecular cloud formation and the influence of chemical processes on the gas dynamics.

We have performed and analysed a suite of state-of-art high-resolution 3D hydrodynamic simulations using the massively parallel code FLASH described in section 1.5. Most importantly, we have implemented a non-equilibrium chemical model by Glover & Mac Low (2007a,b) within the FLASH's adaptive mesh refinement structure. As a result, adding detailed treatment of atomic/molecular cooling and the most important hydrogen chemistry presents an enhancement to the previous models of molecular cloud formation.

In this manner, we proceed with the following study cases: formation of H_2 in the turbulent ISM where we study the difference between solenoidal and compressive turbulent driving; formation of cold, dense cloud in converging flows of warm atomic gas; and C I emission from the molecular clouds.

- **Chapter 2: Modelling H_2 Formation in the Turbulent ISM**

In this chapter we have shown that if the environment has strong turbulence or high mean density of the gas, molecular hydrogen forms fast regardless of turbulence being driven compressively or solenoidally. The gas reaches molecular hydrogen fraction of 90% very fast in both cases and it becomes fully molecular in less than the time required to assemble the cloud from the diffuse ISM. When expressed in the units of crossing time, H_2 formation takes longer when the strength of the turbulence is increased in the solenoidal case. On the other hand, H_2 formation timescale decreases when rms velocity is increased in the compressive case. When the dense gas becomes fully molecular, it no longer

contributes to the total H_2 formation rate. This occurs in both cases but has a greater effect in compressive case because of the faster initial H_2 formation rate. We also show that mixing of the material from overdense clumps into low density regions takes at least one-third of a turbulent crossing time, raising caution in usage of rapid gas mixing prescription by Gnedin et al. (2009). Their approximation is still valid in studies of how quickly different regions of the ISM become dominantly molecular, but it will be problematic if one is interested in final, equilibrium state of the gas.

- **Chapter 3: Cloud Formation in Colliding Flows**

When studying the cloud formation in converging flows, we compare our non-equilibrium model with one that uses simplified cooling function from Koyama & Inutsuka (2002). We find that two approaches are qualitatively similar. However, there are important quantitative differences. In Koyama & Inutsuka approach, the cooling rate of hot gas is significantly overestimated, while photoelectron heating is underestimated especially in CNM regime. In their model, most of the gas is in thermal equilibrium while in non-equilibrium treatment there is a wide spread of gas densities around the equilibrium. This occurs in the intermediate density regime $1 < n < 30 \text{ cm}^{-3}$ where photoelectric heating efficiency increases with electron number density. Morphology of the gas cloud is especially sensitive to the choice of the thermal treatment. Because of the difference in the cooling time of hot gas in two models, the velocity dispersion is different. In non-equilibrium treatment, the cooling time is longer, cloud remains over pressured for longer. Hence, it is accelerated outwards more efficiently and that creates more distorted distribution. One of the aspects where two approaches give similar results is the properties of the clumps. We find that these structures are not self gravitating because compressions produced in flow collisions are not sufficient to create gravitationally unstable pre-stellar cores. This means that in addition some sort of large scale collapse of the cloud is necessary.

- **Chapter 4: Modelling C I emission**

In this chapter we study the tracers of molecular cloud structure either through column density of C I or integrated C I emission. We find that integrated C I emission is not a good tracer of the total column density in the denser regions of the cloud. At the surface of the cloud, C I emission increases with the increasing total column density but toward the center of the cloud collisional excitation and the number of excited atoms become extremely large. As a result, C I emission reaches saturation and material continues emitting at constant maximum intensity. This results in flattening of intensity of integrated C I emission. For the same reason the C I integrated emission is not a good tracer of

the C I column density. It would be reasonable to expect that the observed C I emission reveals the C I distribution but the PDF of velocity integrated C I intensity matches the C I column density PDF only at low densities. This can also be seen in the images of C I column density and line intensity. On the other hand, PDFs of C I column density and total column density match well. We also show that C I is a good tracer of the cloud structure. Unlike the classical picture where C I exists only in the top layers of the cloud as a product of CO photodissociation, we find that C I forms in the entire cloud and its integrated emission matches the CO emission. C I is also an excellent tracer of the low extinction material at the surface of the cloud.

Acknowledgements

I acknowledge the financial support of the International Max Planck Research School for Astronomy and Cosmic Physics at the University of Heidelberg (IMPRS-HD) and the Heidelberg Graduate School of Fundamental Physics (HGSFP).

I am eternally grateful to both Dr. Simon Glover and Dr. Ralf Klessen for everything, but mostly for the infinite amount of support and patience throughout all these years. I have been honoured to have them directing my research and giving me the opportunity to pursue a career in Physics.

I would like to thank Dr. Henrik Beuther for interesting discussions and valuable comments on the present work. I also thank Dr. Matthias Bartelmann and Dr. Markus Oberthaler for kindly agreeing to be a part of my defence committee.

At the end I thank all the colleagues at the Institut für Theoretische Astrophysik.

Bibliography

- Abel, T., Anninos, P., Zhang, Y., & Norman, M. L. 1997, *New A*, 2, 181
- Arzoumanian, D., André, P., Didelon, P., et al. 2011, *A&A*, 529, L6
- Audit, E., & Hennebelle, P. 2005, *A&A*, 433, 1
- Bakes, E. L. O., & Tielens, A. G. G. M. 1994, *ApJ*, 427, 822
- Balbus, S. A., & Hawley, J. F. 1998, *Reviews of Modern Physics*, 70, 1
- Ballesteros-Paredes, J., & Hartmann, L. 2007, *Rev. Mexicana Astron. Astrofis.*, 43, 123
- Ballesteros-Paredes, J., Hartmann, L., & Vázquez-Semadeni, E. 1999a, *ApJ*, 527, 285
- Ballesteros-Paredes, J., Vázquez-Semadeni, E., & Scalo, J. 1999b, *ApJ*, 515, 286
- Banerjee, R., Vázquez-Semadeni, E., Hennebelle, P., & Klessen, R. S. 2009, *MNRAS*, 398, 1082
- Beatty, J. J., & Westerhoff, S. 2009, *Annual Review of Nuclear and Particle Science*, 59, 319
- Beck, R. 2001, *Space Sci. Rev.*, 99, 243
- Blitz, L., Fukui, Y., Kawamura, A., et al. 2007, *Protostars and Planets V*, 81
- Blitz, L., & Shu, F. H. 1980, *ApJ*, 238, 148
- Bohlin, R. C., Savage, B. D., & Drake, J. F. 1978, *ApJ*, 224, 132
- Boley, A. C., Hartquist, T. W., Durisen, R. H., & Michael, S. 2007, *ApJ*, 656, L89
- Braun, H., & Schmidt, W. 2012, *MNRAS*, 421, 1838

-
- Brown, P. N., Byrne, G. D., & Hindmarsh, A. C. 1989, *SIAM J. Sci. Stat. Comput.*, 10, 1038
- Brunt, C. M. 2010, *A&A*, 513, A67
- Brunt, C. M., Heyer, M. H., & Mac Low, M.-M. 2009, *A&A*, 504, 883
- Burkert, A., & Lin, D. N. C. 2000, *ApJ*, 537, 270
- Calder, A. C., Fryxell, B., Plewa, T., et al. 2002, *ApJS*, 143, 201
- Cen, R. 1992, *ApJS*, 78, 341
- Clark, P. C., Glover, S. C. O., & Klessen, R. S. 2012a, *MNRAS*, 420, 745
- Clark, P. C., Glover, S. C. O., Klessen, R. S., & Bonnell, I. A. 2012b, *MNRAS*, 424, 2599
- Colella, P., & Woodward, P. R. 1984, *Journal of Computational Physics*, 54, 174
- Crutcher, R. M. 1999, *ApJ*, 520, 706
- Crutcher, R. M., Hakobian, N., & Troland, T. H. 2009, *ApJ*, 692, 844
- Dullemond, C. P. 2012, *Astrophysics Source Code Library*, 2015
- Elmegreen, B. G. 2000, *ApJ*, 530, 277
- Elmegreen, B. G., & Scalo, J. 2004, *ARA&A*, 42, 211
- Engargiola, G., Plambeck, R. L., Rosolowsky, E., & Blitz, L. 2003, *ApJS*, 149, 343
- Falgarone, E., Puget, J.-L., & Perault, M. 1992, *A&A*, 257, 715
- Federrath, C., Glover, S. C. O., Klessen, R. S., & Schmidt, W. 2008a, *Physica Scripta Volume T*, 132, 014025
- Federrath, C., Klessen, R. S., & Schmidt, W. 2008b, *ApJ*, 688, L79
- . 2009, *ApJ*, 692, 364
- Federrath, C., Roman-Duval, J., Klessen, R. S., Schmidt, W., & Mac Low, M.-M. 2010, *A&A*, 512, A81
- Federrath, C., Sur, S., Schleicher, D. R. G., Banerjee, R., & Klessen, R. S. 2011, *ApJ*, 731, 62
-

-
- Ferland, G. J., Peterson, B. M., Horne, K., Welsh, W. F., & Nahar, S. N. 1992, *ApJ*, 387, 95
- Ferrière, K. M. 2001, *Reviews of Modern Physics*, 73, 1031
- Field, G. B. 1965, *ApJ*, 142, 531
- Field, G. B., Goldsmith, D. W., & Habing, H. J. 1969, *ApJ*, 155, L149
- Frerking, M. A., Keene, J., Blake, G. A., & Phillips, T. G. 1989, *ApJ*, 344, 311
- Fryxell, B., Olson, K., Ricker, P., et al. 2000, *ApJS*, 131, 273
- Gazol, A., Vázquez-Semadeni, E., & Kim, J. 2005, *ApJ*, 630, 911
- Gazol, A., Vázquez-Semadeni, E., Sánchez-Salcedo, F. J., & Scalo, J. 2001, *ApJ*, 557, L121
- Gillmon, K., Shull, J. M., Tumlinson, J., & Danforth, C. 2006, *ApJ*, 636, 891
- Glover, S. C. O. 2003, *ApJ*, 584, 331
- Glover, S. C. O., & Abel, T. 2008, *MNRAS*, 388, 1627
- Glover, S. C. O., & Clark, P. C. 2012a, *MNRAS*, 421, 116
- . 2012b, *MNRAS*, 421, 9
- . 2012c, *MNRAS*, 426, 377
- Glover, S. C. O., Federrath, C., Mac Low, M.-M., & Klessen, R. S. 2010, *MNRAS*, 404, 2
- Glover, S. C. O., & Jappsen, A.-K. 2007, *ApJ*, 666, 1
- Glover, S. C. O., & Mac Low, M.-M. 2007a, *ApJS*, 169, 239
- . 2007b, *ApJ*, 659, 1317
- . 2011, *MNRAS*, 412, 337
- Gnedin, N. Y., & Kravtsov, A. V. 2011, *ApJ*, 728, 88
- Gnedin, N. Y., Tassis, K., & Kravtsov, A. V. 2009, *ApJ*, 697, 55
- Goldsmith, P. F. 2001, *ApJ*, 557, 736
- Goldsmith, P. F., & Langer, W. D. 1978, *ApJ*, 222, 881
-

-
- Gould, R. J., & Salpeter, E. E. 1963, *ApJ*, 138, 393
- Habing, H. J. 1968, *Bull. Astron. Inst. Netherlands*, 19, 421
- Hartmann, L. 2003, *ApJ*, 585, 398
- Hartmann, L., Ballesteros-Paredes, J., & Bergin, E. A. 2001, *ApJ*, 562, 852
- Heiles, C., & Troland, T. H. 2003, *ApJ*, 586, 1067
- Heitsch, F., Burkert, A., Hartmann, L. W., Slyz, A. D., & Devriendt, J. E. G. 2005, *ApJ*, 633, L113
- Heitsch, F., & Hartmann, L. 2008, *ApJ*, 689, 290
- Hennebelle, P., Banerjee, R., Vázquez-Semadeni, E., Klessen, R. S., & Audit, E. 2008, *A&A*, 486, L43
- Hennebelle, P., & Pérault, M. 1999, *A&A*, 351, 309
- Heyer, M. H., & Brunt, C. M. 2004, *ApJ*, 615, L45
- Hollenbach, D., & McKee, C. F. 1979, *ApJS*, 41, 555
- . 1989, *ApJ*, 342, 306
- Hollenbach, D. J., Takahashi, T., & Tielens, A. G. G. M. 1991, *ApJ*, 377, 192
- Hollenbach, D. J., Werner, M. W., & Salpeter, E. E. 1971, *ApJ*, 163, 165
- Huff, E. M., & Stahler, S. W. 2006, *ApJ*, 644, 355
- Hughes, A., Wong, T., Ott, J., et al. 2010, *MNRAS*, 406, 2065
- Kaufman, M. J., Wolfire, M. G., Hollenbach, D. J., & Luhman, M. L. 1999, *ApJ*, 527, 795
- Keene, J., Lis, D. C., Phillips, T. G., & Schilke, P. 1997, 178, 129
- Kennicutt, Jr., R. C. 1998, *ARA&A*, 36, 189
- Kim, W.-T., & Ostriker, E. C. 2006, *ApJ*, 646, 213
- Klessen, R. S. 2001, *ApJ*, 556, 837
- Klessen, R. S., Heitsch, F., & Mac Low, M.-M. 2000, *ApJ*, 535, 887
- Klessen, R. S., Krumholz, M. R., & Heitsch, F. 2009, [arXiv:astro-ph/0906.4452](https://arxiv.org/abs/astro-ph/0906.4452)
-

-
- Koyama, H., & Inutsuka, S.-I. 2000, *ApJ*, 532, 980
- . 2002, *ApJ*, 564, L97
- Krumholz, M. R., & Gnedin, N. Y. 2011, *ApJ*, 729, 36
- Krumholz, M. R., Matzner, C. D., & McKee, C. F. 2006, *ApJ*, 653, 361
- Krumholz, M. R., McKee, C. F., & Tumlinson, J. 2009, *ApJ*, 693, 216
- Lai, S.-P., Crutcher, R. M., Girart, J. M., & Rao, R. 2001, *ApJ*, 561, 864
- . 2002, *ApJ*, 566, 925
- Langer, W. 1976, *ApJ*, 206, 699
- Larson, R. B. 1981, *MNRAS*, 194, 809
- Le Teuff, Y. H., Millar, T. J., & Markwick, A. J. 2000, *A&AS*, 146, 157
- Lemaster, M. N., & Stone, J. M. 2008, *ApJ*, 682, L97
- Little, L. T., Gibb, A. G., Heaton, B. D., Ellison, B. N., & Claude, S. M. X. 1994, *MNRAS*, 271, 649
- Mac Low, M.-M. 1999, *ApJ*, 524, 169
- Mac Low, M.-M., & Glover, S. C. O. 2012, *ApJ*, 746, 135
- Mac Low, M.-M., & Klessen, R. S. 2004, *Reviews of Modern Physics*, 76, 125
- Mac Low, M.-M., Klessen, R. S., Burkert, A., & Smith, M. D. 1998, *Physical Review Letters*, 80, 2754
- Mac Low, M.-M., & Shull, J. M. 1986, *ApJ*, 302, 585
- Martin, P. G., Keogh, W. J., & Mandy, M. E. 1998, *ApJ*, 499, 793
- McKee, C. F., & Ostriker, E. C. 2007, *ARA&A*, 45, 565
- McKee, C. F., & Ostriker, J. P. 1977, *ApJ*, 218, 148
- Meixner, M., & Tielens, A. G. G. M. 1993, *ApJ*, 405, 216
- Men'shchikov, A., André, P., Didelon, P., et al. 2010, *A&A*, 518, L103
- Micic, M., Glover, S. C. O., Banerjee, R., & Klessen, R. S. 2012b, submitted to *MNRAS*
-

-
- Micic, M., Glover, S. C. O., Federrath, C., & Klessen, R. S. 2012a, MNRAS, 421, 2531
- Mihalas, D. 1978, *Stellar atmospheres* /2nd edition/
- Moos, H. W., Cash, W. C., Cowie, L. L., et al. 2000, ApJ, 538, L1
- Mouschovias, T. C., & Spitzer, Jr., L. 1976, ApJ, 210, 326
- Myers, P. C. 1983, ApJ, 270, 105
- Nelson, R. P., & Langer, W. D. 1999, ApJ, 524, 923
- Ossenkopf, V., & Mac Low, M.-M. 2002, A&A, 390, 307
- Ostriker, E. C., Stone, J. M., & Gammie, C. F. 2001, ApJ, 546, 980
- Palla, F., & Stahler, S. W. 2000, ApJ, 540, 255
- Parker, E. N. 1966, ApJ, 145, 811
- Pineda, J. E., Caselli, P., & Goodman, A. A. 2008, ApJ, 679, 481
- Plewa, T., Linde, T. J., & Weirs, V. G. 2005, none
- Plewa, T., & Müller, E. 1999, A&A, 342, 179
- Pompe, W. 1985, *Zeitschrift Angewandte Mathematik und Mechanik*, 65, 536
- Price, D. J., & Federrath, C. 2010, MNRAS, 406, 1659
- Price, D. J., Federrath, C., & Brunt, C. M. 2011, ApJ, 727, L21
- Roman-Duval, J., Jackson, J. M., Heyer, M., Rathborne, J., & Simon, R. 2010, ApJ, 723, 492
- Rosolowsky, E., & Blitz, L. 2005, ApJ, 623, 826
- Sahnow, D. J., Moos, H. W., Ake, T. B., et al. 2000, ApJ, 538, L7
- Scalo, J., & Elmegreen, B. G. 2004, ARA&A, 42, 275
- Schilke, P., Keene, J., Le Bourlot, J., Pineau des Forets, G., & Roueff, E. 1995, A&A, 294, L17
- Schmidt, W., Federrath, C., Hupp, M., Kern, S., & Niemeyer, J. C. 2009, A&A, 494, 127
-

- Schroder, K., Staemmler, V., Smith, M. D., Flower, D. R., & Jaquet, R. 1991, *Journal of Physics B Atomic Molecular Physics*, 24, 2487
- Scoville, N. Z., & Hersh, K. 1979, *ApJ*, 229, 578
- Scoville, N. Z., Solomon, P. M., & Sanders, D. B. 1979, in *IAU Symposium, Vol. 84, The Large-Scale Characteristics of the Galaxy*, ed. W. B. Burton, 277–282
- Sembach, K. R., Howk, J. C., Ryans, R. S. I., & Keenan, F. P. 2000, *ApJ*, 528, 310
- Shetty, R., Glover, S. C., Dullemond, C. P., & Klessen, R. S. 2011, *MNRAS*, 412, 1686
- Sobolev, V. V. 1957, *Soviet Ast.*, 1, 678
- Solomon, P. M., Rivolo, A. R., Barrett, J., & Yahil, A. 1987, *ApJ*, 319, 730
- Solomon, P. M., Sanders, D. B., & Scoville, N. Z. 1979, *ApJ*, 232, L89
- Spitzer, Jr., L., & Jenkins, E. B. 1975, *ARA&A*, 13, 133
- Springel, V. 2005, *MNRAS*, 364, 1105
- Stoerzer, H., Stutzki, J., & Sternberg, A. 1996, *A&A*, 310, 592
- Sutherland, R. S., & Dopita, M. A. 1993, *ApJS*, 88, 253
- Tielens, A. G. G. M., & Hollenbach, D. 1985, *ApJ*, 291, 722
- Trevisan, C. S., & Tennyson, J. 2002, *Plasma Physics and Controlled Fusion*, 44, 1263
- Troland, T. H., & Crutcher, R. M. 2008, *ApJ*, 680, 457
- Truelove, J. K., Klein, R. I., McKee, C. F., et al. 1997, *ApJ*, 489, L179
- van der Tak, F. F. S., Black, J. H., Schöier, F. L., Jansen, D. J., & van Dishoeck, E. F. 2007, *A&A*, 468, 627
- Vázquez-Semadeni, E., Ballesteros-Paredes, J., & Klessen, R. S. 2003, *ApJ*, 585, L131
- Vázquez-Semadeni, E., Banerjee, R., Gómez, G. C., et al. 2011, *MNRAS*, 414, 2511
- Vázquez-Semadeni, E., Gazol, A., & Scalo, J. 2000, *ApJ*, 540, 271
- Vázquez-Semadeni, E., Gómez, G. C., Jappsen, A. K., et al. 2007, *ApJ*, 657, 870
- Vázquez-Semadeni, E., Ryu, D., Passot, T., González, R. F., & Gazol, A. 2006, *ApJ*, 643, 245
-

Weingartner, J. C., & Draine, B. T. 2001a, *ApJ*, 563, 842

—. 2001b, *ApJS*, 134, 263

Wolfire, M. G., Hollenbach, D., McKee, C. F., Tielens, A. G. G. M., & Bakes, E. L. O. 1995, *ApJ*, 443, 152

Wolfire, M. G., McKee, C. F., Hollenbach, D., & Tielens, A. G. G. M. 2003, *ApJ*, 587, 278

Wolfire, M. G., Tielens, A. G. G. M., Hollenbach, D., & Kaufman, M. J. 2008, *ApJ*, 680, 384

Wong, T., & Blitz, L. 2002, *ApJ*, 569, 157

Woodall, J., Agúndez, M., Markwick-Kemper, A. J., & Millar, T. J. 2007, *A&A*, 466, 1197

Woodward, P. R. 1978, *ARA&A*, 16, 555

Zuckerman, B., & Evans, II, N. J. 1974, *ApJ*, 192, L149

Zuckerman, B., & Palmer, P. 1974, *ARA&A*, 12, 279
